Wavelength modulation spectroscopy of industrial flame systems

by

Torrey Rahe Schenkenberger Hayden

B.S. Saint Lawrence University, 2013

M.S. University of Colorado Boulder, 2015

A thesis submitted to the

Faculty of the Graduate School of the

University of Colorado in partial fulfillment

of the requirements for the degree of

Doctor of Philosophy

Department of Mechanical Engineering

2018

ProQuest Number: 10928017

ProQuest 10928017

This dissertation entitled:

Wavelength modulation spectroscopy of industrial flame systems

written by Torrey Rahe Schenkenberger Hayden

has been approved for the Department of Mechanical Engineering

Professor Gregory B. Rieker (Principal Advisor)

Mark Strobel

Professor Peter Hamlington

Date:

The final copy of this thesis has been examined by the signatories, and we
find that both the content and the form meet acceptable presentation standards
of scholarly work in the above mentioned discipline.

Abstract

Hayden, Torrey Rahe Schenkenberger (Ph.D., Department of Mechanical Engineering)

Wavelength modulation spectroscopy of industrial flame systems
Dissertation directed by Assistant Professor Gregory B. Rieker

Combustion is widely used for materials processing, propulsion, and power production. Understanding the temporal and spatial variations within practical combustion systems can help to optimize their stability, uniformity, emissions, and/or efficiency. Wavelength modulation spectroscopy (WMS) provides quantitative, non-intrusive, time-resolved measurements of line-of-sight thermodynamic properties in a gas sample. This dissertation describes the development and application of novel WMS sensors for measurements in industrial flame environments. After an overview of WMS, we describe the development of the first WMS sensor to measure OH radical near 1491 nm. We perform the first dual-comb spectroscopy measurement above a premixed flame in order to develop accurate models for the H_2O absorption that interferes with OH absorption at elevated temperatures. The model improves the absolute OH measurement accuracy. We apply the OH sensor in conjunction with temperature and H_2O mole fraction WMS sensors to characterize a premixed ribbon burner interacting with an industrial chilled-roller polymer-treatment system. Measurements at the surface of the polymer, together with post analysis of the surface oxidation, provides the first experimental demonstration of the connection between concentrations of OH radical in a premixed flame and the level of oxidation of polypropylene film in flame processing. The WMS sensors are used to probe the temporal, vertical and 2D variation in the heated, buoyant jet above an iron-chromium alloy catalytic combustor, which could be used for industrial materials processing. We develop a new pathlength correction method that uses computational fluid dynamics simulations to account for the effect of the narrowing and billowing of the heated gases on the measured water vapor mole fraction. The vertical profiles of temperature and H_2O mole fraction show a high likelihood of additional combustion above the catalytic surface under certain operating conditions. Finally, we extend the WMS technique to measure high-density gases by performing the first large amplitude wavelength modulation spectroscopy with a MEMS-Tunable Vertical Cavity Surface-Emitting Laser (MEMS-VCSEL). We demonstrate the

technique on high-pressure mixtures of CO_2 in air that are 2.5 times higher density than previously published WMS measurements (equivalent to greater than 255 atm at 1500 K). Together, these measurements demonstrate the utility of WMS sensors in optimizing and characterizing industrial combustion systems.

Acknowledgments

I would like to thank the color purple, beer-league softball, coffee with chocolate, and micro-brews for getting me through graduate school. Although these things that have brought me small daily joys, it has really been the people in my life who have made this whole journey possible.

It would be hard to not start off with a heartfelt thank you to my family who has been so supportive throughout this whole journey. I am grateful of your sacrifices that made attendance at Colorado Academy, St. Lawrence University and CU-Boulder possible. My parents always encouraged me to put my education first, which is something I'll always be thankful for. Thank you to my aunts, uncles, other family members and family-friends who helped make it easier for me to pursue higher education, from picking me up from the airport to taking me out to dinner. I could not have survived grad school without the immense support of my boyfriend Houston Judd, who has been my rock for the last several years. From going on runs, hiking 14ers and cooking me meals, you have been the steady presence in my life and have an unwavering supporter of my goals and I can never say thank you enough.

I honestly don't think I could have made the journey through graduate school without my lab-mates in the people of the Precision Laser Diagnostics. It's rare to find a group of people who are as smart, hard-working, compassionate and fun all in one place. There are too many ways that you have all helped me in the last several years. From our weekly Friday activities (Halo, beers or football), late nights in the lab or discussing a new idea, it's been such a pleasure to work with every single one of you. In particular, thank you to one and only, señor musculos, (Dr.) Paul Schroeder, who started this crazy journey with me when we signed on with a brand-new professor and always was willing to help me discuss new ideas, use his muscles to help me or just be a listening ear. Also, a big thank you to Amanda who always told me "It's going to be great!" with a smile, read my paper drafts and help me set up optics in the lab while we listen to Taylor Swift.

Next, I thank those who aided in the technical portion of this work. I am thankful to the funding provided by 3M Company for the research presented in Ch. 2-4 of this dissertation. Thank you to all of the

people who helped make this work possible: Bill Andrews for his design and construction of the experimental setup, Alan Sanchez for his work on the LabView software and development of real-time Dr. Melvyn Branch for helpful conversations and insight in various stages of our work and Dan Petrykowski for his help in finishing up my experiments this year and asking all of the right questions. I appreciate all of the work done by the other graduate students on my project, Jason, Caelan, Nick and Sid, who were always ready to help or provide simulations and to Dr. Peter Hamlington for challenging my assumptions and encouraging us to design better experiments to help validate the computational models. Thank you to Mark Strobel and Ani Urupahye for their thoughtful questions and support for our research for the last several years. It was such a unique learning experience to come to St. Paul for the summer to intern at 3M and work with the great people there. A big thank you to all of the help I received from Mark, Ani, Adrianne and the rest of the Surface Modification group on the experiments at 3M. Additionally, thank you to Luke Heinzen for the opportunity to work on his interesting combustion system during my internship.

Finally, I have to thank my PhD advisor Dr. Greg Rieker and his wife Dr. Julie Steinbrenner. Although I may complain about the lasers or Igor Pro, I am thankful every day that I came to CU to work with Greg. He has always encouraged me to be a better researcher while daily demonstrating his deep care for us as humans. Maybe one of these days his perfectionism will rub off on me. I greatly appreciate all of Julie's care and patience editing my papers, answering my questions about thermocouples and what to wear to conferences and all the times I kept Greg late discussing research. I cannot think of a power couple I would rather learn how to be a professional researcher and teacher from.

Table of Contents

List of Tables

List of Figures

1 Introduction

1.1 Motivation and background

1.1.1 Industrial combustion systems

Combustion is used in a variety of industries including materials processing, propulsion, and power production. The specific application will determine the desired qualities of the combustor or combustion process. For example, some materials processing applications require high temperatures or the presence of certain radical species to achieve a desired processing goal. It is therefore desirable to develop sensors that are capable of studying the properties of various types of combustion systems so that the desired qualities of the system can be optimized.

In materials and food processing, it is often desirable to treat a product with heat and/or expose the product to unstable radical species. Premixed flames are one method of combustion that has been used extensively for polymer film, wood and food processing [1–4]. Premixed combustion is when the fuel and oxidizer are pre-mixed before the combustion reactions begin, shown in Fig. 1-1(a). These systems are ideal for producing high temperature, uniform flames with radicals that can react with a material during processing.

In most processing applications, it is desirable to have spatial and temporal uniformity to maintain consistency in the product. Burner designs, such as a ribbon burner, have been developed to improve uniformity [1]. However, the species and temperature still vary greatly across different regions of the flame and with the introduction of equipment that handles the material being processed. Hence, diagnostics that measure uniformity and probe the internal flame structure are of great value in optimizing a given process.

Some industrial applications, such as large-scale baking, require lower temperatures without chemical treatment. In these applications, the introduction of a catalyst can reduce the temperature and the presence of radicals in the combustion product gases. An example of a catalytic combustor operating on methane and air is shown in Fig. 1-1(b). In catalytic combustion, the fuel and oxidizer react on the catalyst, which aids in the dissociation of O_2 and the breaking of the C-H bond, resulting in combustion at lower

1

temperatures and with reduced pollutant emissions [5,6]. If the catalytic system is used for materials processing, spatial and temporal uniformity must be considered. Furthermore, it is not desirable to have additional radicals present above the catalytic surface for some processes like the reduction of emissions through the use of catalytic combustion. By studying the species and temperature exiting the catalytic combustor we can determine catalyst health, presence of additional combustion and the uniformity of the product gases that would impinge on a product.
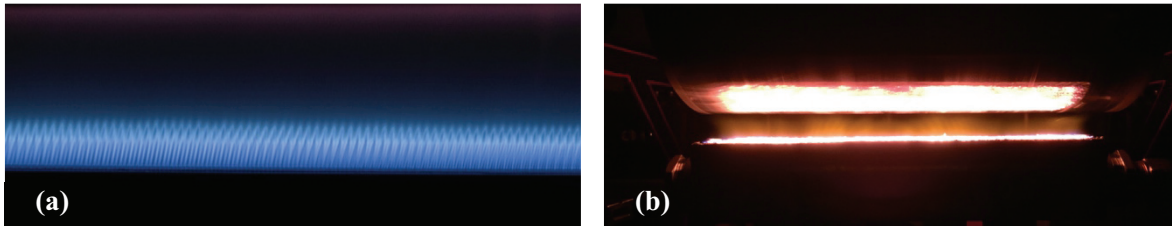
Fig. 1-1. Examples of (a) a premixed flame system and (b) a catalytic combustor with chilled roller for materials processing.

In propulsion and transportation, many systems are dominated by high pressure combustion, which maximizes efficiency and minimizes energy loss during combustion [7–9]. In order to make even small gains in engine efficiency, diagnostics are needed to differentiate small changes in operational conditions or engine design [10,11]. Measurements of species concentrations and temperature provide insight into the chemical kinetics and engine operation. Because the combustion in these systems can happen on a fast time scale, it is necessary to have a quantitative, fast, and time resolved diagnostic. However, the high-pressure nature of these systems is challenging for most traditional and laser diagnostics.

1.1.2 Qualities of combustion systems

There are a variety of conditions that can affect combustion reactions and the resulting gas properties. The amount of air and fuel mixed together in premixed combustion will greatly affect the thermodynamic properties of the resulting combustion. Combustion processes are exothermic, meaning they release energy as the chemical reactions occur at standard conditions. The amount of energy released during reaction is determined by the quantity and type of fuel used. The energy per unit mass or mole of fuel is quantified through the heat of combustion (ΔH_c, enthalpy change during the reaction) or the lower heating value (LHV,

2

amount of heat released during the combustion of a fuel assuming the product H_2O remains in vapor form). Therefore, the estimated power flux for a control volume combustor can be described as by:

$$\Delta \dot{E} = \frac{\Delta H_c \dot{m}}{A_{comb}} \tag{1-1}$$

where $\Delta \dot{E}$ is the energy released per second per unit area, $\dot{m}$ is the mass flow rate of the fuel and A_{comb} is the surface area of the combustor.

In premixed combustion, the fuel will be combined with an oxidizer prior to the inception of reactions. The ratio of the mass flow rate of air to the mass flow rate of fuel can be denoted as the A/F ratio and has an effect on the flame heat release and can affect the flame chemistry. If there is exactly the amount of oxidizer needed to react all of the fuel, the resulting ratio of the air to fuel mass flow rate is known as the stoichiometric ratio. The stoichiometric ratio will depend on the fuel and oxidizer being used for combustion. Equivalence ratio (ϕ) relates any other A/F ratio to the stoichiometric ratio by:

$$\phi = \frac{\left(\dot{m}_{ox}/\dot{m}_{fuel}\right)_{st}}{\left(\dot{m}_{ox}/\dot{m}_{fuel}\right)} = \frac{\left(n_{ox}/n_{fuel}\right)_{st}}{\left(n_{ox}/n_{fuel}\right)} \tag{1-2}$$

where $\dot{m}_{ox}$ is the mass flow rate of the oxidizer, $\dot{m}_{fuel}$ is the mass flow rate of the fuel, n_{ox} is the moles of oxidizer, n_{fuel} is the moles of fuel and st indicates the stoichiometric ratio. If there is more air than needed, the system is considered to be fuel-lean ($\phi<1$). On the other hand, if there is less air than needed it is denoted fuel-rich ($\phi>1$), which will often result in additional reactions or secondary diffusion flames. Because the fuel and air flow rate are typically controlled by the system, it is important to understand how a combustion system varies as the inlet conditions change.

We can study the effect of these combustion conditions on the flame properties by using laser diagnostics to probe gases throughout the reactions. As suggested in Sec. 1.1.1, studying the thermodynamic of the gases in a flame or post-combustion can provide insight on how the combustion process could be used for industrial applications. Two of the properties that laser diagnostics can probe are temperature and species mole fraction. These two properties can provide insight into system uniformities, heat transfer and

chemistry in combustion systems. Temperature measurements will be bounded by theoretical limit of the adiabatic flame temperature, which assumes that all of the heat released in the reaction heats up the product gases. Comparing measured temperatures to the adiabatic flame temperature can provide insight into the heat transfer. Because H_2O and CO_2 are final products of combustion reactions, diagnostics targeting these species are ideal to understand combustion completeness and system conditions. Studies of radical intermediates such as OH, CO, H, O, HO_2 can improve understanding of flame structure and chemical reactions in the flame. Hence, laser diagnostics can provide valuable information to optimize the industrial combustion systems described in the previous section.

1.2 Wavelength modulation spectroscopy

1.2.1 Laser absorption spectroscopy

WMS and other forms of absorption spectroscopy are performed by quantifying the amount of light absorbed by a gas as a function of wavelength and relating it to the thermodynamic state of the molecules. Traditional tunable diode laser absorption spectroscopy (TDLAS) is performed by repetitively sweeping the injection current of a diode laser to vary the laser intensity and frequency. An example of this technique is shown in Fig. 1-2, where a linear sweep is applied. The incident or un-attenuated light (I_0) enters the gas sample and is transmitted to a detector on the other side. The light will be absorbed by a molecular species of interest if the wavelength of the light matches the energy of a quantum transition in the target species. The amount of light absorbed by a given species is dependent on the number of molecules in a given state and can be described by Beer-Lambert law:

$$\frac{I_t}{I_0} = exp\left(-\sum_j S_j(T)PX_iL\phi(v)\right) \qquad (1\text{-}3)$$

where I_t is the transmitted intensity through the sample, I_0 is the un-attenuated intensity, $S_j(T)$ is the linestrength of a given transition j at the specified temperature (T), P is the system pressure, X_i is the absorbing species mole fraction, L is the pathlength probed by the laser, and $\phi(v)$ is the lineshape function, which varies with optical frequency, v. The argument of the exponential is known as absorbance, which is

4

often denoted as α and is illustrated in Fig. 1-2(c). Absorbance measured as a function of wavelength or optical frequency can be related to the path-averaged thermodynamic properties.
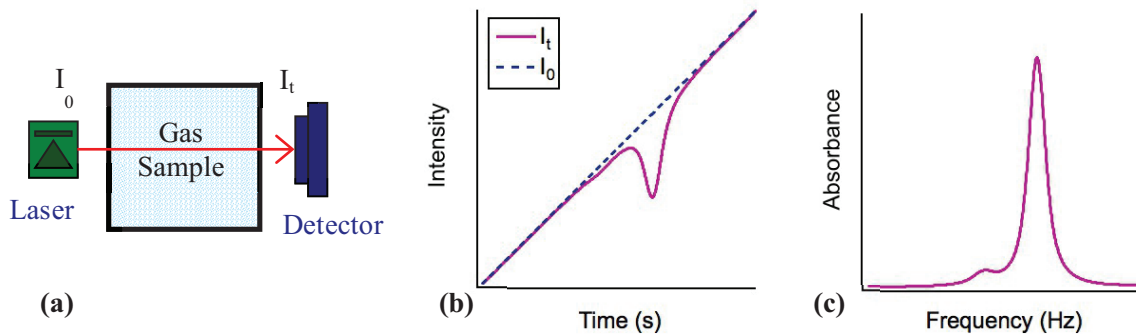
Fig. 1-2. Example tunable diode laser absorption spectroscopy measurement. (a) A schematic of laser light at a known frequency passing through a gas sample of interest. (b) A sample intensity/wavelength sweep of the laser demonstrating the attenuation of the incident light (I_0) by absorption by the gas sample to result in the transmitted (I_t) light intensity. (c) Absorbance as a function of frequency calculated from b) using the Beer-lambert law and a measured frequency sweep.

One of the most straightforward ways to extract thermodynamic properties from absorbance measurements is to fit a model to the measured absorbance data. In many atmospheric-pressure systems, it is sufficient to model the lineshape as a Voigt profile – a convolution of the Gaussian and Lorentz profiles that captures the collisional and Doppler broadening of the absorption feature. Other profiles may be used to improve the accuracy of the fit and capture the complicated physics [12]; however, uncertainties in foreign broadening in flames and computational complexity prevented their use in this work. The four components of required to simulate a Voigt profile are: center frequency (v_0), integrated area (A), Lorentz or collisional width (Δv_c) and Doppler width (Δv_D). These quantities are calculated from the transition-specific parameters, known as spectral line parameters, (except the Doppler width, which is not transition-specific): linecenter, pressure-shift coefficient, linestrength, foreign and self-broadening coefficients, and the temperature dependence of each parameter, which are catalogued in spectral databases such as HITRAN and HITEMP or measured line lists [13–15].

1.2.2 Temperature and species mole fraction measurements using absorption spectroscopy

In TDLAS, the most direct means to determine the gas temperature and concentration is using the integrated absorbance area of one or more quantum transitions extracted from fitting the measured absorbance. While the specific shape of an absorption transition ($\phi(v)$) depends on the other non-absorbing

5

gases present in the system (CO_2, CO, etc. in combustion systems), the integrated absorbance area is independent of collision partner, and therefore does not require measurements or assumptions of the other gases in the system [16,17]. Indeed, by definition the lineshape function $\int_{-\infty}^{\infty} \phi(\nu)d\nu \equiv 1$. Therefore, integrating Eq. (1-3) over an entire transition results in Eq. (1-4), which describes integrated absorbance, A:

$$A = \int \alpha \, d\nu = S(T)PX_{abs}L \tag{1-4}$$

where $S(T)$ is the linestrength of the probed transition at temperature T, P is the total pressure, X_{abs} is the species mole fraction of the absorbing gas and L is the pathlength of the laser beam across the gas sample.

Once integrated absorbance is extracted by fitting a model to the data, it can be used to calculate the temperature and absorbing species mole fraction across the beam path. Taking the ratio of the integrated areas (A_1 and A_2) of two absorption features creates a quantity that only depends on the linestrengths, which are only a function of temperature. As shown in Eq. (1-5), the ratio eliminates pressure and pathlength dependence, which means these quantities do not need to be known in order to process the data. A look up table correlating this ratio to a measured temperature is created them by using the equations for S(T) in Ref. [18] and the specific line parameters mentioned in Sec. 1.2.1. One can then use a measured ratio to interpolate the measured temperature, as shown in Fig. 1-3. A more extensive description of two-line thermometry can be found in the work of Falcone and Hanson [19].

$$\frac{A_1}{A_2} = \frac{S_1(T)PXL}{S_2(T)PXL} = \frac{S_1(T)}{S_2(T)} = f(T) \tag{1-5}$$

This work utilizes two NEL Inc. distributed feedback (DFB) diode lasers centered on H_2O absorption transitions at 1391.7 nm and 1468.9 nm. The features were chosen because of the large difference in the lower state energy of these transitions (1045 cm^{-1} and 3319 cm^{-1} respectively), which optimizes the temperature sensitivity at elevated temperatures, and the existence of previously validated linestrength parameters measured in Ref. [20].
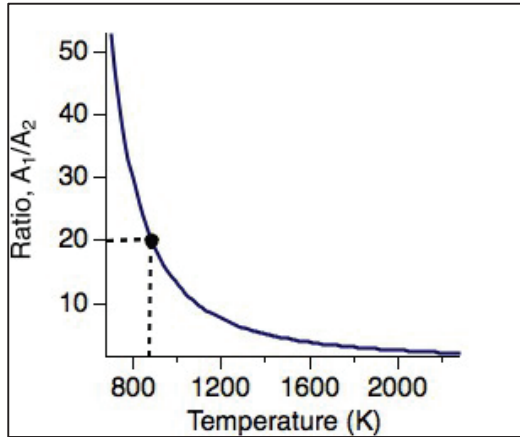
Fig. 1-3. Ratio of linestrengths, S(T) or integrated absorbance, A, for two different H_2O absorption transitions. The ratio of these two quantities is only dependent on temperature, thus enables calculation of temperature.

With the temperature now known, we calculate the species mole fraction by solving Eq. (1-4) for X_{abs} using the integrated absorbance of one transition. Room pressure is measured using a calibrated capacitance manometer at the time of experiments. The linestrength, $S(T)$, is calculated using measured parameters from Ref. [20]. If the absorbing species is present in the ambient air, outside of the measurement volume, its presence needs to be quantified and then subtracted off of any measured signal.

1.2.3 Scanned wavelength modulation spectroscopy

This work utilizes a sensitive form of absorption spectroscopy, wavelength modulation spectroscopy (WMS), to probe the thermodynamic properties of combustion systems. In WMS, the wavelength and intensity of the laser is modulated at a fast frequency *f*. For wavelength modulation techniques, this frequency is typically 10-500 kHz, as shown in the schematic of Fig. 1-4(a) [21]. In a typical DFB laser, the modulation is applied via injection current tuning, which induces temperature change and subsequent wavelength tuning, along with intensity modulation of the laser, as shown in Fig. 1-4(b). The thermal tuning and intensity modulation under this situation is primarily linear since the tuning range is is small (<1 nm) and any wavelength dependent loss is monotonic.
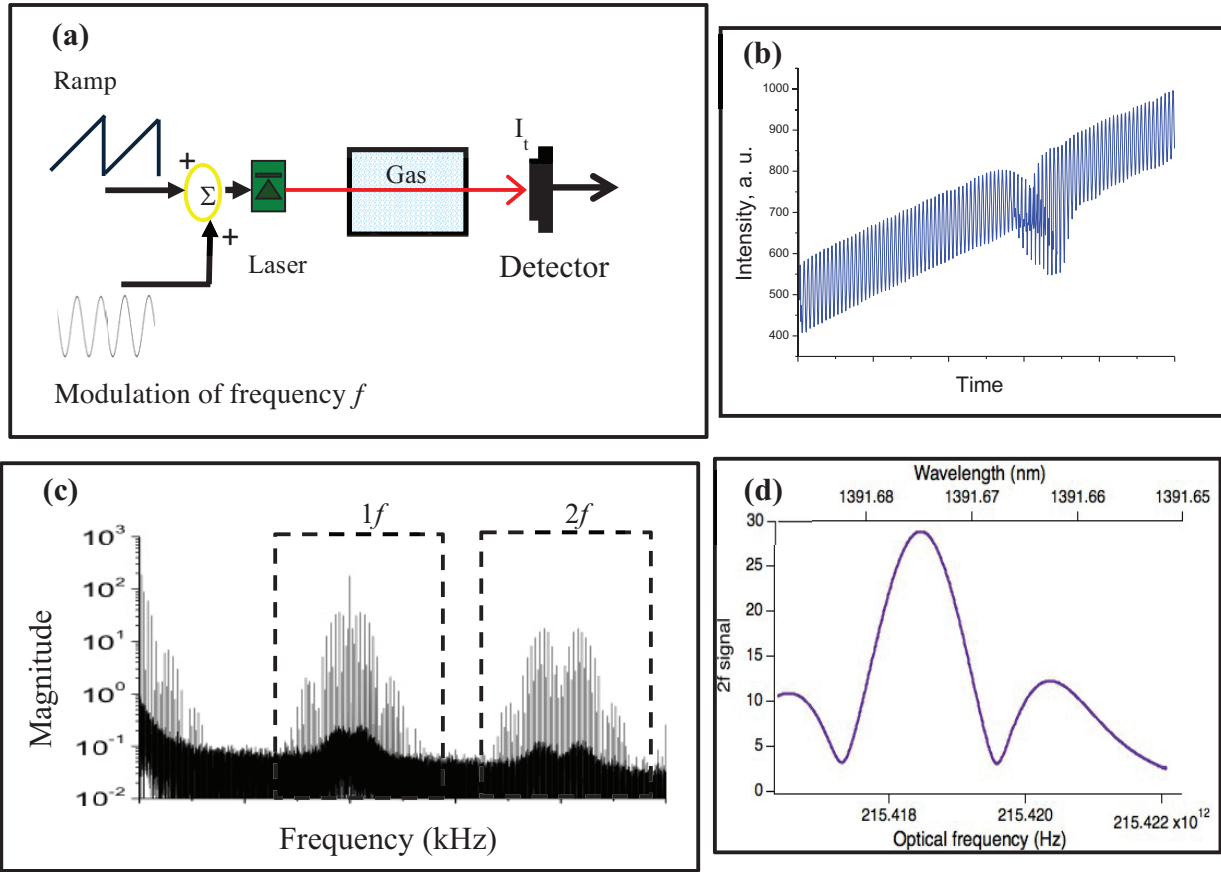
Fig. 1-4. (a) Schematic of scanned wavelength modulation spectroscopy (WMS). The sum of a slow ramp and a fast modulation is applied in current form to the laser, which will ramp in intensity and wavelength. The laser light will then pass through a gas sample to a detector, which will result in harmonic signals in the detector signals. (b) An example of the ramping intensity as a function of time, with absorption occurring part way through the ramp. (c)The FFT of a signal such as (b), where signals are present at multiples of the fast modulation frequency, *f*. (d) An example of the 2*f* signal as a function of wavelength that is measured by passing the raw transmission through a lock-in amplifier 2*f*.

This fast modulation of intensity and wavelength modulation results in a series of harmonics in the detector signal at multiples of *f*, as shown in Fig. 1-4(c). These harmonic signals are isolated using a lock-in amplifier, which acts as a band-pass filter. The work presented in this dissertation uses a digital lock-in amplifier that follows the work of Ref. [22]. If multiple lasers are used, each laser is modulated at a different frequency so that the signals can be isolated from a single detector using the lock-in amplifier. This approach shifts the measured signal to higher frequencies where laser noise is lower, enabling more sensitive measurement of gas thermodynamic properties than TDLAS. We utilize the second harmonic, denoted *2f*, because it is mainly sensitive to changes in absorption, while maintaining a zero baseline if

there is no absorption [23]. An example of a 2*f* signal of H_2O absorption can be found in Fig. 1-4(d). Normalization of the second harmonic signal, 2*f,* by the first harmonic signal, 1*f,* enables calibration-free operation and eliminates the dependence of the signal on intensity fluctuations and makes the sensor robust against beam steering, window fouling, and particulate matter in harsh environments [24]. This advantage is critical in combustion environments as the intensity will fluctuate significantly. An example of a 2*f*/1*f* signal can be found at the bottom of the flow-chart shown in Fig. 1-5. Many groups have utilized WMS to sense temperature and species mole fraction in a variety of combustion environments from atmospheric flames to shock tubes [24–32].

As with other forms of absorption spectroscopy, the most direct way to calculate temperature and species mole fraction from a WMS signal is by fitting a model to the measured signal to extract integrated absorbance. Recently, it has been shown that by scanning the mean laser wavelength all the way across an absorption transition while the laser wavelength is modulated for WMS, the integrated absorbance can be extracted through a fitting routine to the WMS signal [16,17,29]. We utilize a least-squares based fitting routine similar to that proposed by Refs [16,17,29].

In this fitting routine, we simulate the *2f/1f* signal and then fit it to the measured *2f/1f* of the transition of interest. An overview of the fitting routine is illustrated in Fig. 1-5. To begin, we characterize the laser properties, wavelength (λ(t)) or optical frequency variation with time and intensity variation with time, I_0(t), before it enters the gas sample. Relative laser wavelength tuning is measured using a fiber-based Fabry-Perot etalon and the center wavelength is measured using a wavemeter, which combine to make λ(t). The initial intensity, I_0, is measured independently on an identical photodetector for each laser to account for laser nonlinearity.

The third component needed in the simulation is a model of absorbance as a function of wavelength $\alpha(\lambda)$, which is the argument of the exponent in Eq. (1-3). The total pressure, P, and the probed pathlength, L, are measured in the experiment. The absorbing mole fraction, X_{abs}, is an initial guess based on the properties of the system. The linestrength, S(T), of the transition as a function of temperature is calculated
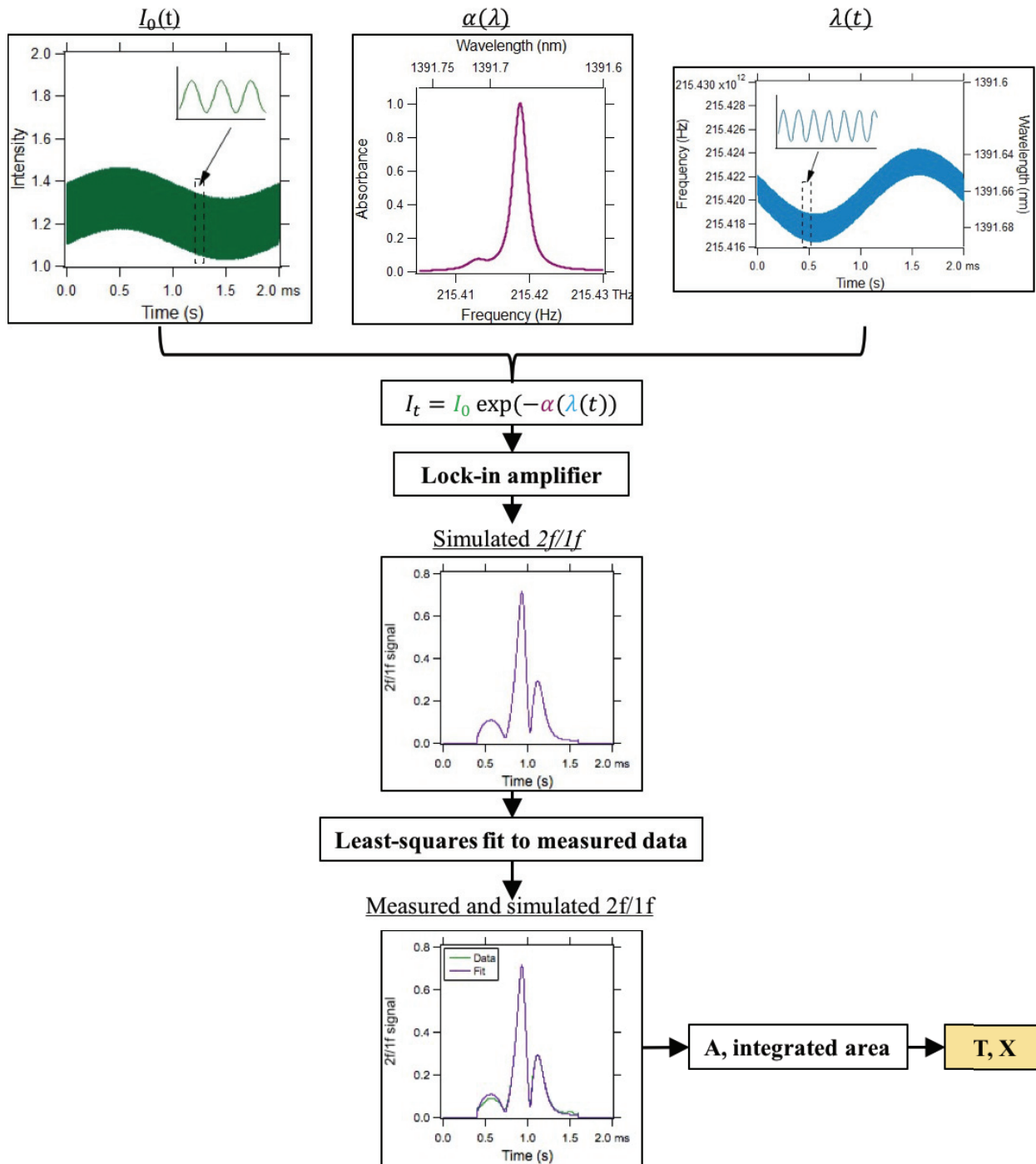
Fig. 1-5. A schematic of this approach is shown in Fig. 1-4(a).

from the measured or calculated linestrength at 296 K [18]. The lineshape function, $\phi(\nu)$, is modeled as a

Voigt profile, as described in Sec. 1.2.1. In this work, initial guesses for the Voigt profile parameters and

S(T) are calculated from the spectral line parameters from databases such as HITRAN2012 and HITEMP 2010 or validated line parameters from Goldenstein and Hanson [20].

These three components are then combined in Eq. (5) to model the transmitted intensity of the modulated light after it has passed through the probed gases species ($I_t(t)$):

$$I_t(t) = I_0(t) exp\left(-\alpha\big(\lambda(t)\big)\right) \tag{1-6}$$

We pass the simulated I_t through an identical digital lock-in as used to process the measured transmitted intensity during an experiment. The simulated WMS $2f/1f$ signal is fit to the measured WMS $2f/1f$ signal, by floating the linestrength-scaled Voigt lineshape profile parameters (linecenter, integrated area, Doppler width, and Lorentz width) in a nonlinear fitting code. Examples of the $2f/1f$ fits for the two H_2O transitions probed in this work are shown in Fig. 1-6. The output of this fitting procedure is the
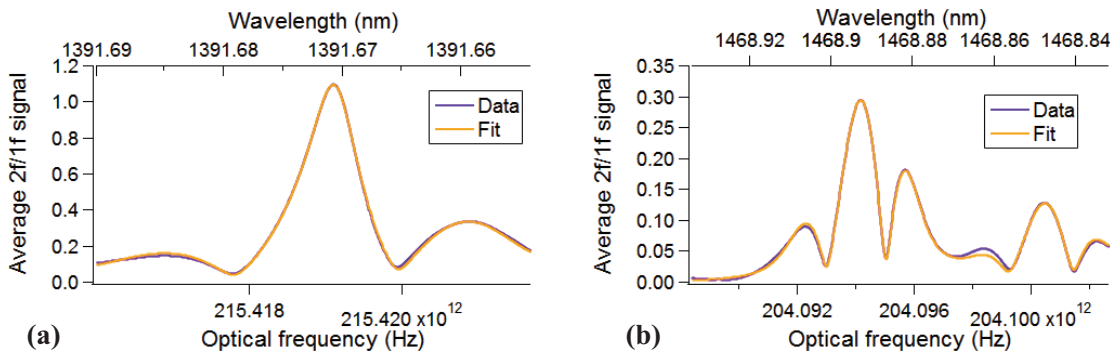
Fig. 1-6. (a) Measured data and fit of 2f/1f signal around 1392nm (b) Measured data and fit of $2f/1f$ signal around 1469 nm

integrated absorbance area of the fitted absorbance profile, which is then used to extract species mole fraction and temperature as per the description in Sec. 1.2.2.

1.3   Dissertation overview

This dissertation achieves the following major goals:

- **Development of an experimental high temperature H_2O and OH spectral parameter database in the 1491nm wavelength region using dual comb spectroscopy (Chapter 2).** We performed the first dual comb spectroscopy measurement above a premixed flame in order to measure high temperature H_2O and OH radical absorption at varying thermodynamic conditions. This data is then

used to perform multi-spectral fitting to extract the spectral parameters for H_2O and OH transitions near 1491 nm.

- **Implementation of a WMS OH sensor at 1491 nm in combustion systems (Chapter 2).** We develop an OH radical sensor based on WMS centered near 1490.9 nm that utilizes the high temperature line-list extracted from the dual-comb spectroscopy measurements as the basis for the analysis. The utility of the sensor is demonstrated by probing a premixed flame and a catalytic combustion system for OH variations. Measurements of OH in the premixed flame match well with 1-D flame calculation trends. We found that under high-velocity conditions the catalytic combustor produces detectable levels of OH while at low flow rates there is no detectable OH. This is the first implementation of *1f*-normalized WMS to probe OH.

- **Characterization of the temperature, H_2O and OH presence in an industrial flame processing system (Chapter 3).** We perform in-situ WMS measurements of temperature, H_2O and OH in an industrial premixed flame interacting with a chilled-roller polymer-treatment system. Measurements with and without the presence of the chilled roller illustrate the effects of the roller on the flame. The measurements performed at the surface of the polymer film are the first experimental demonstration of the connection between OH presence in the flame and the measured oxidation of the processed polymer film.

- **Development of a novel approach for extracting species mole fraction from absorption spectroscopy measurements (Chapter 4).** The varying width of the flames and buoyant jets studied in this work necessitates a technique for estimating the relevant "pathlength" in order to estimate the species mole fraction at the core of a given flow. We develop a novel approach for utilizing computational fluid dynamics simulations to inform the estimation of the relevant beam pathlength. This value is used to calculate H_2O mole fraction inside the heated buoyant jet above a catalytic combustor.

- **Characterization of temperature and H_2O mole fraction profiles in the buoyant jet above a catalytic combustor (Chapter 4).** An understanding of the temporal and spatial variation in the heated, buoyant jet above a catalytic combustor is essential for optimizing its use in industry. We utilize WMS to probe the temporal, vertical and horizontal temperature and H_2O mole fraction variation in the buoyant jet above a rectangular catalytic combustor. This presents the first characterization of the thermodynamic properties of a buoyant jet above a catalytic combustor.

- **Extension of the WMS technique to large modulation depths to measure broad absorbers (Chapter 5).** Traditionally WMS has been limited to narrowly-absorbing molecules, such as those at room pressure or small molecules. We utilize a MEMS-VCSEL laser to extend the technique to larger tuning ranges to measure samples that absorb broadly in wavelength, such as high pressure systems or large hydrocarbons. We illustrate the technique on high-pressure mixtures of CO_2 in air that are 2.5 times higher density than previously published WMS measurements. The agreement between the measured data and the model developed to accommodate the non-linear laser tuning parameters suggests that this technique can be used in the future for future measurements of species mole fraction.

2 Wavelength Modulation Spectroscopy of OH Radical in an Industrial Flame

2.1 Introduction

The hydroxyl radical (OH) is of interest combustion diagnostics because of its importance to combustion kinetics and its use in manufacturing. Because it is a prevalent intermediate in combustion, OH can indicate flame structure and combustion completeness. In manufacturing settings, OH stimulates surface treatment of polypropylene [33,34] and also appears in dielectric discharge plasmas used for material and gas stream processing [35–38]. Diagnostics that provide temporal and spatial measurements of OH can aid in optimizing the operation of industrial flame systems. However OH is difficult to measure in industrial settings because extractive sampling techniques such as gas chromatography are not informative (OH is highly reactive and temperature sensitive), and in-situ measurements are complicated by high temperatures, limited access, and generally harsh deployment conditions.

A wide range of laser techniques have been applied to the in-situ detection of OH radical. Laser induced fluorescence (LIF) and planar laser induced fluorescence (PLIF) have been used with great success to image OH concentrations in many combustion applications [39–43]. Maillard *et al* used emission spectroscopy to measure OH emission from 1100-2700 cm^{-1} in an oxyactetylene flame [44]. These methods have provided measurements of small quantities of OH radical in a variety of combustion settings; however, they require some combination of high-power laser equipment, significant optical access, and/or sensitive optical sub-systems that make these approaches challenging for industrial application and not optimal for real-time monitoring.

Laser absorption spectroscopy is an excellent option for probing industrial combustion and plasma systems because it is quantitative, relatively simple, can probe large systems, and requires only one or two small optical ports [45]. In laser absorption spectroscopy, the thermodynamic properties (temperature, pressure, etc.) and concentration of a species of interest can be measured by their relationship to the absorption of laser light with a photon energy matching the energy of a quantum mechanical transition of the target species. Various research groups have used absorption spectroscopy to probe the electronic

14

transitions of OH in the ultraviolet-visible (UV-Vis) range for a variety of applications including shock-tubes, engines and the atmosphere [36,43,46–49]. Although the electronic transitions of OH in the UV-vis range are very strong, it can also be desirable to probe weaker ro-vibrational transitions at near-infrared (NIR) wavelengths. NIR sensors are desirable because of the low-cost, fiber-coupled nature of the available lasers. Despite this, there has been limited work on OH absorption spectroscopy in this region. Both Peeters *et al* and Rutkowski *et al* used cavity-enhanced absorption techniques near 1.5 um to detect OH concentrations in flame environments [50,51]. Both works are excellent demonstrations of OH detection in the near-infrared; however, cavity-enhanced systems do not scale to large, long-term industrial deployment.
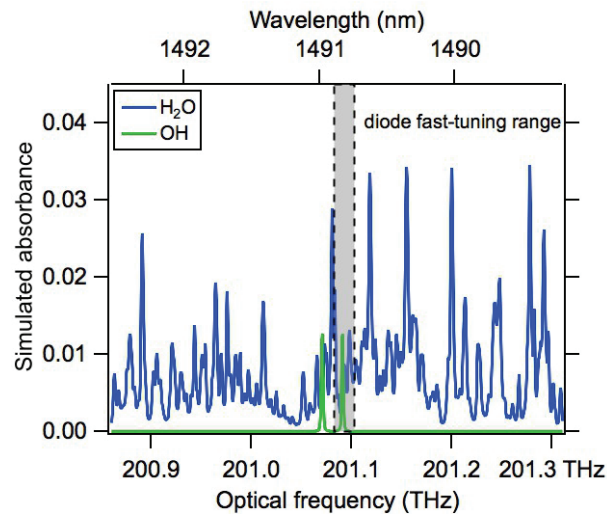
Fig. 2-1. Simulated absorbance of 15% H2O and 0.3% OH mole fraction from 200.9-201.4THz (1489-1493 nm) using HITEMP 2010 for OH and the spectral database developed in this paper for H2O. Both species were simulated at 2200 K, 820 mbar, and a pathlength of 30.7 cm. Shaded region indicates tuning range of DFB diode laser used for WMS measurements. The range of the dual – frequency comb spectrometer extends beyond the edge of the plot from 196.2-217.2 THz (1380-1528 nm).

Because WMS is a form of absorption spectroscopy that achieves higher sensitivity than traditional direct absorption spectroscopy by reducing the effects of system noise and intensity fluctuations, it is an ideal measurement technique for an OH sensor. Aizawa *et al* previously demonstrated the use of WMS to detect OH radical near 1.55 um [52,53]. These papers highlight the challenge of making accurate OH

15

measurements because of interference from high temperature H_2O absorption. In this work, we build on the work of Aizawa *et al* by probing a different OH transition at 1491 nm and characterizing the overlapping H_2O absorption. Furthermore, we utilize 1*f* normalization of the 2*f* signal to remove beam steering problems and improve upon the fitting routine to reduce uncertainties in extracted thermodynamic values.

It is not possible to find OH transitions in the NIR that are free from significant (10-80%) interference from H_2O. The overlap between the absorption of OH and H_2O in the 1490-1492 nm region is shown in the simulated absorbance using the H_2O database that is developed later in this paper in Fig. 2-1. This overlap is significant because a WMS measurement detects the combined absorption of any overlapping species. In order to calculate OH mole fraction from the measured WMS signal, a model of the underlying H_2O absorption must be included in the fit of the measured signal to account for the added signal from the overlapping absorption. Although spectral databases such as HITRAN or HITEMP contain absorption transition information near 1491 nm for H_2O, the high temperature H_2O parameters in this wavelength region are extrapolated from ambient conditions and have never been experimentally investigated or validated [13,14]. It has been shown by several past researchers that these databases are increasingly uncertain as temperatures approach combustion conditions [15,54,55]. Hence, careful characterization of the H_2O transitions neighboring the strong OH transitions of interest in the 1491 nm range are required in order to develop an accurate OH sensor. We present these characterizations in this paper.

This section describes the development and demonstration of a WMS OH sensor centered at 1491 nm. This new OH sensor is demonstrated in the study of the effect of equivalence ratio on the OH concentrations above a catalytic combustor that is expected to be a radical-free heat source. This demonstration illustrates the future utility of this WMS sensor for combustion and plasma applications. The accuracy of the OH measurement is improved by incorporating the measured spectral line. We include the development of a new high temperature H_2O absorption database near 1491 nm utilizing dual frequency comb spectroscopy and multi-spectral fitting. A premixed ribbon burner system is used as the stable high-temperature environment in which to measure these spectral parameters. The light from a dual-frequency

comb spectrometer is passed through the ribbon burner system operating at several different equivalence ratios in order to measure absorption parameters at different thermodynamic conditions. We then extract linestrength and linecenter for the strongest transitions using the multi-spectral fitting code described in [56,57]. The dual frequency comb spectrometer can measure all of the H_2O and OH transitions simultaneously with broad bandwidth, high resolution, and a well-known wavelength axis to minimize the uncertainty of the extracted spectral parameters [15]. These measurements are the first dual-comb spectroscopy measurements in a flame environment.

2.2 Measurement approaches

2.2.1 Scanned wavelength modulation spectroscopy (WMS) for industrial OH sensing

For the measurement of OH in industrial applications we use scanned WMS because of its kHz time resolution, compact size, relatively low cost, and compatibility with telecom fiber optic cables of the semiconductor diode lasers [58–60]. An overview of the WMS technique can be found in Sec. 1.2.

As discussed in the previous section and shown in Fig. 2-1 an absorption measurement of OH at 1491 nm will also include overlapping H_2O absorption. Therefore, analysis of OH must remove the H_2O absorption contribution in order to isolate the OH integrated absorbance. We measure the temperature and H_2O mole fraction using two diode lasers which probe two interference-free H_2O transitions at 1392 nm and 1469 nm [61]. The integrated areas extracted from these two transitions are used to calculate temperature and H_2O mole fraction following the technique described above. A third diode laser probes the OH transition near 1491 nm. We use the measured temperature and H_2O mole fraction to simulate H_2O absorbance as a function of wavelength in the 1491 nm region, and incorporate this simulated absorbance into the fit of the OH transition. Specifically, the fit treats the OH transition as a floating Voigt lineshape added to the H_2O absorbance. The summed absorbance of H_2O and OH is then incorporated into Eq. (1-3)
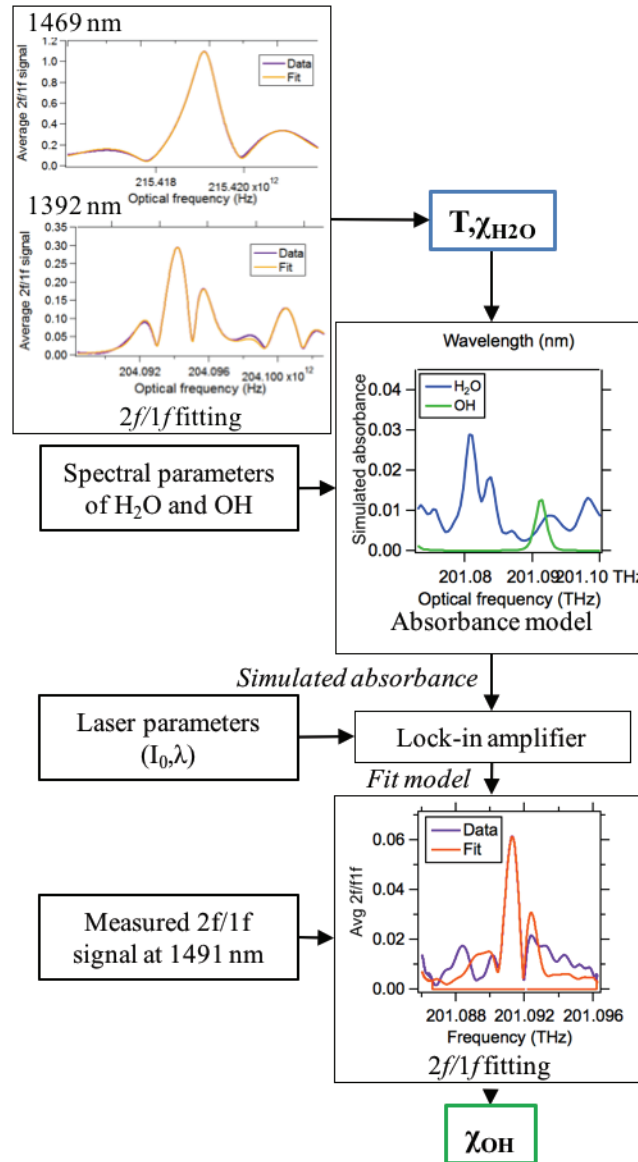
Fig. 2-2. Overview of the fitting routine used to fit the measured WMS 2f/1f signal of the overlapping OH and H_2O features in order to extract OH mole fraction.

with the measured intensity and wavelength variations of the diode laser to simulate the transmitted intensity, I_t. This simulated transmitted intensity passes through the lock-in amplifier to isolate the $2f/1f$ signal, shown in Fig. 2-2. This simulated $2f/1f$ signal is then fit to the measured data by varying the parameters of the Voigt lineshape of the single OH transition until residuals between the model and the measured WMS signal are minimized. The integrated absorbance for the single OH transition that minimizes residuals is used to calculate OH mole fraction.

The absolute accuracy of the OH measurement is highly dependent on the quality of the underlying H_2O database used to simulate H_2O absorbance as a function of wavelength in the analysis. There have been no known database measurements of H_2O in this 1490-1493 nm region, which means that the best available data is from HITEMP 2010. The line parameters of HITEMP in this region have 10-20% uncertainty as they are calculated from quantum models. This uncertainty propagates to significant uncertainty in the OH measurement. Hence, we measure the spectral line parameters of the H_2O transitions in this region using dual frequency comb spectroscopy to improve the accuracy of our OH measurement.

2.2.2 Dual frequency comb spectroscopy (DCS) for H_2O database development

Dual frequency comb spectrometers are an emerging class of laser spectrometers that provide simultaneously broad spectral bandwidth, high spectral resolution, and excellent wavelength accuracy [62]. With these characteristics, the dual-frequency comb spectrometer is well-suited for the development of spectral databases, particularly for high-temperature environments [12,15]. Dual frequency comb spectrometers are recently also capable of field deployment to industrial environments [63,64], but currently at a higher cost and slower measurement rate than tunable diode laser systems. Thus, we use frequency comb spectroscopy here to develop the high-temperature database for interfering water vapor absorption in the region near the OH transition of interest, but still apply tunable diode laser WMS for the primary industrial OH sensor.

The dual-comb spectrometer employed here consists of two linear-cavity, Er-doped fiber frequency comb lasers with a 200 MHz pulse repetition rate. Each comb is individually amplified using erbium-doped fiber amplifiers and then spectrally broadened with a section of highly non-linear fiber (HNLF). In the optical frequency domain, each comb produces hundreds of thousands of modes, which appear as narrow linewidth "comb teeth", spaced by the pulse repetition rate of the laser. The broadened spectrum is then spatially filtered to the wavelength range of interest using a grating-based filter. This filtered light then passes through the gas sample of interest to probe the absorption in the NIR and infer the thermodynamic properties.
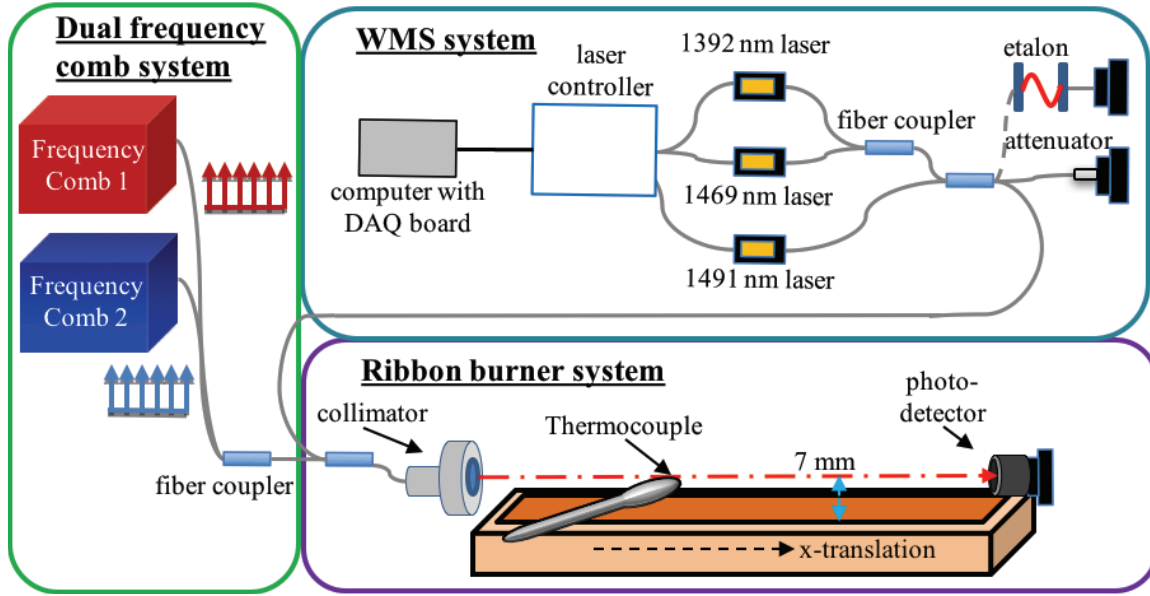
Fig. 2-3. Schematic of the optical setup used for all ribbon burner experiments. (left) Light from two frequency combs is combined to pass across the flame 7 mm above the edge of the burner for extraction of high temperature spectral parameters. (top-right) Experimental setup for WMS OH sensor in the premixed flame of the ribbon burner. (bottom-right) Thermocouple is mounted on a translation stage that passes the thermocouple through the beam in the flame to test for flame uniformity.

Once the light from both lasers passes through the gas sample, they are interfered on a single photodetector. In order to read the signals from each comb tooth, the two combs are stabilized to slightly different pulse repetition rates, which results in a different frequency spacing of the comb teeth for each laser. Therefore, when the lasers are combined, the difference between corresponding "comb teeth" results in a unique RF heterodyne frequency at an integer multiple of the difference between repetition rates, Δf_{rep}. The resulting time-domain signal on the detector is a series of interferograms which repeat at the difference frequency between the two comb repetition rates. A Fourier transform of these interferograms reveals the transmission spectrum including attenuation due to absorption from the measured gas. Further description of the specific DCS method employed here can be found in Ref. [65] and the spectrometer is further described in Ref. [64,66,67]. The filtered light from both combs is combined and passed through the flame (as shown in Fig. 2-3), yielding a broad and precise transmission spectrum.

2.3 High-temperature H₂O absorption database development using dual-comb spectroscopy in a premixed flame

We utilize dual frequency comb spectroscopy (DCS) measurements in a well-characterized flame to develop a high-temperature H_2O absorption database near 1.5 um. The absorption line parameters are extracted from DCS data using the multispectral fitting code described in Refs [56,57] . This section will provide an overview of the database extraction process, as highlighted in Fig. 2-4.

Before we can use the multi-spectral fitting code to extract database line parameters, we must provide it with three inputs: an absorption database to provide seed input values for the location, strength, and shape of transitions, transmission data that incorporates the lines of interest, and uniform and well-known thermodynamic properties (temperature, pressure, etc.) along the laser line-of-sight. We utilize the H2O line parameters from HITEMP 2010 for the seed absorption database [13]. DCS measurements near 1491 nm at three different flame conditions provide the input transmission data. Fits of absorbance data from the same DCS measurements in a wavelength region with a published experimental database provide the line of sight thermodynamic properties of the flame. The multi-spectral fitting routine uses all three inputs to create transmission models that are fit to all three data sets simultaneously to produce the set of desired line parameters. The fit results in a list of lineshape parameters for every transition in the wavelength region validated over the temperature range of the input data. We then compare simulations created using the new high temperature H_2O database and HITEMP 2010 to measured DCS data at a fourth premixed flame condition.

2.3.1 Transmission measurements

The most effective way to empirically producse quantum transition parameters is to provide measured transmission at different temperatures, pressures, and species mole fractions. Many of the H_2O transitions measured in combustion conditions near 1491 nm are not detectable without cavity enhancement unless they are at high temperatures, so we require a gas sample above 1700 K containing sufficient H_2O to generate detectable absorption for stable fits. By probing a premixed flame, we can achieve high temperatures in a uniform manner. The burner systems used in this work for extraction of

21

line parameters is a ribbon burner, which is a burner consisting of a series of small flame jets [1]. These burners have been shown to produce stable flames that result in uniform temperature fields that can be used for industrial processing [68]. Previous work, such as that done by Rutkowski *et al*, measures spectral line intensities in uniform, premixed flames [54].
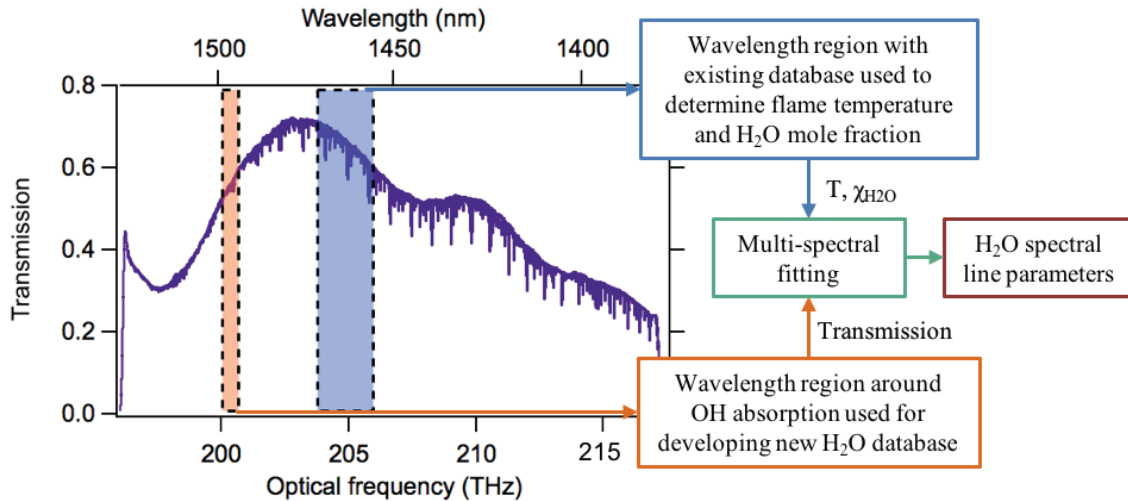
Fig. 2-4. Flow chart of high temperature, H_2O absorption database development. Purple trace is transmission measured by dual-frequency comb spectroscopy above a premixed flame combusting at 90 W/cm^2 and ϕ=0.9. Shading highlights wavelength regions used to provide transmitted intensity (orange) and temperature and H_2O mole fraction (blue) inputs to multi-spectral fitting routine. Orange region contains OH absorption transition used in WMS sensor. H_2O transitions in the blue region have previously been validated by Schroeder *et al* [15]. The multi-spectral fitting routine uses these two inputs from several spectra to extract a new database of H_2O spectral line parameters.

The ribbon burner combusts premixed methane and air at controlled conditions, as described in Ref. [58]. Low power fluxes, approximately 90 W/cm^2, were selected to keep the visible flame short and velocities low. By keeping the flame short, the laser can probe the product gases above the visible flame at a distance close to the burner surface, which helps to minimize non-uniformities across the flame due to buoyancy-driven necking and entrainment of surrounding air (which occurs at larger heights above the burner). Air and fuel flow rates were adjusted to achieve varying fuel-air equivalence ratios while maintaining a consistent flame height. The laser light from the frequency combs passes the length of the burner at approximately 7 mm above the surface, as shown in Fig. 2-3.

The flame conditions and reactant flow rates for four probed conditions are given in Table 2-1. Data using the dual comb spectrometer is collected at each of the four conditions for thirty minutes and a

background data set is collected for twenty minutes while the air is flowing at 100 SLPM. A sample of the transmission spectrum is shown in Fig. 2-4, with the gold region highlighting the wavelength range of interest for transmission measurements. The thirty-minute averaged transmission data for three out of the four conditions are used with the background data as an input for the multi-spectral fitting. The fourth case, condition #3, is kept as a test case to validate the spectral parameters measured from the other three cases.

Condition #	Fuel (SLPM)	Air (SLPM)	Equivalence ratio	Power flux (W/cm^2)
1	6.28	76.1	0.8	79
2	7.00	75.3	0.9	88
3	7.36	75.3	0.95	93
4	7.70	74.6	1	97

Table 2-1. Flow parameters of four trials measured in absorption line parameter extraction study

2.3.2 Line-of-sight thermodynamic properties of the premixed flame

In order to minimize uncertainty in the extracted line parameters, it is important to create a known, spatially-uniform thermodynamic profile along the laser beam. We characterize the uniformity of the ribbon burner test bed by probing the temperature profile along the beam path with a type-K thermocouple. The thermocouple bead is 1.65 mm, approximately the size of the beam diameter, which was chosen to best measure the relative temperature directly along the laser beam. The thermocouple is placed in the beam path on a horizontal translation stage, as shown in Fig. 2-3. Fig. 2-5 shows the thermocouple-measured temperature normalized by the maximum temperature. There is 1.4% maximum variation measured between the bounds of the burner (denoted by gold-dash lines), and a steep gradient on each side. Similar uniformity is achieved for all four trials. In addition to demonstrating the uniformity across the flame, the width of flat-top region, 297 mm, provides the pathlength of probed gases to be input to the multi-spectral fitting program.
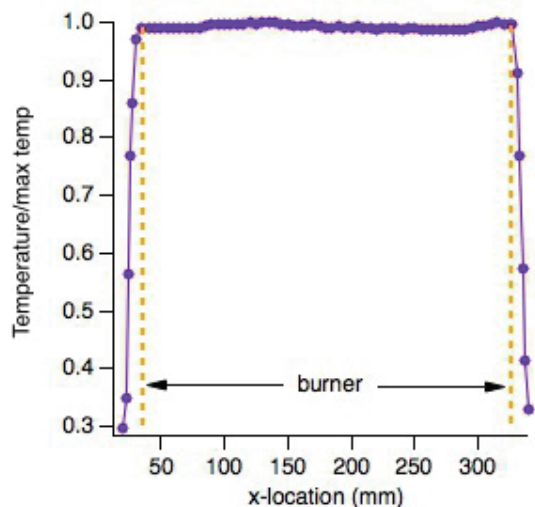
Fig. 2-5. Temperature measured using a type-K thermocouple in the beam path normalized by the maximum measured value.

The thermocouple measurements are able to characterize the uniformity along the beam path, but are not able to accurately measure the absolute temperature due to radiative, convective, and conductive losses around the thermocouple tip. Instead, we utilize the dual comb spectrometer measurements from 1455.3-1469.5 nm (204-206 THz) where a high temperature database has already been created using a tube furnace [15] to calculate thermodynamic properties for each condition. The transmission in the wavelength range highlighted in the blue box in Fig. 2-4 is fit with a simulation of the expected absorbance to extract the temperature, H_2O and OH mole fractions. The fitting routine uses line parameters provided by Schroeder *et al* [15] for H_2O and HITEMP 2010 [13] for OH to perform the broadband fitting approach described in Ref. [69]. The resulting measured thermodynamic properties for all four trials are shown in Table 2-2.

Condition #	Equivalence ratio	Measured Temperature (K)	Adiabatic temperature (K)	Measured H_2O mole fraction	Expected H_2O mole fraction	OH mole fraction
1	0.8	2019	1994	0.162	0.153	0.00275
2	0.9	2119	2130	0.181	0.169	0.00354
3	0.95	2154	2184	0.187	0.176	0.00389
4	1	2165	2220	0.191	0.183	0.00385

Table 2-2. Flame conditions for DCS measurements to extract absorption transition parameters near 1491 nm and to text new database.

2.3.3   High-temperature absorption database

We use three of the four measured conditions to create the absorption database, leaving the data condition #3 to test the experimental database. To begin, we apply a 3×10^{-25} linestrength filter to the HITEMP database to reduce 83,000 lines in the 1489-1492.5 nm (200.8-201.4 THz) spectral region into a seed database that provides the initial guesses for the fitting algorithm. This threshold is evaluated at 2000 K using the temperature-dependent linestrength equation from Ref. [18] to reduce the seed database to 453 H_2O lines and four OH lines. The lines above this threshold produce absorption above the noise floor in the measured thermodynamic range and provide adequate spectral density to compensate for measured absorption that is unaccounted by the seed database linestrengths. The multi-spectral fitting routine uses the line parameters from the seed database as initial guess values combined with the measured thermodynamic properties to simulate absorbance as a series of Voigt profiles. This simulated line-by-line absorbance from H_2O and OH combines with a 13th order Chebyshev polynomial to represent the baseline laser power spectrum to produce a transmission model that is compared to the measured transmission for a given condition. Residuals between this model and the measured transmission spectra are calculated for each condition.

The multispectral program iteratively fits the Chebyshev baseline and H_2O spectral parameters to the measured transmission spectra for numerical stability. An example of this fitting is shown in the top panel of Fig. 2-6, which shows the measured relative transmission for condition #2 and the Chebyshev baseline. First, the Chebyshev polynomial coefficients are fit to each transmission spectrum using the seed database absorption model. Then, the reference linestrengths S_{296} are individually added to the fit to reduce systematic residuals across all the spectra. Once the linestrengths are no longer able to reduce the multispectral residual, linecenters are added alongside the floating Chebyshev polynomial and linestrengths. All linecenters are scaled to burner conditions using the HITEMP air-shift parameter with a temperature-dependence exponent of unity [12]. The OH line parameters are fixed at HITEMP values, because there was no independent measurement of the OH mole fraction. The spectral parameters of the 28

H2O doublets in the spectral range are constrained to each other according to the procedure in Schroeder *et al* [15].
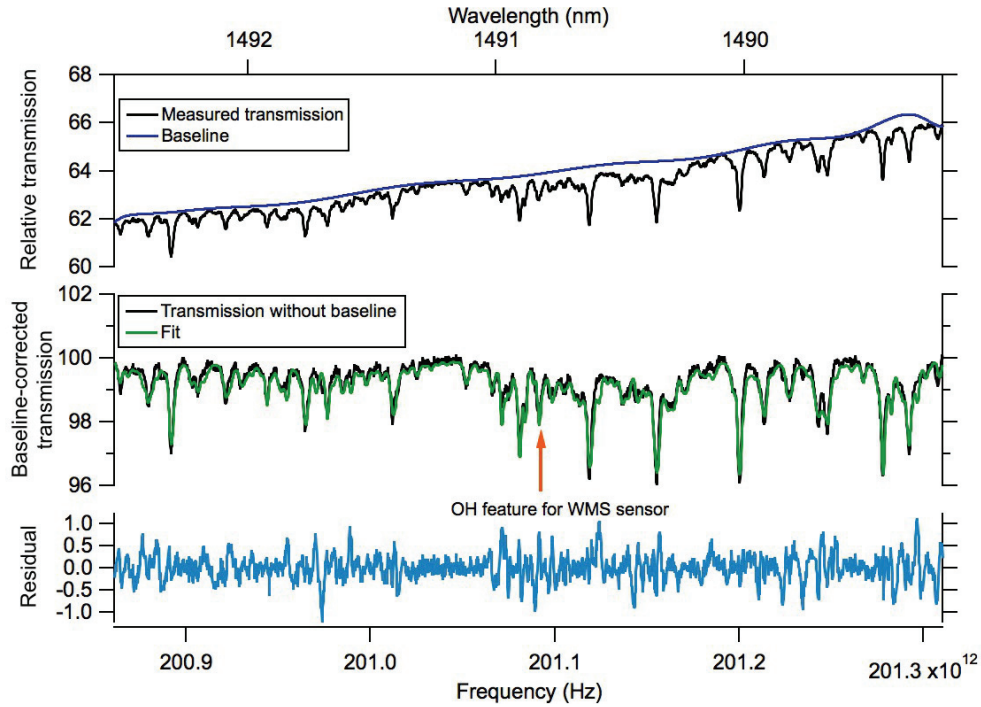
Fig. 2-6. (Top) Relative transmission measured during trial 2 with baseline fit in multispectral analysis. (Middle) Baseline-corrected transmission (black), multispectral fit result (green), and fit residual (blue).

The linecenters were evaluated using a simplification of the full Hartmann-Tran model due to limitations of available database parameters and measured thermodynamic conditions. The multi-spectral fitting uses the air-shift HITEMP values for foreign-shift, which we scale to 2000 K using the temperature scaling validated by Schroeder *et al* [70] and assuming an power-law exponent of *n*=1. assumes a temperature dependence of the shift to be 1 and evaluates the temperature scaling law at 2000K. The self-shift was fixed to zero because HITEMP does not provide *ab initio* coefficients and Schroeder *et al* was not able to observe a non-zero trend in the H2O self-shift in a multispectral fit to a neighboring spectral region [15].

Using the initial database parameters provided by HITEMP 2010, we iterated the multi-spectral fitting routine until it was numerically stable. First, 103 linestrengths and the 13th-order Chebyshev polynomial

26

www.manaraa.com

baselines were floated. Once the 103 lines were selected to produce numerically stable fits, we iterate the

fit ten times, using the results from the previous iteration as the initial guess for the next iteration. When a

linestrength became unstable it was reset to its HITEMP value to begin floating again. Once the fit

stabilized, 15 of the corresponding linecenters were allowed to float as well. As before, unstable parameters

were reset to their initial guess values to begin the iteration process again until a fit that was stable over ten

iterations was found. The resulting linestrengths and linecenters are the resulting experimental database.

The measured transmission spectra for condition #2, normalized to 100, is shown in black in the middle

panel of Fig. 2-6 with a simulation of the final database and the corresponding residuals on the bottom

panel.
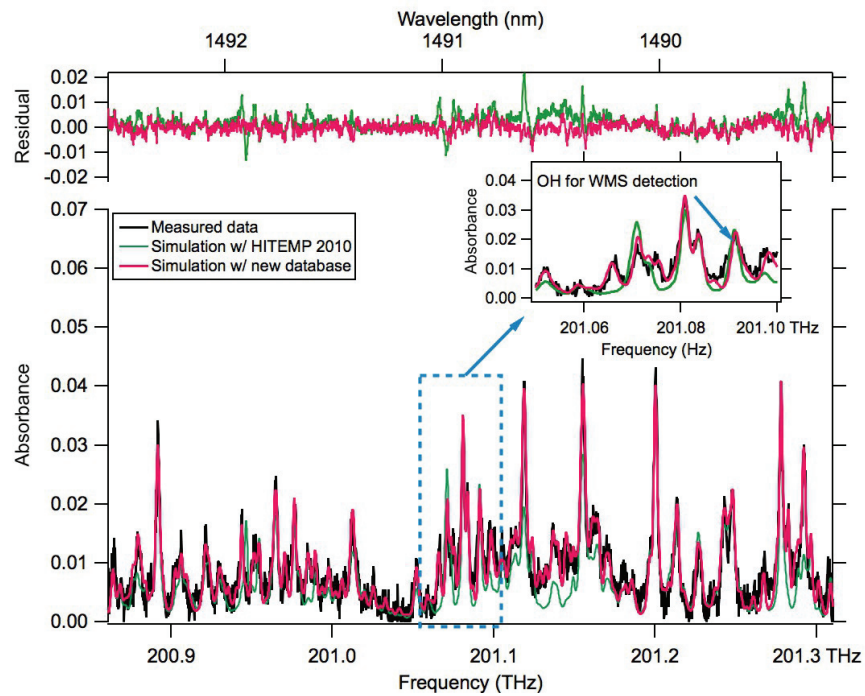
Fig. 2-7. Measured absorbance as a function of optical frequency as compared to absorbance simulated with HITEMP 2010 (green) and the experimental database (pink) at the measured thermodynamic properties. The resulting residuals between model and fit are shown as the top traces.

Having extracted absorption line parameters for H_2O in the 1489-1492.5 nm (200.8-201.3 THz) region,

we test the new database using the measured spectrum of condition #3 (ϕ=0.95, 93 W/cm^2, which was not

used for the creation of the database). The measured absorbance is shown in black in Fig. 2-7. We compare

the measured absorbance to simulations of absorbance created as a series of Voigt profiles calculated from

the measured thermodynamic properties measured in Table 2-2 and the spectral parameters from HITEMP 2010 (green) or the experimental line list (pink). Each simulation is compared to the measured data to produce the residuals shown in the top axis of Fig. 2-7.

It is clear from Fig. 2-7 that the residuals for the simulation using the experimental database are smaller across almost all frequencies, suggesting the experimental database improves on HITEMP 2010 under these conditions. The inset of Fig. 7 illustrates the improved agreement near the OH transition that will be used by the WMS sensor. Eight of the new linecenters deviated less than 0.025 cm^{-1} from HITEMP 2010 values while 52 linestrengths deviate less than 50% and only 18 of the new linestrength values deviated from initial guess values by more than 300%.

Uncertainties of the extracted line parameters fall into two categories: line-specific and non-line-specific. The non-line-specific uncertainties are based on the systematic uncertainties of the experiment and will be the same for all extracted line parameters. If we assume that from the temperature dependent linestrength equation in Ref. [18] we can define $S(T)$ as Eq. (2-1)

$$S(T) = S_{296K}\beta(T)$$

(2-1)

we can then plug this into Eq (1-4) to give

$$S_{296K} = \frac{A}{\beta(T)PXL}$$

(2-2)

We can then estimate the transition independent uncertainty of the extracted reference linestrength to be the sum of the uncertainties of each of these quantities in quadrature

$$\frac{\delta S_{296K}}{S_{296K}} = \sqrt{\left(\frac{\delta A}{A}\right)^2 + \left(\frac{\delta\beta}{\beta}\right)^2 + \left(\frac{\delta P}{P}\right)^2 + \left(\frac{\delta X}{X}\right)^2 + \left(\frac{\delta L}{L}\right)^2}$$

(2-3)

which is approximately 7%. This uncertainty assumes 0.5% uncertainty in A from frequency comb accuracy [71], 5.3% uncertainty in β from temperature uncertainty, 0.5% uncertainty in P from the pressure sensor, 3.3% uncertainty in X from DCS fitting and 3% uncertainty in L from the thermocouple study.

28

Line-specific uncertainty comes from both the statistical uncertainty of the multi-spectral fitting routine and the stability of the fit. The statistical uncertainty for each fit parameter is extracted with the new line parameter and is tabulated in the Appendix A. We determined the fit stability by perturbing the S_{296K} values by +/- 10% and iterating the multi-spectral fitting with these new parameters. This uncertainty is also tabulated with the new database parameters in the Appendix A.

2.4   Demonstration of WMS OH radical sensor

While the broadband, high-resolution nature of DCS provides greater accuracy and flexibility, WMS is a robust, high time-resolution, lower-cost option for a targeted measurement of particular species in a particular measurement configuration. As described in Sec. 2.2.1, OH mole fraction is extracted from measured WMS signals by fitting a model of the signal to the data in order to extract the integrated absorbance. Therefore, we utilize the measured experimental database extracted from the dual comb spectroscopy measurements as the basis for data analysis in the WMS sensor, as described in Sec 2.2.1, to measure OH radical near 1491 nm. This new WMS sensor is then used to characterize OH in both a premixed flame system, demonstrated in Ref [72], and catalytic combustor, presented here. These two demonstrations demonstrate a step toward industrial implementation of the OH sensor [58].

In industry, catalytic combustors are used as a method for reducing emissions and as a non-reacting heat source. Introducing a catalyst lowers the energy required for the dissociation of combustion reactants, with the goal of obtaining more complete combustion with lower emissions [5,6]. Because the catalyst reduces combustion temperatures to 1400-1600K, we do not expect to find equilibrium OH mole fraction levels above 10^{-4} if combustion is complete. Therefore, sensing OH at the exit of a catalytic combustor can provide insight into the effectiveness of the catalyst at achieving complete combustion, or the health of a catalyst in long-term monitoring applications.

We pass the combined laser light of the WMS sensor three times across the surface of the combustor to probe the product gases exiting the combustor. Four combustor power fluxes were selected from 5-20 W/cm^2. At 5 W/cm^2 the catalytic bed is barely glowing, which suggests low temperatures that are not conducive to the existence of OH. On the other hand, when the burner operates at 20 W/cm^2 there is a visible blue flame at the surface of the catalytic bed that indicates a high likelihood of continued combustion and the possible presence of detectable OH concentrations. At each power flux the equivalence ratio is varied to change the combustion chemistry and conditions at the surface.
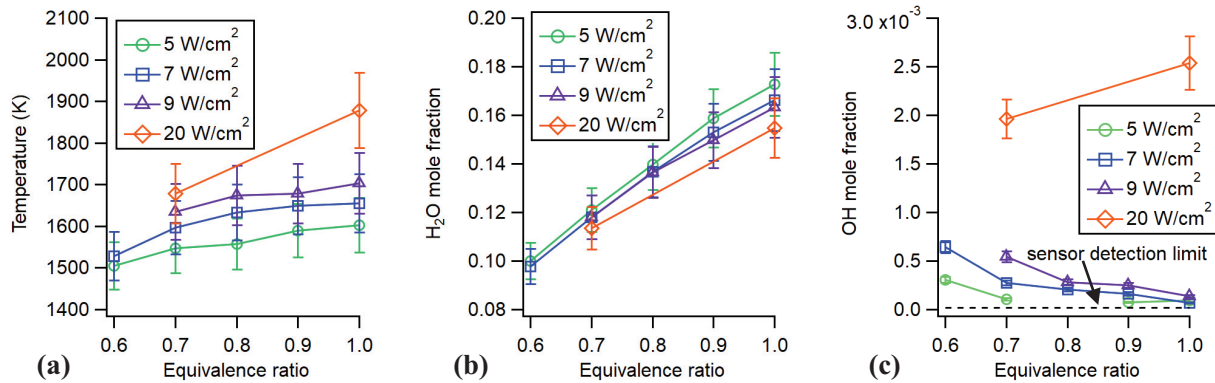
Fig. 2-8. (a) Temperature (b) H$_2$O mole fraction and (c) OH mole fraction as a function of equivalence ratio for a range of power fluxes measured at the surface of a catalytic combustor using WMS. Uncertainty bars for (a) and (b) are 4% and 7% respectively from measurements in a fixed temperature furnace in Sec. 4.3. The uncertainty bars for (c) are estimated from the combined H$_2$O and temperature measurement uncertainties and uncertainty in spectral parameters to be about 11%.

Fig. 2-8(a) and (b) show the measured temperature and H$_2$O mole fraction as a function of equivalence ratio for the four power flux conditions selected. Vertical uncertainty bars are the sensor uncertainty derived from validations under known conditions [61] and the uncertainty of experimental conditions to be 4% and 7% respectively. The increase in both properties with equivalence ratio matches expectations that each will reach a maximum near or slightly above the stoichiometric (ϕ=1) condition. Additionally, the traces in Fig. 2-8 (a) confirm that higher temperatures occur at higher fuel flow rates.

The OH mole fraction variation with equivalence ratio shown in Fig. 2-8(c) does not match the trend for premixed flame combustion, where OH should peak around equivalence ratios of 0.9-0.95 [73]. Time resolved OH mole fraction results indicate that the noise on the measurement is about 1.6x10^{-5} at 1700 K (as compared to 2.0x10^{-4} at 2000 K from data presented in Ref [72]), indicating this is the lowest detectable

level of OH. The uncertainty of OH mole fraction values is approximately 11%, which is calculated by adding in quadrature the uncertainties of temperature, H_2O mole fraction, pressure, pathlength and S(T) as per Eq. (1-4).

Because increased levels of OH are typically associated with elevated temperatures found in premixed flames, it is surprising to see indications of OH radical present above the catalytic combustor as it operates at lower temperatures. Furthermore, for the three lower power flux conditions, the OH levels decrease with equivalence ratio. This trend is the opposite of the temperature increase with equivalence ratio shown in Fig. 2-8(a). In the case of the lowest power flux (5 W/cm^2), the OH mole fraction measured at $\phi=0.6$ is significantly larger than the other conditions that indicate OH levels barely above or below the detection limit. For each power flux, the methane flow rate is held constant and the air flow rate is varied to change the equivalence ratio. Thus, the $\phi=0.6$ case corresponds to the highest air flow rate, and therefore the highest exit velocity for that power flux. The matching trends of OH with air flow rate, instead of temperature, indicate that the catalyst may not have sufficient residence time or catalyst temperature to react all of the fuel and oxidizer at higher flow rate cases. Only the 20 W/cm^2 condition has increasing OH levels with increasing equivalence ratio, suggesting that at this condition flow rates are always too high to complete combustion in the catalyst. Whether this trend is due to a saturation of the available active sites on the catalyst, or residence time issues is not clear, but this condition is not ideal for certain industrial applications where reactive radicals in the product gases of the catalytic combustor are not desired. Overall, these measurements demonstrate the utility of the WMS OH sensor for studying the effectiveness of the catalyst under different conditions or for long-term industrial monitoring of catalyst health.

2.5 Conclusion

In this work, we employ dual comb spectroscopy to develop an accurate and sensitive OH radical sensor based on wavelength modulation spectroscopy near 1491 nm. The first dual comb spectroscopy measurements above a controlled premixed flame are performed in order to develop a high-temperature absorption model for H_2O near 1491 nm. The air and fuel flow rates of the premixed ribbon burner are

adjusted to achieve four different flame conditions for multispectral fitting. Transmission spectra measured through the flame from 1455-1470 nm (where a previously developed high-temperature H_2O database exists [27]) are analyzed to extract average thermodynamic properties for each condition. These properties are combined with measured transmission near 1491 nm in a multispectral fitting routine to extract a new experimental database in that spectral region. Simulations of absorbance using the experimental database are shown be in better agreement with measured absorbance data as compared to simulations derived from HITEMP 2010.

The new experimental database is incorporated as part of a new OH sensor using wavelength modulation spectroscopy at 1491 nm, in order to properly account for unavoidable H_2O interference. The database serves as the basis for simulating absorbance as a function of wavelength for H_2O from 1489-1493 nm, so that H2O is accounted for when measuring the OH contribution of the WMS signal. The inclusion of the new H_2O database changes the measured OH mole fraction by up to 370% over values obtained when using the HITEMP database, and brings values into good agreement with previous measurements under similar conditions [74]. The sensor has an OH mole fraction detection limit of $1.6x10^{-5}$ at 1700K and $2.0x10^{-4}$ at 2000 K with an 75 and 30.5 cm pathlengths respecitively. We then utilize the sensor to probe two different combustion systems of interest – a premixed flame and a catalytic combustor. Measurements of vertical profiles of OH, H_2O, and temperature in the premixed flame follow expected trends. Probing the gases at the exit of the catalytic combustor at a variety of power flux and equivalence ratio conditions indicate the existence of additional combustion above the surface of the catalytic bed at high velocity and/or higher fuel flow rate conditions.

As shown by the demonstrations of the OH sensor in the premixed flame and catalytic combustor, this OH sensor has the potential to be used in a variety of applications in the future. The combined sensitivity of WMS with the accuracy provided by spectral parameter characterization makes the sensor ideal for application to catalytic combustion, plasmas or premixed flame processes in industry. The time-resolved and accurate nature of the sensor   would be ideal for long-term monitoring and control as well.

2.6 Acknowledgements

The text in this chapter primarily comes from an in-prep manuscript:

T. R. Hayden, N. Malarich, D. J. Petrykowski, S. P. Nigam, C. LaPointe, J. D. Christopher, N. T. Wimer, P. E. Hamlington, and G. B. Rieker, "OH radical detection in combustion environments using wavelength modulation spectroscopy and dual frequency comb spectroscopy near 1491 nm," **in prep**, (2018).

The experimental spectral database developed in this work is attached in Appendix A.

3 Characterization of the thermodynamic properties of premixed flames from a ribbon burner interacting with a chilled roller

3.1 Introduction

Flame treatment is one of the most commonly used methods to modify the surface of polyolefin polymer films. The two principal polyolefin films used in industry, polyethylene (PE) and polypropylene (PP), have low adhesion and inherently low surface energy. These films need to be surface-activated to improve adhesion, enable the coating of inks, primers, release coatings, and paints, and improve the strength of laminates [75–77].

To optimize surface oxidation and to achieve a consistent product, the flame processing of polyolefin films requires a high degree of spatial uniformity and precise control of species concentrations and temperature [1,76]. A ribbon burner is an excellent burner design to achieve spatial uniformity, as it is made up of sheets of metal crimped together to produce tightly spaced rows of small premixed flame jets [1]. Most flame processing systems employing a ribbon burner involve impingement of the combustion gases on a film traveling over a chilled roller or conveyor belt, which could have an effect on the flame properties. Therefore, optimizing temperature and species concentrations to improve surface oxidation requires an understanding of the flame thermodynamic properties in the film interaction region, and how the properties tie to various attributes of the surface oxidation [1,76].

Previous relevant characterization work can be categorized into three main areas: surface characterization of polymer films after they have passed over flames, studies of flames impinging on chilled surfaces, and ribbon burner flame characterizations and simulations. There is a body of literature on the surface analysis of the treated polymer surface, including analyses utilizing x-ray photon spectroscopy (XPS) and contact angle measurements [78,79]. There has been extensive work studying premixed flames from other types of burners impinging on chilled surfaces or flat plates; however, these studies focused on the heat-transfer characteristics instead of gas-phase species concentrations and thermodynamic properties [80–87]. These studies suggest that the flame properties and separation between burner and chilled surface have a large effect on the heat transfer from the flame to the surface.

Branch *et al.* studied the effect of burner-to-film gap and equivalence ratio on polypropylene film processing using numerical models from PREMIX and film surface characterizations [68]. Stroud *et al.* used Schlieren imaging to visualize and thermocouples to measure temperatures in the flow fields between a ribbon burner impinging on a chilled roller [88]. The numerical modeling results of Sullivan *et al.* suggest a connection between OH radical and surface wettability based upon computational models and film surface characterization [73]. Additionally, Farris *et al.* highlight the importance of the OH radical in flame chemistry and surface reactions in their review of flame treatment of polyolefin polymers [76]. Using secondary ion mass spectrometry (SIMS), Pachuta and Strobel suggest that OH may be primarily responsible for hydrogen abstraction in film treatment [33]. This series of studies suggest that there is a strong link between OH concentration, and to a lesser degree temperature, with the wettability and adhesion properties of processed films. They also suggest that impingement of flames on chilled surfaces influences flame properties. However, none of the previous studies for polymer film processing performed direct measurement of OH radical, combined with direct measurements of gas phase temperature and film surface properties in the interaction region. Here, we combine in-situ gas-phase measurements of temperature, OH and H_2O concentration in the flame to quantify the impact of a chilled surface on the interaction between the flame and polymer, and relate the gas-phase measurements directly to measured film surface properties for the first time.

Specifically, this study seeks to investigate the impact of the chilled roller on the thermodynamic properties of the flame and determine if there is a connection between OH radical concentration in the flame and increased film adhesion and wettability. The former will facilitate optimization of the flame treatment system to maximize surface oxidation while the latter will provide a clear connection between flame and surface properties. We characterize gas-phase temperature, OH and H_2O mole fraction profiles in the flames using tunable diode laser wavelength modulation spectroscopy (WMS) and the surface atomic composition using XPS. Of the various methods available for in-situ measurements of temperature and species concentrations, WMS is chosen here because the compact, relatively low cost, noise-immune, all-fiber-

coupled design is desirable for future online sensing applications directly in industrial treatment systems [24].

With these tools, we probe three systems: a premixed, unobstructed flame above a ribbon burner, the same ribbon burner premixed flame impinging on a chilled roller, and a premixed ribbon burner flame impinging on a polypropylene film transported through the flame on a chilled roller. Our first study suggests that WMS is an effective measurement tool to probe these industrial premixed flames, and develops baseline temperature and species profiles for the burner system. The second set of experiments quantifies the effect of the chilled roller on the thermodynamic properties of the flame. Finally, gas-phase OH measurements at the surface of the PP film during processing are combined with XPS measurements to directly show that OH is key to surface oxidation.

3.2   WMS experimental setup
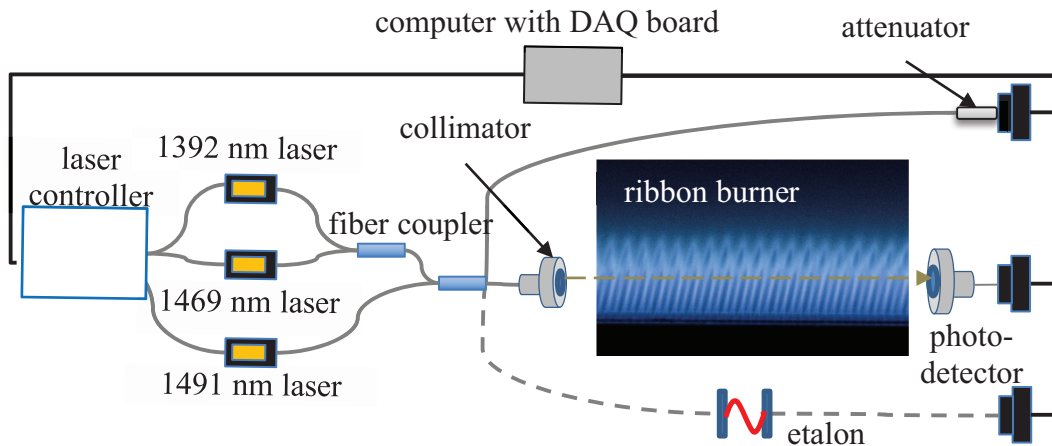
Fig. 3-1. Schematic of the optical setup used for all ribbon burner experiments. Light from all three lasers is either passed across the flame, straight to a detector to monitor the intensity, or to an etalon to characterize wavelength as a function of time.

The WMS sensor uses three distributed feedback (DFB) diode lasers at 1392, 1469, and 1491 nm to probe two H_2O and one OH ro-vibrational absorption transitions, respectively. The measured absorption of these three transitions is used to determine average temperature, H_2O and OH mole fractions across the flame. A detailed description of WMS, the H_2O and temperature sensors can be found in Sec. 1.2 and Ref. [61]. A description of the OH sensor and its analysis is described in Ch. 2.

36

The experimental set up used for the ribbon burner characterizations is shown in Fig. 3-1. Two National Instruments PCI-6110 data acquisition boards supply the modulation voltage to an ILX laser diode controller and acquire the input voltages from the photodetectors. The light from all three lasers is combined and passed to two fibers, one that passes the light through the flame in a triple-pass configuration across the burner via transmit/receive collimators and mirrors, and another that passes the light directly to a photodetector for intensity monitoring or alternatively to a fiber-based etalon (FSR = 636 MHz) to characterize the wavelength modulation. Background absorption of H_2O vapor in the ambient air is measured prior to an experiment by flowing dry air through the burner, and then subtracted from the measured signals during analysis. The vertical variation of the flame is characterized by simultaneously translating the transmit and receive collimators vertically.

3.3   Characterization of unobstructed premixed ribbon burner

Measurements of the unobstructed premixed ribbon burner flame form a baseline with which to compare measurements that include the chilled roller and interaction with PP film. The burner combusts methane and air with a power flux of approximately 500 W/cm^2 in an up-firing orientation. This power flux is within the common operating range of industrial flame processing of PP films. Measurements are made vertically in the flame at 2 mm intervals for the first 1 cm and 5 mm intervals up to 5 cm. We collect three trials at an equivalence ratio (ϕ) of 0.95, which is expected to maximize the peak X_{OH} [4]. In a subsequent series of trials, we varied the equivalence ratio from 0.83 to 1.07. The results of the open flame characterizations are shown in Fig. 3-2. The temperature vertical profiles from all three trials at $\phi = 0.95$ are shown in Fig. 3-2(a). Each data point represents a 30-60 second average. The horizontal uncertainty bars indicate a 3% systematic sensor uncertainty estimated from previous validation measurements in a uniform tube furnace [61]. Because the burner length is large compared to the length of ambient air being probed, the gradients on the edge will not have a significant effect. We estimate that the WMS temperature measurement drops approximately 3% with gradient based on the temperature gradients measured above the ribbon burner in Ref. [89]. The measured vertical temperatures have a steep increase and then stabilize

at approximately 10 mm, which matches well with expected trends in premixed methane-air flames [90]. The stabilization of the temperature suggests that the exothermic combustion reactions near completion at around 10 mm, after which entrainment and heat loss reduces the temperature. The maximum measured temperature is approximately 2100 K, which is slightly below the adiabatic flame temperature of 2240 K for methane combustion in air, as expected due to heat loss. Previous spatially resolved measurements along the laser beam path show that the temperature is uniform along the majority of the path, with sharp temperature gradients back to ambient at the edges of the burner [21]. Based on simulations using the previously measured temperature profile along the beam path, we estimate that the edge effects reduce the WMS-measured temperature by approximately 3% from the actual mean temperature of the uniform central region of the burner.
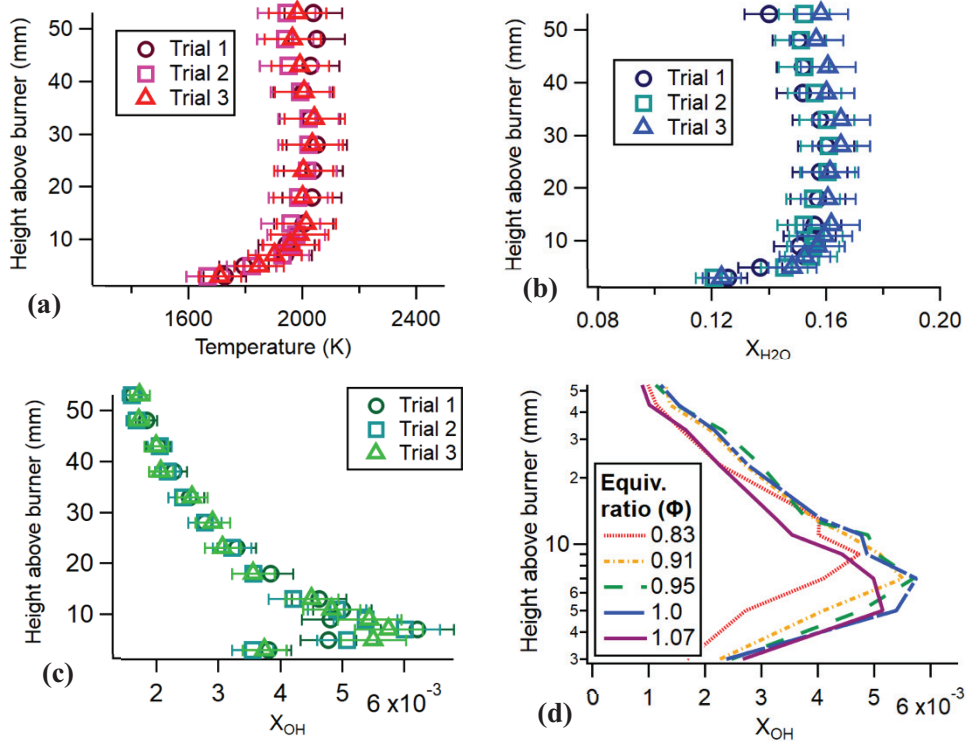
Fig. 3-2. Measured (a) temperature (b) X_{H2O} and (c) X_{OH} vertical profiles in premixed methane/air flame at ϕ= 0.95 and 500 W/cm^2. (d) X_{OH} vertical profiles at different equivalence ratios and power flux 500 W/cm^2.

The X_{H2O} profile shown in Fig. 3-2(b) increases sharply from the surface of the burner and plateaus around X_{H2O} = 0.16.. Equilibrium calculations performed using the NASA chemical equilibrium with applications (CEA) solver at an equivalence ratio of ϕ = 0.95 produce a X_{H2O} value of 0.17. The 6%

38

difference between measured values and the equilibrium values may be attributed to uncertainty in the pathlength correction (which accounts for buoyancy-induced necking above the burner surface in this case) and the pressure measurement used to calculate X_{H2O} [61].

Panels (c) and (d) of Fig. 3-2 show the X_{OH} vertical profiles of the three trials at $\phi = 0.95$ and at five different equivalence ratios, respectively. Unlike the plateaus present in the temperature and H_2O data, the X_{OH} peaks between 2-4 mm above the burner surface, matching simulated OH trends in Ref. [68]. This peak location decreases with increasing equivalence ratio, as shown in Fig. 3-2(d). For these measurements, the methane flow rate was held constant to maintain a stable burner heat flux and the air flow rate was decreased in order to raise the equivalence ratio. The decrease in the peak height above the burner for X_{OH} is the result of the decrease in air flow rate (while holding the fuel flow rate constant), which coincides with a shorter visible flame cone as equivalence ratio increases. According to Fig. 3-2(d), X_{OH} is maximized around $\phi = 0.91$ to 0.95, which matches previous simulations [1]. Hence, the unobstructed measurements suggest that optimal polyolefin film surface activation would be achieved if the product were placed 2-4 mm above the surface of the burner with the flame at an equivalence ratio of $\phi = 0.91$ to 0.95. However, this conclusion assumes that the film and film transport system do not affect flame properties and further motivates the investigation of the effects of the presence of the chilled roller.

The precision of the X_{OH} measurements under our conditions is approximately 10 ppm. The horizontal uncertainty bars on the X_{OH} data in Fig. 3-2(c) represent a 9.5% estimated systematic uncertainty due to uncertainty in the temperature, X_{H2O}, and pathlength measurements. It is important to understand the systematic uncertainty can help understand process repeatability and system control charts in industrial processes. The measured spatial OH trends match well with previous simulations from Branch *et al.*, but differ in absolute value [15]. This could be due either to inaccuracies in the kinetic model from the Branch *et al.* study, bias in the OH measurements, or both. Bias in the OH measurements is difficult to quantify because of the difficulty in performing OH validation measurements (OH is highly reactive, and is therefore only found in significant quantities in reacting systems or very high temperature environments which are

themselves not good environments for validation measurements). Bias in the system could arise from error in the underlying H_2O absorption model used for the 2*f*/1*f* fit, and from the lack of experimentally validated OH linestrengths. The absorption parameters in the HITEMP database for OH at 1491 nm are determined computationally, and the H_2O absorption strengths have a reported uncertainty of 5-15% [89].

3.4   Characterization of ribbon burner with chilled roller

The burner was placed beneath a chilled roller, as shown in Fig. 3-3(a). We adjusted the gap between the surface of the burner and the chilled roller to approximately 10 mm so that the roller is approximately 3 mm beyond the tip of the visible flame cones at a power flux of 500 W/cm^2.

Measurements were taken at 1 mm intervals up to 8 mm, and then at 0.5 mm intervals until the surface of the roller occludes the beam. We performed two trials with the roller spinning at 240 rpm, which corresponds to a film speed of approximately 200 m/min. The data are averaged for 30 seconds at each height.

The presence of the chilled, spinning roller has a strong effect on the vertical temperature and species profiles. Fig. 3-3(b) shows the vertical temperature profile between the roller and the burner surface as compared with the average of the three unobstructed measurements at the same power flux and equivalence ratio (solid line). The dashed line indicates the location of the chilled roller. The two trials taken with the roller (circles and squares) are in good agreement. Simulations of the roller and burner show that obstruction by the roller causes slight billowing of hot gases toward the optics at beam heights near the roller surface; however, the temperature gradients at the edges of the high temperature core flow remain steep, and thus the influence on the measured temperature is still small. Compared to the unobstructed case, the gas temperature is reduced at all heights and does not increase abruptly above the surface of the burner. Instead, the profile is uniform with a variation of 3-4% until approximately 7.7 mm above the surface. At

this height, the temperature begins to drop toward the surface of the chilled roller. The measurements confirm that the roller introduces significant heat loss and perturbation to the flame structure.
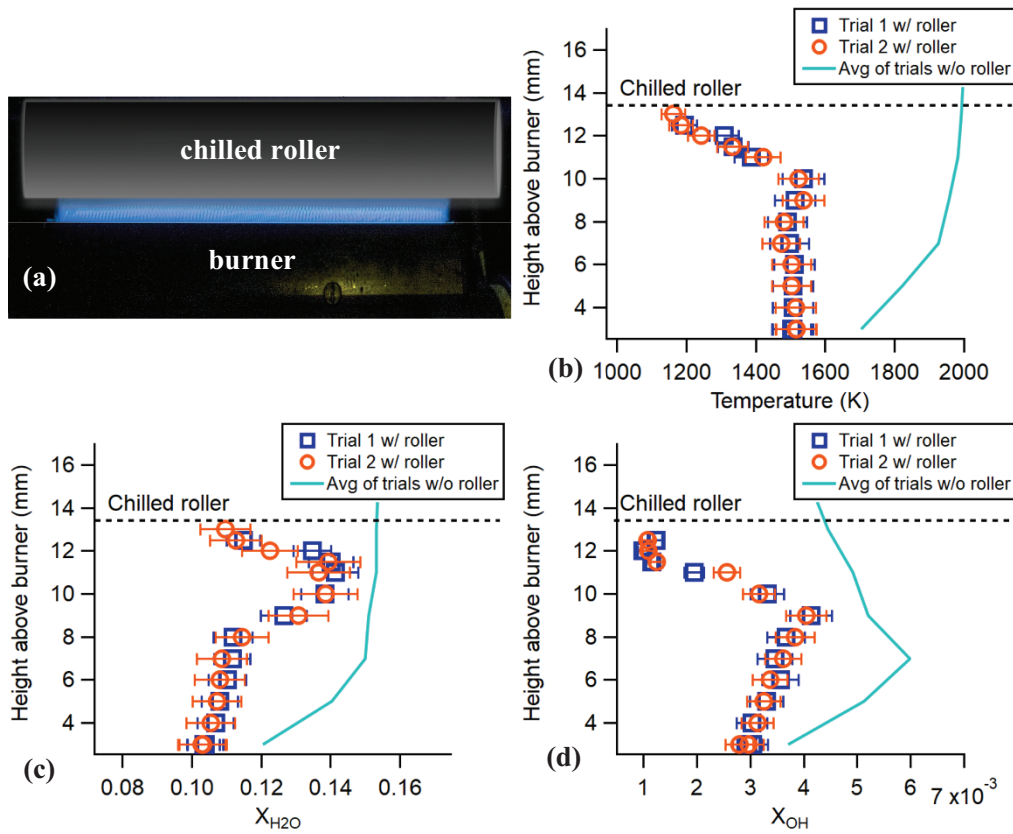
Fig. 3-3. (a) Photograph of ribbon burner flame impinging on the spinning chilled roller (roller is photographically enhanced for clarity). Measurements of the vertical profiles of (b) Temperature (c) X_{H2O} and (d) X_{OH} at $\phi = 0.95$ and 500 W/cm^2 with the chilled roller at 11 mm.

As with temperature, X_{H2O} is also reduced at all locations as compared with the unobstructed case. In contrast to the temperature profiles, the measured X_{H2O} shown in Fig. 3-3(d) increases steadily from the surface of the burner until approximately 5 mm above the burner surface. For the next 3 mm (until 8 mm) the X_{H2O} increases rapidly. This rapid increase suggests that reactions are delayed by lower temperatures induced by the presence of the chilled roller. Above 8 mm, the X_{H2O} decreases, which could be caused by the entrainment of cool, dry air by the roller.

The vertical X_{OH} profile also changes with the introduction of the chilled roller. The measured values of X_{OH} are reduced and peak at a higher location above the burner as compared with the unobstructed

case. This further supports that slower kinetics are induced by the lower temperatures when the roller is present. The sharp decrease in X_{OH} toward the surface of the roller is expected because of the corresponding drop in temperature. Since surface treatment is believed to be highly dependent on OH concentration, these results show the importance of accounting for the chilled roller influence on OH concentration.
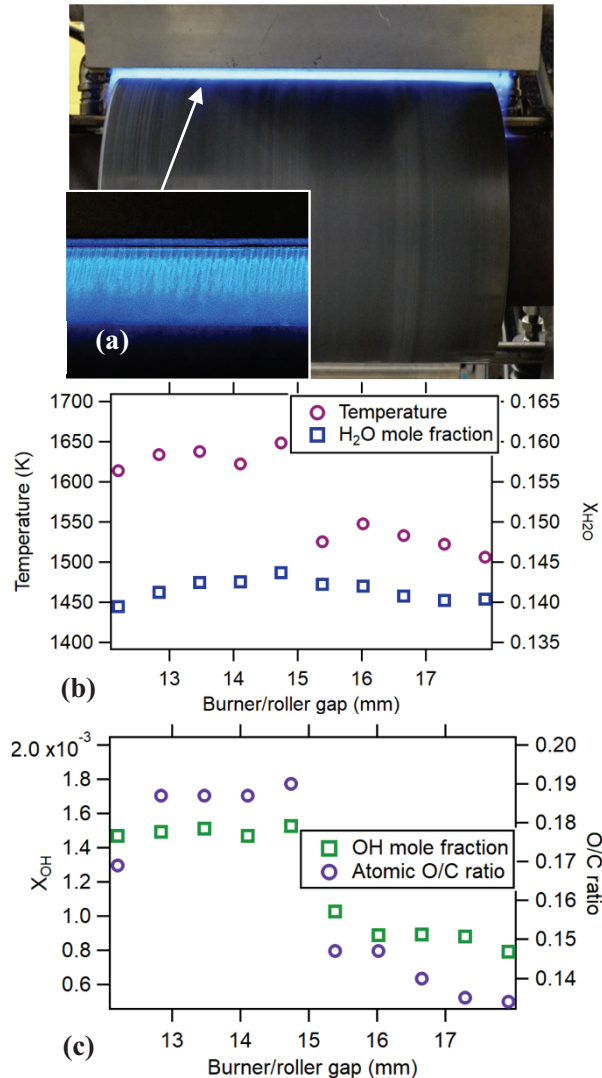
Fig. 3-4. (a) The industrial flame processing system with a ribbon burner firing down onto a chilled roller that passes polymer film below the flame. (b) Temperature (circles), H_2O mole fraction (squares) (c) OH mole fraction (squares) and O/C atomic ratio (circles) as a function of burner-to-roller gap at stoichiometric conditions with polypropylene film passing at 200 m/min.

3.5 The influence of OH mole fraction on polymer film surface modification

Because the previous section shows that the presence of the chilled roller has a cooling effect on the ribbon burner premixed flame, it is important to directly relate OH concentration measurements to surface activation of a PP film. We used a 3M industrial flame processing system built by Flynn Burner Corp., with the flame firing down onto 30-cm-wide polypropylene film that passes over a chilled roller. A photograph of the apparatus, which is different from the setup used in Sec. 3.3 and 3.4, is shown in Fig. 3-4(a); the inset magnifies the structure of the flames impinging on the 37˚C chilled roller. The laser sensor is mounted such that it measures 1-2 mm above the surface of the roller for all experiments. The burner operates at a power flux of 770 W/cm², which is another typical processing power, and the roller passes film over the ribbon burner at a speed of 200 m/min. The experiments were conducted near the stoichiometric ratio for an air:natural gas flame. The gap between the burner and roller was varied between

42

8.9 to 15 mm in order to vary the location of the film within the flame and to determine the location that achieves peak X_{OH} at the film surface. The films that passed under the impinging flame were characterized using XPS to measure the O/C atomic ratio, which is a measure of the extent of surface oxidation that, in turn, determines wettability and adhesion.

Fig. 3-4(b) and (c) present the temperature, X_{H2O}, and X_{OH} at the roller surface as a function of burner-to-roller gap at stoichiometric conditions, where each point is the average of one minute of data. Basic calculations show that the number of reactive sites that must be oxidized to achieve the measured O/C ratio is much less than the OH flux near the surface. Therefore, we do not expect the oxidation of the PP film to significantly affect the measured OH concentration field. One might expect the maximum X_{OH} to occur when the burner-to-roller gap matches the height of the peak OH mole fraction of the roller-obstructed case shown in Fig. 3-3(d), scaled by the 40% increase in power flux used for the PP film processing case (~9 mm peak for the roller-obstructed case, scaled to 12-13 mm for the PP film processing case). Because the power flux used to generate the data in Fig. 3-4(b) is 1.4 times larger than the power flux used for the data in Fig. 3-3(d), we expect the peak to be closer to 8-9 mm above the burner, instead of 6 mm as shown in Fig. 3-3(d). We find instead that the peak X_{OH} measured at the film surface occurs at a gap of 14 mm. This suggests that changing the gap between the chilled roller and the burner variably alters the structure of the flame (i.e. can cause variation in the OH peak location) in ways that are difficult to predict, further supporting the need for direct measurements of OH in the system.

The temperature and OH measurements shown in Fig. 3-4 have a discontinuity between the 11.7 and 12.3 mm gaps. This discontinuity was caused by stopping the process to change to a new roll of the same input PP film. The discontinuity is also present in the O/C atomic ratio (shown as circles), demonstrating the direct connection between the measured OH radical and the surface modification result.

There are many possible reasons for this unexpected discontinuity, including slight changes in the flame stoichiometry, and/or film-handling system between the experiments. As mentioned earlier, this dataset was collected near the stoichiometric condition of the natural gas mixture. The industrial-scale

43

control system for the natural gas-based flame treating system is based on feedback from an oxygen sensor on the inlet piping, which is challenging to use near stoichiometric conditions. For example, changes in humidity and natural gas composition often result in discprepancies in flame treating near the stoichiometric condition. It is therefore possible that while conducting this experiment, the data for the first polypropylene roll were collected under slighly fuel-rich conditions while the data for the second polypropylene roll were collected under slightly fuel-lean conditions. The change in flame condition from fuel-rich to fuel-lean has been shown to cause drastic differences in flame chemistry and the polypropylene surface chemistry by Strobel *et al.* [79]. Nonetheless, the resulting discontinuity presented an excellent test of the connection between OH radical concentraion and surface oxidatation that was suggested by previous numerical studies [1,68,73]. OH drops 32% and the O/C ratio drops 23% across the discontinuity. Although temperature also exhibits the discontinuity to a smaller degree (drop of 7.5%), previous work by Strobel *et al* studying the effect of flame conditions and flame-to-film gap suggests that the extent of surface treatment of polypropylene film does not correlate with temperature [34].

In order to maximize the amount of polymer film that is flame-processed, the ability to treat films at the highest possible speed is almost always desirable in industrial applications. Therefore, the goal is to maximize the O/C ratio at any given film speed by optimizing other process variables such as reactant flow rates and burner-to-film distance. Once the O/C ratio is optimized at any given speed, a target O/C ratio can be achieved by varying the film speed. The measurements show the potential value for the sensor to both determine the optimal process variables to maximize O/C ratio, and for real-time monitoring and control of X_{OH} in industrial systems, as slight process variations from seemingly similar conditions can yield variation in X_{OH} and surface modification outcomes away from the optimal values.

3.6   Effects of burner to film gap size

The two process variables in flame treatment of polymer films that are most amenable to optimization are the flame equivalence ratio and the distance of the polymer film from the burner exit. Therefore, it is valuable to understand how these two factors affect the OH mole fraction presence in the

flame, as the previous section demonstrates the connection between polypropylene surface oxidation and OH presence in the flame. This section seeks to study the connection between burner to film gap size and polypropylene film oxidation through two means: measuring OH mole fraction on the chilled roller surface as the gap is varied over a range of distances, and measurement of film properties as a function of burner to roller gap.

3.6.1   Effects of gap size on flame properties at roller surface

First, we sought to understand how the burner to chilled roller gap affects the properties of the flame impinging on a polymer film passing over the chilled roller. Slightly fuel lean (ϕ=0.98) and slightly fuel rich (ϕ=1.02) conditions were selected to verify that a switch from lean to rich would not cause the large disconnect in our measured flame properties shown in Fig. 3-4. Additionally, these two conditions provides a comparison between fuel-rich and fuel-lean regimes in film processing conditions.

As with previous studies, the beam passed three times just above the surface of polypropylene film and at each gap one minute of data was collected. This study utilizes the higher capacity, down-firing flame system described in 3.5. Since Fig. 3-3(d) suggests that the the maximum OH mole fraction is within the region of the flame that has many chemical reactions, we collected two trials for the fuel-lean case where the visible flame is impinging on the surface. Measured OH signal is processed using the HITEMP 2010 database, which has increased uncertainty as compared to the new high temeperature H_2O database developed in Sec. 2. However, the presented trends will still represent the variation in OH between different conditions.

The measured flame properties at the film surface for varying burner to roller gap are shown in Fig. 3-5 for both ϕ=1.02 (fuel-rich) and ϕ=0.98 (fuel-lean) conditions. For both conditions the temperature peaks, rolls back off and starts to level off or come back up again. A similar trend is observed in the H_2O mole fraction for each condition. We expect that as the gap expands the hot gases touching the film will be fully combusted products that will cool as the reaction region moves farther away. The OH mole fraction, on the other hand, appears to increase as the gap decreases until it plateaus near 8 or 9 mm distance between burner and roller. It is important to note that the OH mole fraction measurements shown here are analyzed

using H_2O absorption parameters from HITEMP 2010, thus will capture the trends but have a much larger uncertainty than the results shown previously in the section. The trends shown in Fig. 3-5 suggest that smaller gaps may provide better surface oxidation in flame processing.
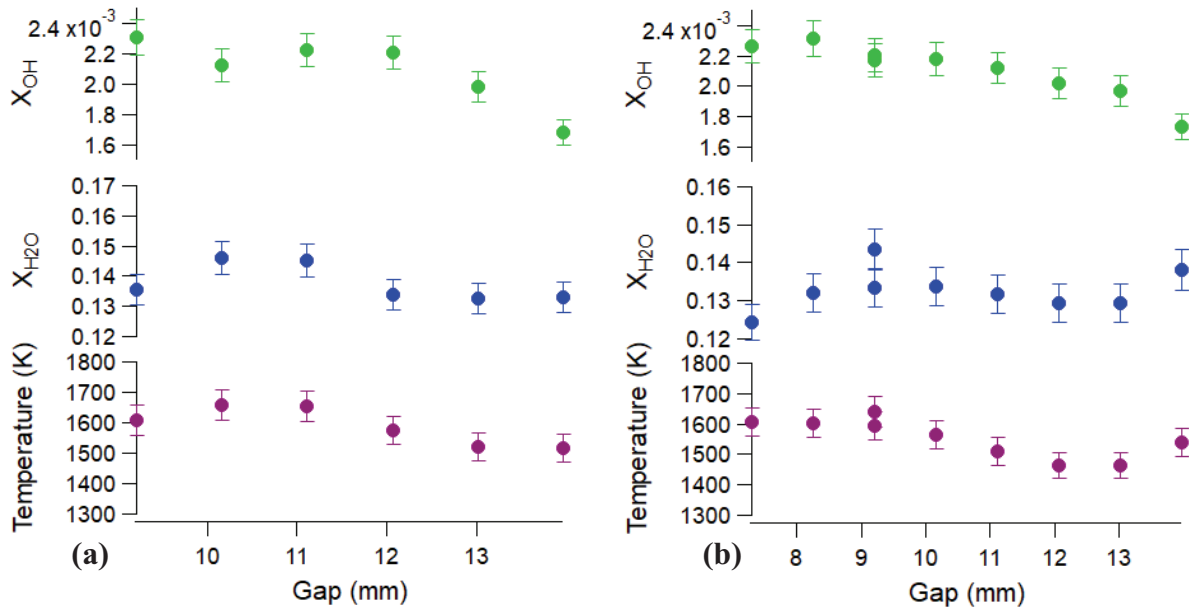
Fig. 3-5. Average temperature, H_2O and OH mole fraction measured at the surface of the chilled roller of the down-firing ribbon burner combusting at 770 W/cm^2 and (a) $\phi=0.98$ and (b) $\phi=1.02$ while the gap between burner and roller is varied. Uncertainty bars indicate sensor uncertainty discussed in Sec. 4.3 for H_2O and temperature and Sec 2.3.

3.6.2 Effect of burner to roller gap on film processing

OH mole fraction results in Fig. 3-5 demonstrate that decreasing the burner to roller gap size results in larger detected quantities of OH radical at the roller surface. However, these measurements do appear to reach a plateau, suggesting there may be a range of gaps that could be optimal for this processing. In order to verify this, we seek to understand the effect of the burner to chilled roller on the flame-processed film properties.

As with the performed in Sec. 3.5, we utilize a down-firing premixed flame burner operating at 770 W/cm^2 at an equivalence ratio of $\phi=0.98$. Polypropylene film passed through the flame at approximately 200 m/min for each sample. After the flame treatment, the O/C ratio is measured using XPS. The measured surface oxidation is shown in Fig. 3-6. The continued increase in O/C with decreased gap deviates from OH mole fraction trends as the OH mole fraction starts to plateau. This suggests that there may be other

46

variations in the flame structure as the gap is decreased, such as splaying of the flame cones to increase the amount of time polymer film is exposed to high OH concentrations.
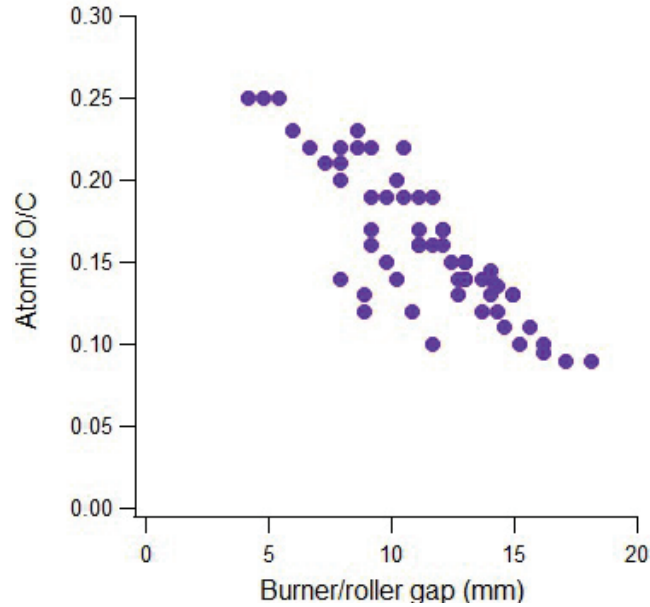
Fig. 3-6. O/C ratio of the surface of flame treated polypropylene film at various burner to roller gaps measured over two experiments.

3.7 Effect of equivalence ratio on flame and film properties

The other process variable that is typically available to optimize flame processing is the flame equivalence ratio. We measure the OH mole fraction in the flame impinging on the polymer film surface to understand the optimal equivalence ratio to maximize surface oxidation. It is challenging to study the effect of this variable polymer film processing because changes in the equivalence ratio affect the length of flame. Therefore, we vary the burner to roller gap as well as the equivalence ratio to find the gap with the maximum OH measurement for each equivalence ratio.

For this study, we utilize the down-firing set up shown in Fig. 3-4(a) so the flame properties can be probed as polypropylene film passes through the flame. The same conditions as previous trials are used: 770 W/cm^2, 200 m/min roller speed and a roller temperature of 308 K. The distance between the casing of the premixed burner and the chilled roller surface varies from 7.6-19 mm as the equivalence ratio

www.manaraa.com

is varied from 0.83 to 1.1. Flame properties are probed by passing the laser beam three times across the roller surface to maximize the measured signal.
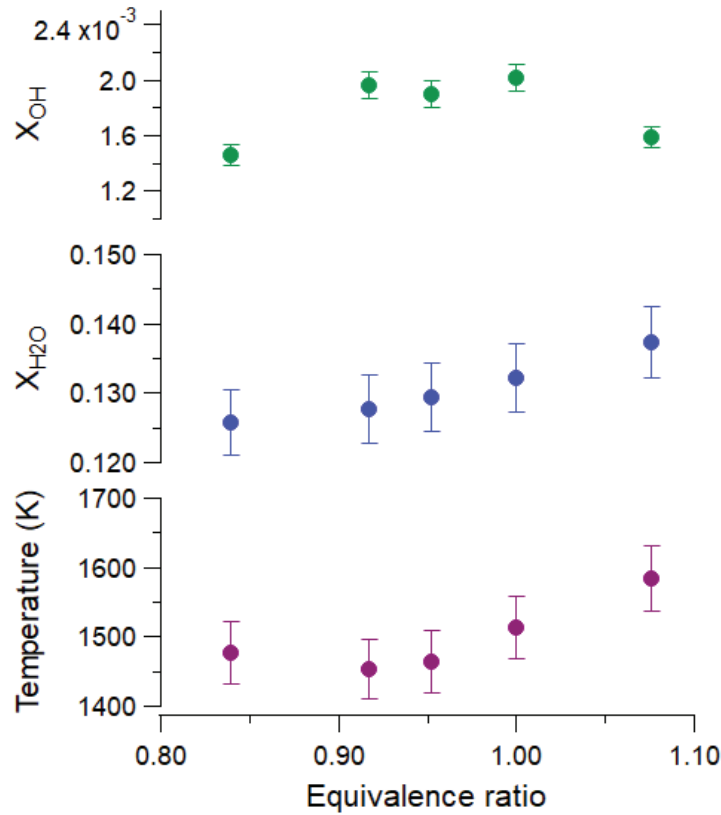
Fig. 3-7. Average temperature, H_2O and OH mole fraction measured at the surface of the chilled roller as equivalence ratio is varied as the ribbon burner combusts at 770 W/cm^2.

The measure flame properties at the surface of the processing polymer film at various equivalence ratios are shown in Fig. 3-5. The maximum OH mole fraction is for each equivalence ratio as the burner to gap is varied is shown here. From these measured flame properties at the roller surface it is clear that the OH mole fraction is maximized somewhere between an equivalence ratio of 0.92 to 1. This matches with previous experimental and numerical studies that predicted that the optimal equivalence ratio is near $\phi=0.93$-0.95 [79,88]. However, the variation between the measured OH mole fraction values for $\phi=0.92$-1.0 is within the uncertainty of the OH measurement, meaning no clear peak can be defined. Refinement of the OH measurement or increased interaction length is needed to determine

which equivalence ratio will maximize OH mole fraction. Yet, it is clear that the OH mole fraction, thus polypropylene film oxidation, can be maximized by varying the equivalence ratio.

3.8   Conclusions

We present the characterization of the vertical variation in the thermodynamic properties of a premixed ribbon burner used in industrial processing. First, we characterized the unobstructed flame, finding that measured temperature and X_{H2O} increased rapidly away from the burner, but then decreases slowly while X_{OH} peaked at approximately 4 mm above the burner. We then introduced a chilled roller above the flow, of the type that is used in the proccessing of polypropylene films. It is clear from our measurements that the introduction of the chilled roller above the premixed flame cools the flame and elevates the location of the peak X_{OH}. Previous works suggest a cooling effect of the roller, but it had not been previously known that X_{OH} peaks at a different location in the flame. This change in maximum X_{OH} location confirms that burner-to-roller gap has a large effect on the processing of polyolefin films [9].

Our third experiment measured the gas-phase properties as polypropylene film passed through the flame. This experiment showed identical trends in the X_{OH} of the flame impinging on the surface and the O/C atomic ratio of the processed film, confirming OH mole fraction is a driving factor in surface oxidation. We then study the effect of two process variables on OH mole fraction variation vertically in the flame and on the surface of polymer film. Varying the burner to chilled roller gap sizes suggests that smaller gap sizes result in increased oxidation of the polymer. Peak OH mole fraction values are found in the range of flame equivalence ratios of ϕ=0.92-1.0, but require further study before a singular peak value can be determined.

Having shown in this work that there is a direct connection between OH mole fraction in the impinging flame and surface oxidation of polypropylene film, it is clear that further measurement and optimization of X_{OH} is possible. We plan to develop a control scheme based on the X_{OH} measurements to show the potential for active control of the flame-treating process and its process variables to optimize the flame system for maximum OH mole fraction and surface oxidation.

3.9 Acknowledgements

The majority of the text for this chapter is published in the *Proceedings of the Combustion Institute* as:

4 Characterization of a buoyant jet from a catalytic combustor using wavelength modulation spectroscopy

4.1 Introduction

Catalytic combustion is used extensively in a variety of fields, from power production, to propulsion, to industrial baking [5,91]. It is a form of combustion in which the fuel and oxidizer react in a catalytic bed, which aids in the dissociation of O_2 and the breaking of C-H bonds, resulting in combustion at lower temperatures and with reduced pollutant emissions [5,6].

Another possible application of catalytic combustion is the heat treatment of materials. Heat treating of a material typically requires high spatial and temporal uniformity within and between product batches [1,76]. Reliable application of these treatments therefore requires an understanding of temporal and spatial non-uniformities present in the combustion gases that impinge on a material. However, despite extensive prior work on the characterization of catalytic combustion from chemical and materials perspectives, relatively little research has focused on the thermodynamic properties of the gases emitted from a catalytic combustor. This work seeks to address this disparity by characterizing the temporal and spatial uniformity of temperature and species mole fraction in the heated buoyant jet created by a catalytic combustor.

Previous work characterizing catalytic combustion has primarily focused on the surface chemistry of the catalyst. Chemists and material scientists have worked extensively to optimize the catalytic material to promote complete combustion (e.g. [92–95] and references therein). Work by Euzen *et al.* studied the causes of palladium catalyst deactivation in methane-air combustion [96], and Barbato *et al.* studied the temperature and conversion rate of mixtures of CH_4, H_2, and CO in a catalytic monolith at pressures up to 10 bar [97]. Deutschmann *et al* performed numerical and experimental studies of the product gases of hydrogen-assisted methane combustion in a palladium reactor [98]. All of these previous studies were aimed at understanding catalytic combustion primarily for power production applications.

Although there have been no characterizations of the plume above a catalytic combustor, jets and plumes in other combustion systems have been previously studied using a variety of intrusive and non-

intrusive techniques. For example, thermocouples, mass spectrometry, and pressure transducers have all been used to characterize combustion systems [1,99]; however, these measurement devices are intrusive and may require correction factors for high-temperature flows. Chemiluminescence has been used to measure radical species in combustion settings [100–102], but is difficult to perform quantitatively and provides information only on certain radical species. Other imaging techniques such as Schlieren can provide valuable information about the flow structure in combustion [103,104], but cannot provide the necessary quantitative data. Several groups have used particle image velocimetry and laser Doppler velocimetry to capture the characteristics of the flow field of a buoyant jet [103,105–107], but the presence of a catalyst here does not permit particle seeding. To determine spatial and temporal uniformity above a catalytic combustor, we require a non-intrusive, time-resolved, absolute sensor that can measure temperature and species concentrations at different locations. For industrial processes, it is also beneficial if the sensor is compatible with practical deployment so that it can be incorporated into process control systems.

Laser absorption spectroscopy is an excellent option to achieve these objectives in a heated, buoyant jet because it is quantitative, species-selective, robust and portable, and can provide millisecond time resolution [108]. Other laser-based techniques, such as laser induced fluorescence (LIF) and Raman or Rayleigh scattering, can provide the desired quantitative spatial and temporal information [39,99]; however, they can require large optical experimental systems that are impractical for industrial applications. The present study utilizes scanned-WMS, as described in Sec. 1.2.3, because it offers improved sensitivity and resistance to beam perturbations, which are prevalent in combustion measurements. Many groups have used WMS to sense temperature and species mole fraction in a variety of combustion environments, from atmospheric flames to shock tubes [24–32]. but this technique has yet to be applied in the context of catalytic combustion.

Here we utilize WMS to characterize the temporal and spatial variability of temperature and water vapor mole fraction in a high-temperature heated buoyant jet created by a 7.5 cm x 25 cm rectangular iron-chromium alloy catalytic combustor. The sensor is first validated in a controlled system with known

52

conditions. Then, we employ the sensor to obtain time-resolved measurements of temperature and water vapor mole fraction at different vertical and horizontal locations above the combustor. A novel approach to pathlength correction based on computational fluid dynamics (CFD) simulations is demonstrated to improve the mole fraction characterization within the buoyant jet. The measurement of these parameters improves the understanding of the non-uniformities and variations in the jet.

4.2   Measurement Approach

4.2.1   Temperature measurement using scanned WMS

We calculate temperature with two-line thermometry by using the integrated absorbance extracted from the WMS fit to two H_2O transitions [19]. Scanned WMS and the extraction of integrated absorbance are described in detail in Sec. 1.2.

This study utilizes two NEL Inc. distributed feedback (DFB) diode lasers centered on H_2O absorption transitions at 1391.7 nm and 1468.9 nm. The features were chosen because of the large difference in the lower-state energy of these transitions (1045 cm^{-1} and 3319 cm^{-1} , respectively), which optimizes the temperature sensitivity at elevated temperatures, and the existence of previously validated linestrength parameters [20].

4.2.2 H_2O mole fraction measurement through pathlength correction approach

For a given temperature, we calculate the H_2O mole fraction by solving Eq. (1-4) for X_{abs} using the integrated absorbance of one transition. Pressure is measured using a calibrated capacitance manometer at the time of experiments. The linestrength, $S(T)$, is calculated using measured parameters from [20]. We quantify the background H_2O absorption in the room air by measuring the signal with only dry air flowing through the combustor. We then subtract the integrated area measured with dry air only from subsequent measurements with the combustor on.
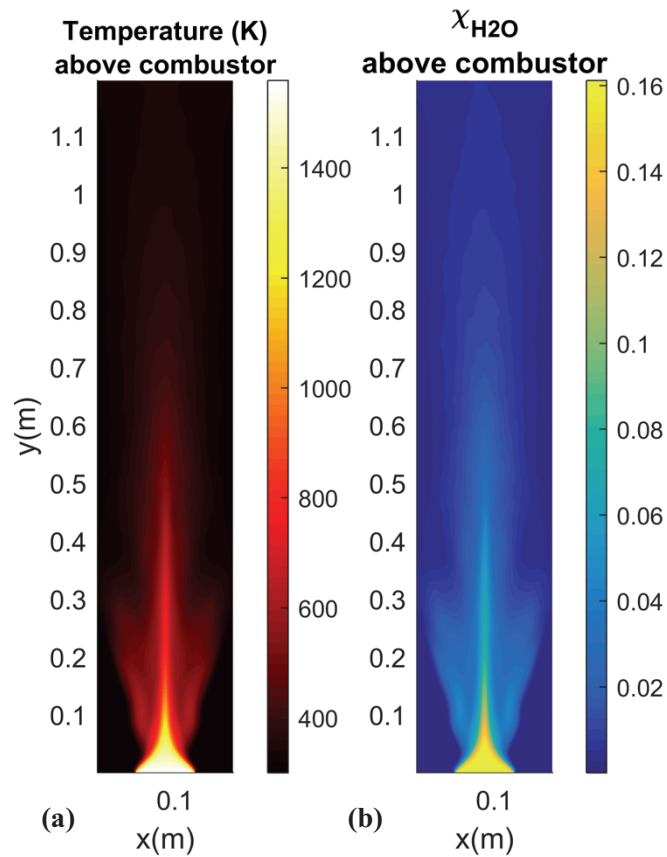
Fig. 4-1. CFD simulation of the time-averaged (a) temperature and (b) H_2O mole fraction above the combustor

The species mole fraction that is extracted in absorption spectroscopy is the mole fraction along the laser beam path. However, when examining a non-reacting jet above a catalytic combustor, the primary quantity of interest is the average H_2O mole fraction within the jet, and not the average of H_2O mole fraction in both the jet and the surrounding ambient air. Within the buoyant jet, the expected H_2O mole fraction values are on the order of 15-19%, because the jet is primarily composed of combustion products, while the water mole fraction of the ambient air is typically below 1%. Using the pathlength between the transmit and receive optics for the H_2O mole fraction calculation gives the average concentration of both the jet and the surroundings. Because the path includes a significant length of ambient air and because the buoyant jet narrows and billows at different points in the flow above the combustor (see Fig. 4-1), the mole fraction calculated using the pathlength between the transmit and receive optics is therefore difficult to interpret.

54

We present here a novel approach that uses CFD simulations to calculate the effective jet width for use in the calculation of the mole fraction within the jet. We simulate a non-reacting heated, buoyant jet with a rectangular exit matching the size of the catalytic burner using the open-source finite-volume code, OpenFOAM [109,110]. Inlet conditions are fixed at the temperature measured at the combustor surface, and the velocity was estimated from the combustor power flux. We assume complete combustion for equivalence ratio of 0.85 and thus fixed mass fractions of N_2, O_2, H_2O and CO_2 accordingly.

The low-pass filtered compressible Navier-Stokes equations were solved with second-order accuracy in conjunction with mass, enthalpy, and species conservation equations using fireFoam [111]. A dynamic one-equation eddy sub-grid scale model closes the resulting large eddy simulations (LES) [112]. Heat transfer modes include conduction, advection, and radiative losses approximated with the discrete ordinate method.

The computational domain contains approximately 2.4 million control volumes stretched vertically to enhance resolution near the burner, resulting in a maximum vertical resolution of approximately 0.4 mm. The grid is uniform in horizontal directions. Time stepping was adaptive and controlled by a maximum CFL condition set to 0.4. After enough computational time has passed to allow to allow the flow field to become statistically stationary, we computed statistics for temperature and water vapor mass fraction over a duration of 10 s. Example fields from the simulations are shown in Fig. 4-1.

The distributions of time-averaged H_2O mole fraction are extracted from the CFD solution, χ_{sim}, at the laser measurement locations above the combustor. The profiles are then normalized by the maximum value at each height, as shown in Fig. 4-2(a), and integrated across the line-of-sight beam path to calculate an effective pathlength or width of the jet, as per Eq. (4-1):

$$L_{eff,jet} = \frac{1}{\chi_{max,sim}} \int_0^L \chi_{sim} \, dx \qquad (4\text{-}1)$$

here $L_{eff,jet}$ is the weighted pathlength or jet width, L is the entire length across the CFD simulation, and x is the position along the laser beam.
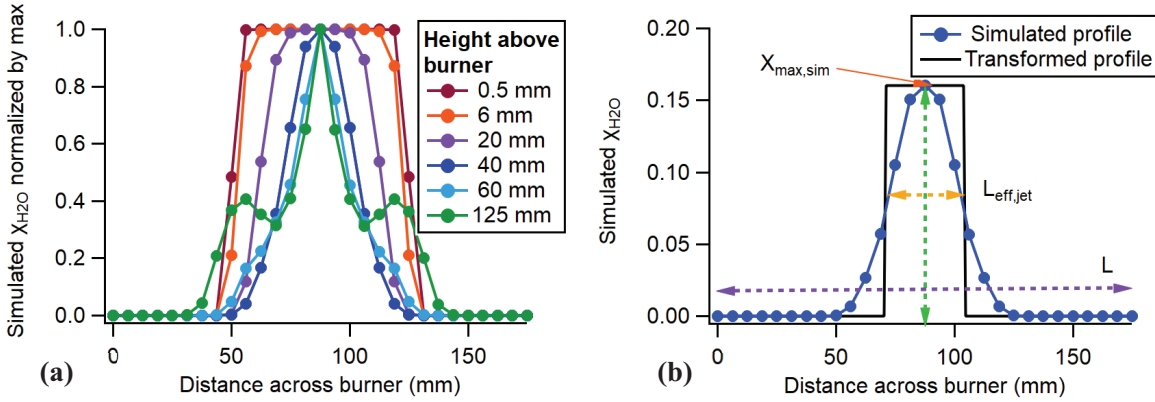
Fig. 4-2 (a). Extracted H_2O mole fraction profiles across the width of the catalytic combustor from the CFD simulation of the heated, buoyant jet above the catalytic surface. (b) Simulated H_2O mole fraction profile as a function of distance across the burner at 18 mm above the surface and the corresponding top-hat profile with the same area, and a height of $\chi_{max,sim}$ and a width of $L_{eff,jet}$ calculated using Eq. (4).

As shown in Fig. 4-2(b), this approach is essentially a transformation of the simulated mole fraction profile, χ_{sim}, to a top-hat profile via conservation of area under both profiles. Because absorption spectroscopy retrieves a single value for each beam path, the top-hat profiles represent the laser measurement outcomes. Examples of the effective jet widths weighted by the water mole fraction distribution from the traces in Fig. 4-2(a) are shown in Fig. 4-3.
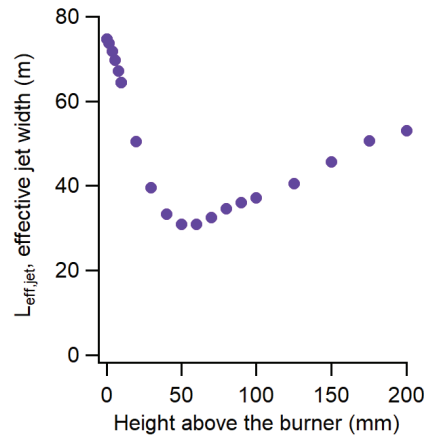
Fig. 4-3. Effective jet width used for the estimation of mole fractions within the jet at different heights above the combustor using Eq. (4-1).

Having calculated an estimated jet width at any given height above the combustor surface, a corrected jet concentration measurement can then be calculated from measured values using Eq. (4-2):

56

$$\chi_{corr} = \frac{L}{L_{eff,jet}} \chi_{avg} \tag{4-2}$$

where χ_{corr} is the adjusted mole fraction measurement, L is the length across the CFD domain and corresponds to the distance between transmit and receive optics, $L_{eff,jet}$ is the effective width of the buoyant jet at a given height above the combustor surface, and χ_{avg} is the WMS-measured mole fraction.

4.3   Sensor validation

The goal of the sensor validation is to quantify the sensor uncertainty using known measurement conditions; in this case, five different temperatures with a fixed H_2O mole fraction in air.

4.3.1   Experimental setup
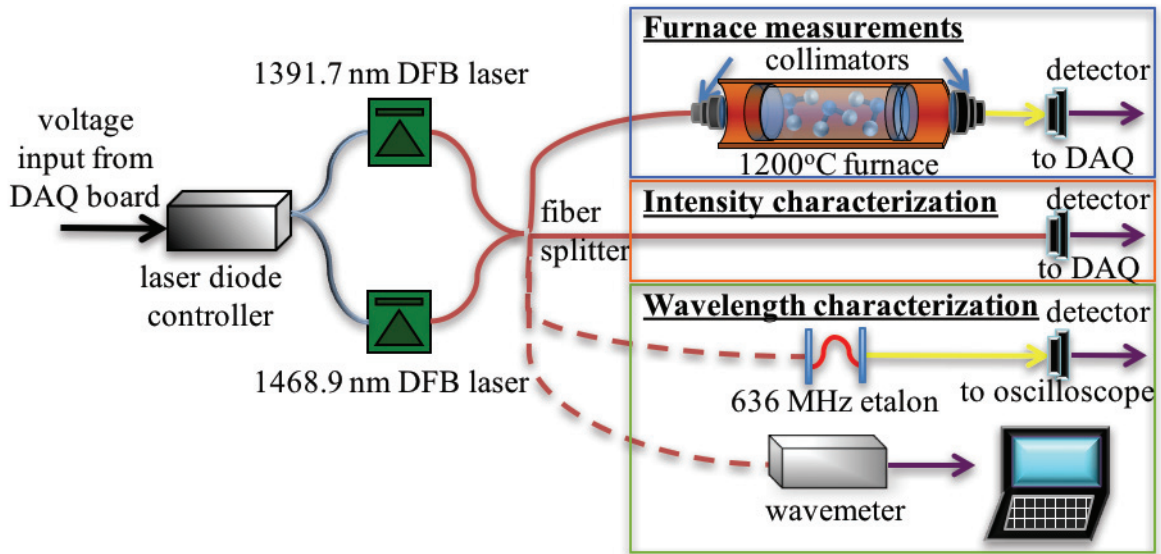
Fig. 4-4. Schematic of experimental setup used for sensor validation.

A schematic of the experimental setup is shown in Fig. 4-4. The sensor contains two NEL DFB lasers centered at 1391.7 nm and 1468.9 nm. The sensor contains two NEL DFB lasers centered at 1391.7 nm and 1468.9 nm. An ILX Laser Diode Controller (LDC) sets the center wavelength of each laser by adjusting current and temperature of each laser individually. Using external voltage inputs, the LDC also modulates the intensity and wavelength. A National Instruments PCI 6110 data-acquisition board connected to a National Instruments 2110 connector box generates voltage waveforms that are applied to the LDC. Each laser drive signal is composed of a sine wave at 500 Hz to tune the wavelength over the absorption feature, as well as a fast sine wave for WMS at 130 kHz for the 1392 nm laser and at 170 kHz for the 1469

57

nm laser. Light from the two lasers is multiplexed onto a single fiber using a 50/50 fiber coupler so that the two lasers simultaneously pass through the gas sample along the same path.

During validation measurements, half of the combined light passes through a quartz cell in a tube furnace containing a controlled mixture of H_2O and air. The light is attenuated by the water vapor to produce I_t in Eq. (1-3). This intensity is measured by a Thorlabs PDA10CS photodetector and digitized at the DAQ board. Signals from the two lasers are separated by de-multiplexing the signal using a digital lock-in amplifier at the *2f* and *1f* frequencies for each laser.

In order to build the model described in Sec. 1.2 and extract thermodynamic properties from the data, the laser tuning properties must be characterized. The un-attenuated intensity variation of the light (I_0) is measured by passing light for each laser individually directly to the detector. Light is also passed through a 636 MHz fiber Fabry-Perot etalon prior to the experiment to characterize the amplitude of the wavelength variation. The wavelength as a function of time is calculated from the temporal location of etalon resonances. The light passes to a Thorlabs Fourier transform optical spectrum analyzer with wavemeter capabilities to determine the average absolute laser wavelength (with the modulation turned off).

4.3.2   Sensor Validation Results

The WMS sensor was validated using a mixture of H_2O in dry air at five different temperatures from 900-1273 K. For the H_2O mole fraction validation, we prepare a test mixture by introducing 0.01667 atm (12.66 Torr) of water vapor to a mixing tank, followed by 1.040 atm (790.3 Torr) of dry air taken from a gas cylinder with less than 2 ppm H_2O content. Though the mixture should be 1.6% H_2O in air based on the partial pressures of the gases, water is polar and adsorbs to the surfaces of the mixing tank and gas handling system. A constant H_2O mole fraction that is slightly less than 1.6% was thus expected, since all measurements were made on the same mixture. Between each trial the temperature of the furnace stabilized for several hours. Results for the sensor validation experiment are shown in Fig. 4-5.
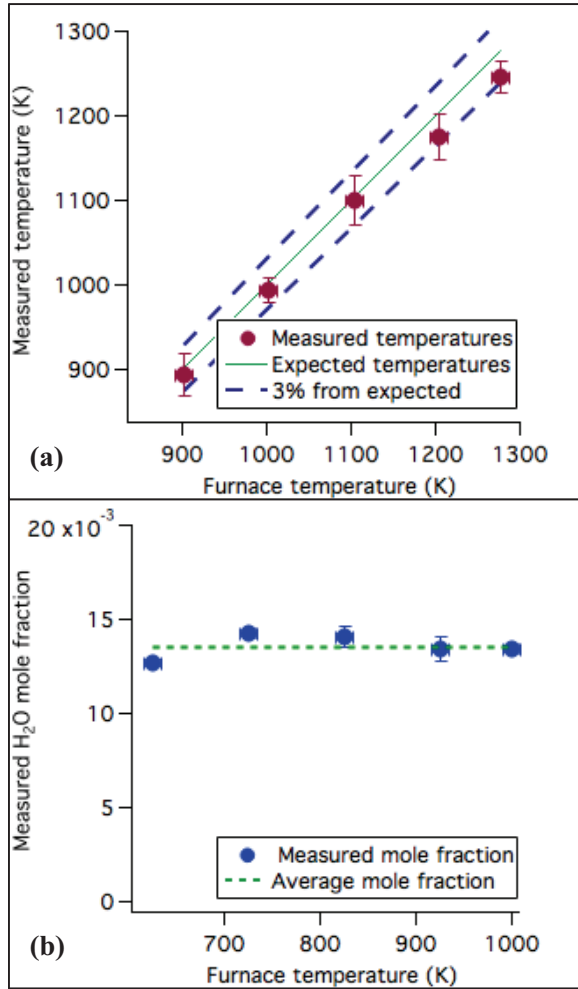
Fig. 4-5 Sensor validation results. (a) Temperature measured using WMS relative to the thermocouple-measured furnace temperature. Vertical uncertainty bars are the standard deviation of each measurement while horizontal uncertainty is the measured uncertainty of the thermocouple. (b) Measured H_2O mole fraction as a function of furnace temperature. Horizontal uncertainty bars measured uncertainty of the furnace temperature while the vertical uncertainty bars indicate the mole fraction uncertainty. The dotted line indicates the average measured value of 0.0136.

As shown in Fig. 4-5(a), the WMS temperature tracks the furnace thermocouple temperature. The WMS values lie within 3% of the furnace temperature (establishing a ~3% systematic uncertainty for the sensor in this temperature range). The vertical uncertainty bars on the measurement represent the standard deviation in time for each measurement. The horizontal uncertainty bars correspond to the uncertainty of the thermocouple-measured furnace temperature. Because the fixed temperature furnace only extended to approximately

The results shown in Fig. 4-5(b) have a mean value near 1.36% H_2O, with +/- 6.3% variation across the temperature trials. We take this variation to be the systematic uncertainty of the H_2O mole fraction measurement, although the actual systematic uncertainty might be slightly higher because the actual H_2O mole fraction of the mixture is not known precisely.
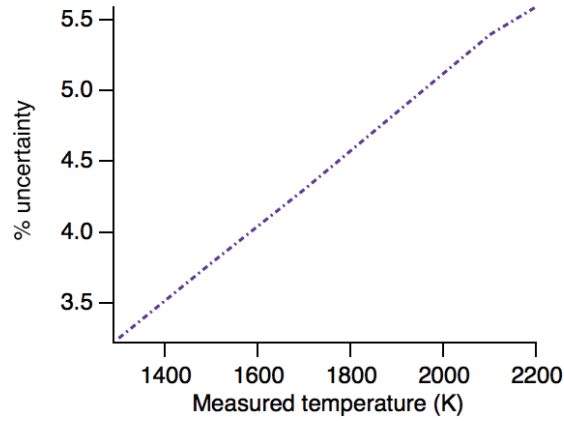
Fig. 4-7. Extrapolated % temperature uncertainty from measurements made in fixed temperature furnace.

Because of the non-linear relationship between linestrength ratio and temperature described in Sec. 1.2.2, the 3% measured temperature uncertainty is not going to hold at high temperatures. Therefore, we calculate what this uncertainty in temperature equals in ratio uncertainty. We then apply the same ratio uncertainty to the linestrength ratios that result in temperatures from 1300-2200K. The resulting range of ratios is then used to calculate a new range of temperatures, which can be converted into a percentage uncertainty. The extrapolated percent uncertainty in measured temperature from 1300-2200K is shown in Fig. 4-7.
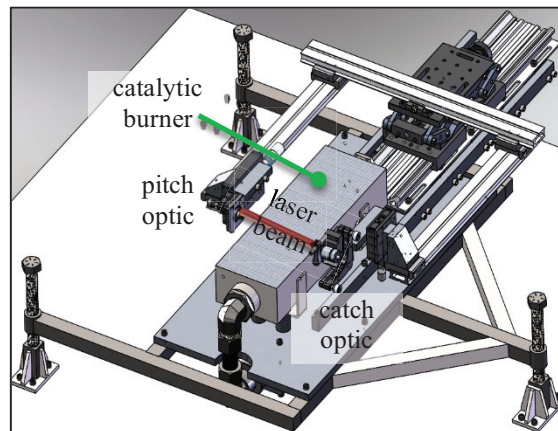
Fig. 4-6. Rendering of the experimental setup for the combustor characterization. The optics are oriented to pass light between the pitch optic and the catch optic across the short dimension of the burner.

60

4.4   Characterization of heated, buoyant jet above a catalytic combustor

Having validated the sensor at known conditions, we used the sensor to probe the temperature and H_2O mole fraction distributions in the heated buoyant jet above a catalytic combustor. These distributions characterize the temporal and spatial uniformity in the jet, and provide insights into the suitability of the catalytic combustor for materials processing.

4.4.1   Experimental setup

The optical configuration for the combustor characterization is the same as in Fig. 4-4, except the furnace is replaced with the combustor shown in Fig. 4-6. The catalytic combustor has an active area of 7.5 cm by 25 cm, with an iron-chromium alloy catalyst bed welded to an open-box metal frame. A mixer is mounted to the bottom of the stage, and consists of a bed of glass spheres that the combustible mixture passes through before reaching the burner. As shown in Fig. 4-6, the light is sent across the short dimension of the combustor (which we will call the width throughout the remainder of the paper). The y-shaped optical stage is mounted on a scissors jack that enables vertical translation of the laser beam in the buoyant jet. The jack is mounted on a track that allows horizontal scanning of the beam in the jet.

4.4.2   Time-resolved measurements

The catalytic combustor operates on a mixture of methane and desiccant-dried air at an equivalence ratio of $\phi = 0.85$ to produce a power flux of 24 W/cm^2. The selected conditions are typical of the baking industry and fall within the operating range of the catalytic combustor. Alicat mass flow controllers regulate the flow rates of air and methane. We collect one minute of WMS data at 500 Hz to characterize the temporal variation of the burner.

Fig. 4-8(a) shows time-resolved measurements of temperature and mole fraction across the width of the combustor as the laser beam skims the catalyst surface. The light color markers indicate measurements at the 500 Hz measurement frequency of the sensor (set by the scan rate across the absorption features). The average temperature is 1522 K and the standard deviation is 30 K (with a range of 240 K), while the average H_2O mole fraction is 0.13 with a standard deviation of 0.006 (with a range of 0.05).

61
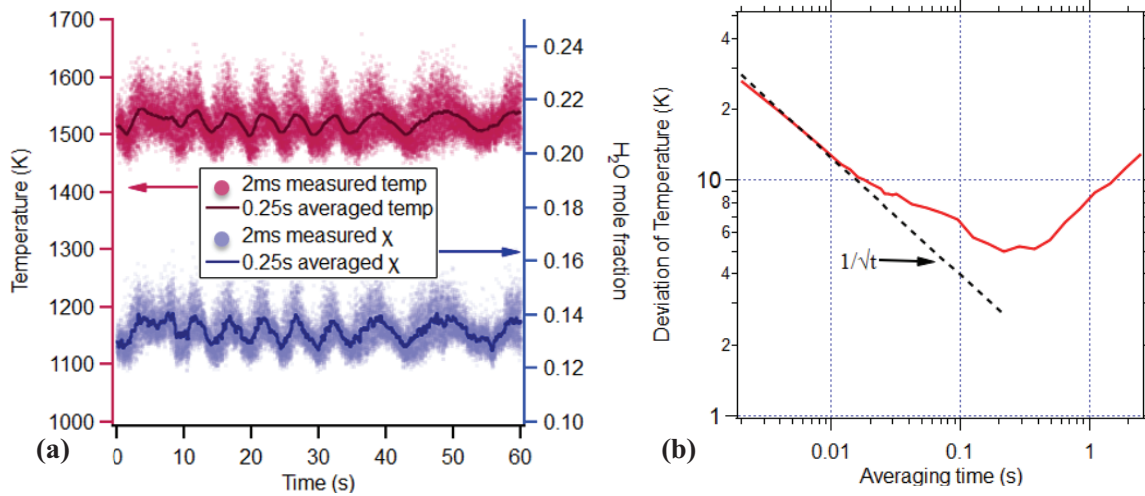
Fig. 4-8. (a) Temperature and water mole fraction as a function of time measured using WMS in the middle of the combustor, skimming the surface. Light colors show measured values at 500 Hz with darker traces represent the 0.25s running average. (b) Allan deviation of temperature measurement shown in (a). Plot shows standard deviation of the data as a function of the averaging time step.

The Allan deviation of the temperature measurement is shown in Fig. 4-8(b). The Allan deviation exhibits an initial slope of $1/\sqrt{t}$ that is consistent with white noise dominating the system precision over small time scales. This can most likely be attributed to sensor noise. Beyond approximately 200 ms (5 Hz), the Allan deviation flattens and then starts to increase, which indicates that the precision at longer time scales is limited by random-walk behavior in the system. The slow variations are present in all levels of the jet. We believe these variations can be attributed to buoyancy effects in the jet or combustor drift, e.g. due to oscillation in the flow controller [7]. By averaging to 0.25 s intervals (which represents the minimum in the Allan deviation and approximately the time at which we believe combustor variation dominates over sensor noise), the variation range over 60 seconds is 50 K for temperature and 0.015 for H_2O mole fraction.

4.4.3 Vertical scan

Vertical variations in temperature and H_2O mole fraction provide information on whether the combustion is complete or whether additional reactions may be occurring above the catalyst. Understanding these vertical variations in the buoyant jet can also provide insights on whether the combustion is complete or whether additional reactions may be occurring above the catalyst. In addition, understanding the vertical profile can help determine where heat-treated products should be placed for

exposure to a particular temperature. We collected vertical profile data on three different days at the same conditions as the experiment in Section 4.4.2 (24 W/cm^2 and $\phi = 0.85$). The lowest measurement occurs at a height where half of the 0.9 mm beam is cut off by the surface of the burner, and then measurements occur at different intervals up to 200 mm above the burner surface. For all trials, the sensor probes the center of the burner across the width. Data are collected for at least one minute at each height.
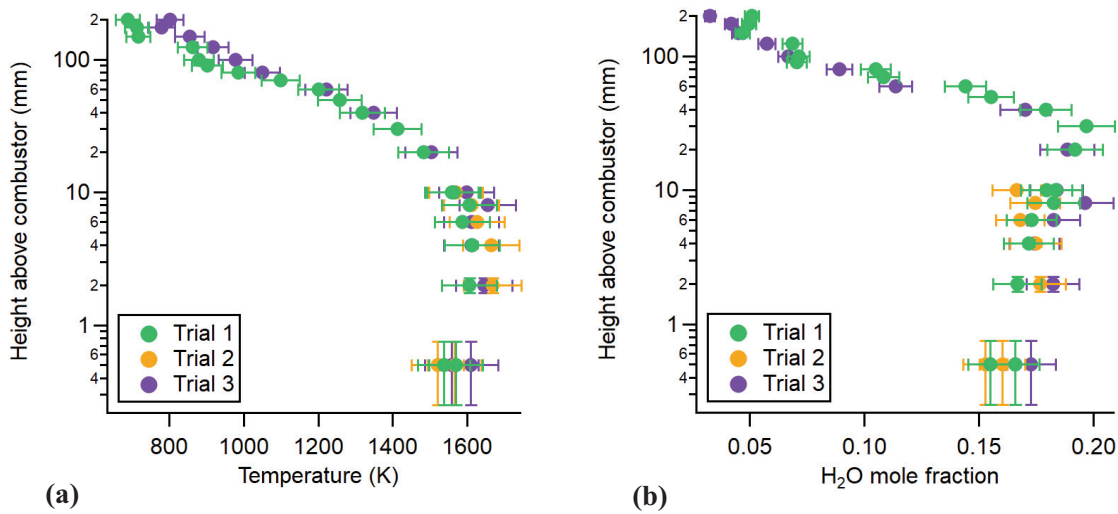
Fig. 4-9. (a) Temperature as a function of height above the burner over four trials. $\phi=0.85$ and power flux = 24 W/cm^2. Vertical uncertainty is the uncertainty of the height measurement and the horizontal uncertainty is the approximately 3% systematic uncertainty of the sensor determined from the validation. (b) Pathlength-corrected H_2O mole fraction at different heights in heated buoyant jet above the catalytic burner, at the same conditions as (a). Vertical uncertainty bars are the uncertainty of the beam diameter and the horizontal is the 6% sensor uncertainty derived from the validation presented in the previous section.

The measured temperature profiles for all three trials are shown in Fig. 4-9(a). The horizontal uncertainty bars are the 3% uncertainty in the temperature measurement derived from the sensor validation in Sec. 4.3. Vertical uncertainty is due to the beam width of 0.9 mm, which was measured with a razor blade translated through the beam on calipers. Measurements within the first 10 mm of the combustor surface show that there is a slight increase in temperature in immediately after the gases exit the combustor. This suggests that the entrainment of dry, cool air is not dominant in this near-field region. Instead, this observation suggests that additional reactions may occur above the catalyst bed, counteracting the expected decrease in temperature due to mixing effect with the room air. The decrease after 10-20 mm suggests that

entrainment of ambient air begins to dominate at larger heights. Comparing the temperature profile between all three trials establishes the level of system stability and measurement error to approximately 18%.
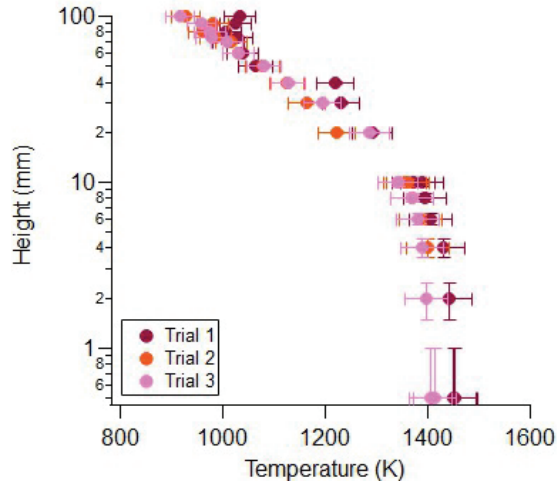
Fig. 4-10. Temperature as a function of height above the burner over four trials. ϕ=0.8 and power flux = 14 W/cm^2. Vertical uncertainty is the uncertainty of the height measurement and the horizontal uncertainty is the 3% systematic uncertainty of the sensor determined from the validation.

Fig. 4-9(b) shows the water mole fraction results as the sensor is scanned vertically above the combustor. All three trials utilize the pathlength correction described earlier in Sec. 4.2.2. The horizontal uncertainty bars are the uncertainty associated with the H$_2$O mole fraction measurement derived from the furnace measurement. If the catalytic combustor were to completely combust all of the reacting gases, one would expect the H$_2$O mole fraction maximum to occur at the surface. Hence, the local maximum of H$_2$O mole fraction at roughly 20-30 mm once again suggests the presence of continued reactions for the first 20-30 mm.

After 40 mm, the mole fractions begin to drastically decrease, as would be expected with the mixing and entrainment of ambient air.

As we show in Fig. 2-8, there is OH present above the surface of the catalytic combustor at the conditions in Fig. 4-9. Therefore, we want to test what effect the presence of OH and additional combustion reactions has on the rest of the flow field by probing a condition where there is no detectable OH present. Data is collected at the same heights as the previous sets shown in Fig. 4-9 on three different days. The laser beam passes three times through the buoyant jet in order to maximize the measured signal. As with previous measurements, the background H$_2$O absorption is quantified before and then subtracted for temperature analysis.

Fig. 4-10 shows the measured vertical temperature profile at $\phi=0.8$ and power flux = 14 W/cm^2. All three trials demonstrate a decrease in temperature above the first millimeter probed above the surface. This suggests that there is not additional heat release in this case (which would serve to increase or maintain temperatures). Instead, the decrease in temperatures matches well with entrainment and mixing of ambient air into the buoyant jet.
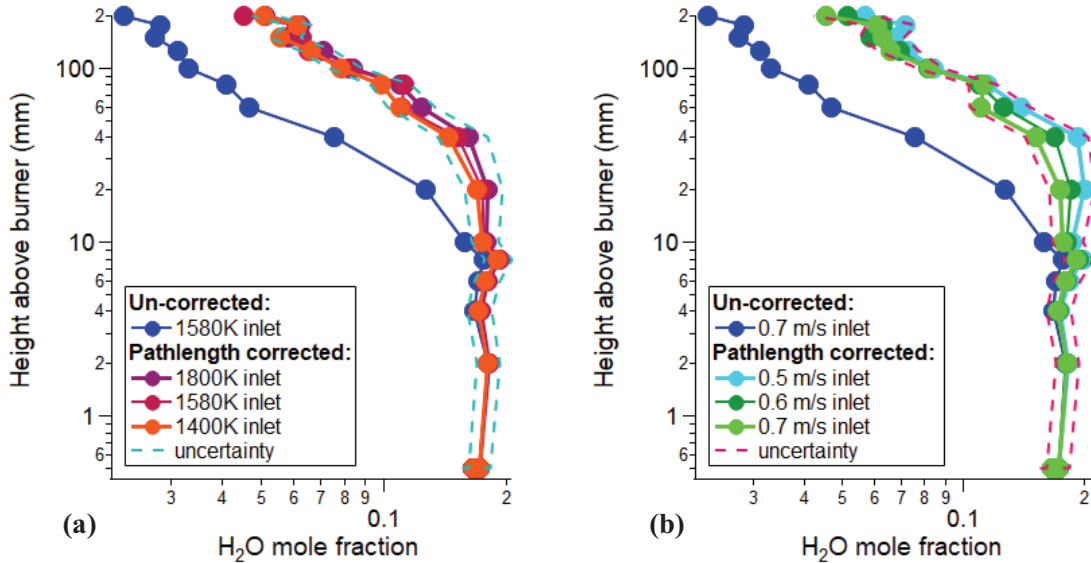
Fig. 4-11. (a)Pathlength-corrected and uncorrected H$_2$O mole fraction vertical profile using CFD simulations with four different initial temperature conditions. (b) Pathlength- corrected H$_2$O mole fraction vertical profiles using CFD simulations of different inlet velocities.

To verify that the conclusions presented herein are not affected by uncertainty in the pathlength correction approach, we test the sensitivity of the results to variations in the CFD boundary conditions. Specifically, it is necessary to understand how varying the temperature and inlet velocity boundary conditions of the CFD simulations affects the pathlength-corrected values [panels (a) and (b) of Fig. 4-11, respectively], because the measured temperature and H$_2$O mole fraction values inform the boundary conditions for the CFD simulations that in turn inform the mole fraction measurements. Since the experimental uncertainty for temperature measurements is estimated to be 3% and the measured value at the exit of the catalyst is 1580 K, the range of uncertainty is approximately 1530-1630 K. We chose values of 1400 K and 1800 K for the sensitivity study to represent extreme cases. Despite the 400 K variation in the simulation inlet temperature, the pathlength-corrected profiles vary only within the systematic

uncertainty of the original mole fraction measurement (i.e. there is little influence of errors in the CFD inlet temperature on the pathlength-corrected measurement results). The variation of inlet velocity (Fig. 4-11(b)) results in more variation in the pathlength-corrected profile. However, the variation is still minimal and within the mole fraction uncertainty, and is also small compared to the difference between the corrected and uncorrected data. The dashed lines in both (a) and (b) show the uncertainty range on the pathlength correction approach by assuming 3% temperature uncertainty, 5% effective pathlength uncertainty, and a standard deviation of about 8% in the measured absorbance areas. Both figures suggest that the pathlength-corrected results are robust with respect to uncertainties in the CFD simulation boundary conditions.

4.5   2D scan of temperature and mole fraction

The final un-impinging catalytic combustor experiment is a 2D scan of the buoyant jet above the catalytic combustor. The goal is to provide further insight into the spatial non-uniformity of the flow for comparison to CFD simulations. The experiment consists of a horizontal scan across the long dimension of the burner (hereafter termed the 'length') in 30 mm intervals at four heights above the surface of the catalyst: 1.5 mm, 11.5 mm, 26.5 mm, and 41.5 mm.

The results of the 2D temperature scan are shown in Fig. 4-12(a) and (b). Each data point [denoted by the open circles in in Fig. 4-12(a) and (c)] consists of at least a 30 s average to account for the slow variations present in the burner. The data are linearly interpolated to generate the 2D fields shown in panels (a) and (c). The temperature map of the data suggests that there is a non-uniformity of approximately 100 K across the surface. Fig. 4-12(b) shows the vertical profiles taken at $z = 60$ mm and $z = 180$ mm. When fit with a linear trend line, both profiles show similar linear trends to the temperature profiles above 10 mm in Fig. 4-9(a), with a slope of about 9 K/mm. However, this 2D scan does not have the vertical resolution necessary to resolve the stable temperature up to 10 mm as shown in Fig. 4-9(a). Because there is ~100 K variation horizontally across Fig. 4-12(a), while there is a constant-slope decrease in temperature in Fig. 4-12(b), it is likely that there are non-uniformities in the catalytic mesh of the combustor.

Similar results for the H_2O mole fraction are presented in Fig. 4-12(c) and (d). The pathlength correction from Section 2.3 is used to adjust the measured H_2O mole fraction to correct for variations in the

66

flow. The 2D flow-field in (c) suggests non-uniform mixing, entrainment, additional reactions, or some combination of these. As in Fig. 4-9(b), the increase in water vapor mole fraction above the combustor surface for the pathlength-corrected measurements suggest continued reactions for roughly the first 25 mm above the catalyst surface.
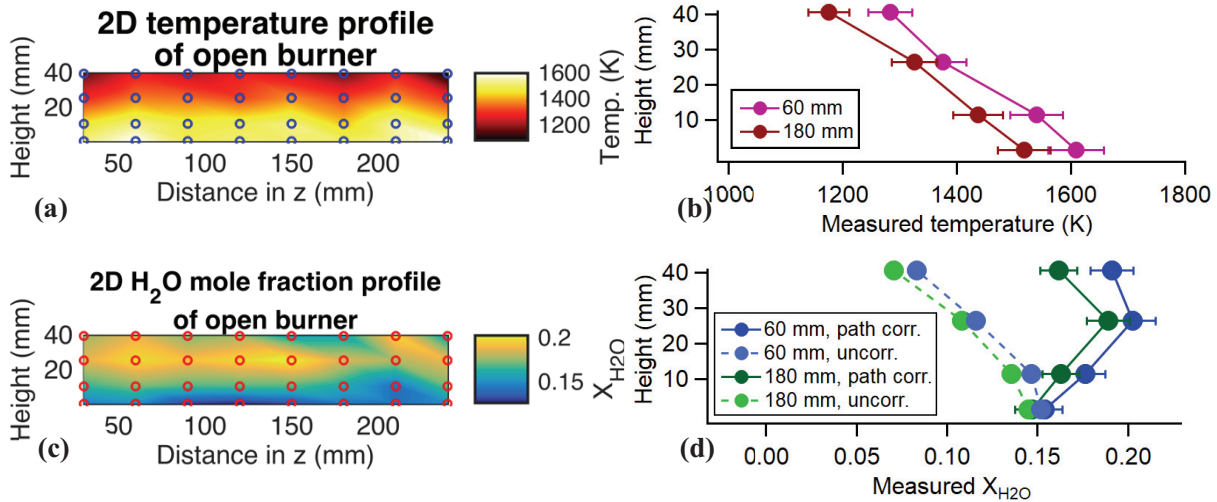
Fig. 4-12. (a) 2D measured temperature above the catalytic combustor, averaged over 30-60 s. (b) Contours of (a) at z = 60 mm and z = 180 mm with 3% uncertainty bars. (c) 2D pathlength-corrected H_2O mole fraction above the catalytic combustor, averaged over 30-60 s. (d) Contours of (c) with and without pathlength correction with 6% measurement uncertainty.

4.6 Introduction of a chilled roller above the catalytic combustor

For industrial flame processing, a product may pass over a chilled roller to prevent ignition of the material as it passes through the flame. A roller chilled by water serves as a heat sink and provides a quenching effect to the chemical reactions [9]. Therefore, it is important for industrial application of the catalytic combustor to understand how the presence of the roller may affect the spatial and temporal uniformity of the heated, buoyant jet above the combustor. Because the inlet conditions can have a large effect on the heated, buoyant jet properties, we also vary the equivalence ratio in order to gain a better understanding of the system. In industrial processing two main factors can be varied to change the flame properties: equivalence ratio and power flux.

4.6.1 Effect of the introduction of the chilled roller
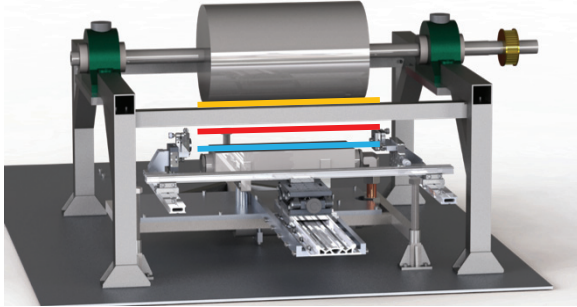
Fig. 4-14. Experimental set up of varying equivalence ratio with chilled roller characterization of heated buoyant jet with a gap of 0.375 inches. The yellow line indicates the laser beam passing through the jet right at the surface of the roller, the red indicates the midline measurement (.25") and the blue indicates the beam passing the combustor surface.

First, we seek to understand how the introduction of the chilled roller affects the flame properties without varying the inlet conditions. We achieve this by probing the temperature at three points in the flow using, as shown in Fig. 4-14. The combustor burns CH_4 and air at $\phi=0.85$ and 32 W/cm^2. The experimental setup utilizes the same catalytic combustor shown in Fig. 4-6 and the laser system described in Sec. 4.3.1. The blue, yellow and red lines in Fig. 4-14 indicate where the laser beam passes through the jet: at the combustor surface, half way in between the combustor and the roller, and at the chilled roller surface. The laser beam passes across the long width of the burner to maximize the absorption signal and improve sensitivity of the measurements. Data is collected for 30 seconds at each height at 2 ms intervals, averaged to 0.25 second intervals as per Fig. 4-8(b).
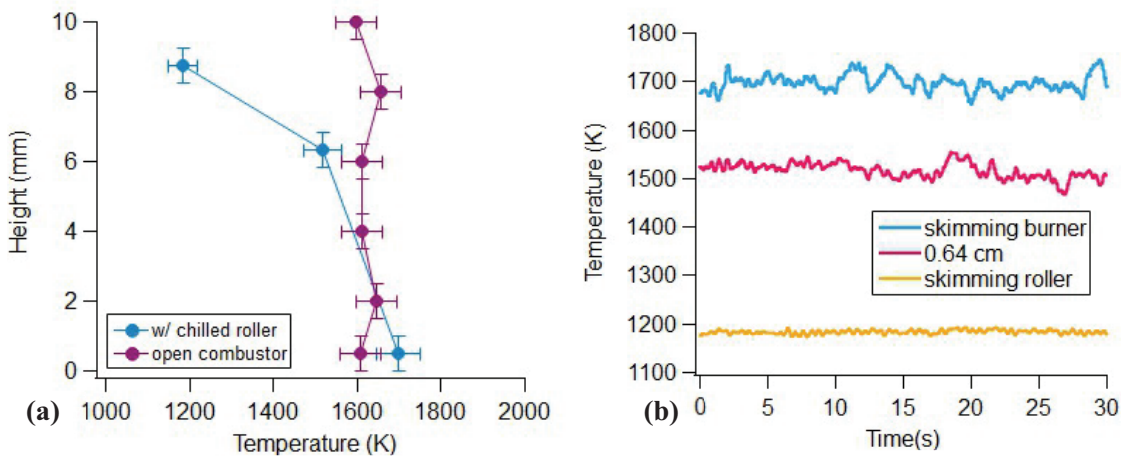
Fig. 4-13. (a) Temperature vertical profiles with the roller at $\phi=0.85$ and 32 W/cm^2 and without the roller present at $\phi=0.85$ and 24 W/cm^2. The uncertainty bars indicate 3% temperature sensor uncertainty and the beam width for vertical uncertainty. (b) Temperature as a function of time for the data collected with the chilled roller present at $\phi=0.85$ and 32 W/cm^2.

The measured temperature profiles suggest that the chilled roller has a large effect on the properties of the heated, buoyant jet. Fig. 4-13(a) compares the measured temperature vertical profile with the chilled roller present to trial 3 in Fig. 4-9. The temperatures are initially higher due a higher power flux of 32 W/cm^2, but drop off rapidly at the surface of the chilled roller. The time resolved measurements of temperature measured at each of the three heights above the burner are shown in Fig. 4-13(a). The first two heights shown 7% and 10% variation respectively, which matches with previous measurements shown in variation in Fig. 4-8(a). However, the variation drops to 3% with the introduction of the chilled roller (yellow trace). This suggests that the entrainment of cool air by the roller not only chills the temperature, but improves temporal uniformity. If this system were used for baking or materials processing, it is clear that the presence of the roller would benefit the production of uniform materials.

4.6.2   Effects of varying inlet properties

Because it is often difficult to change the roller speed or location in processing, it is often desirable to adjust treatment conditions by changing the inlet flows. Since this catalytic combustor is premixed, it is possible to control both the air and fuel flow rates. Changes in fuel flow rate will change the available energy for the combustion reactions, thus affecting the power flux of the combustor. Variations of the ratio between the air and fuel flow rates will change the equivalence ratio, thus changing the chemistry.

We began by varying the equivalence ratio to observe its effect on the buoyant jet's properties. To maintain a fixed power flux, we only vary the air flow rate and fix the fuel rate to achieve the desired power flux of 32 W/cm^2. We fixed the roller speed at 140 m/min and set the gap to 0.95 cm. Again, data was collected at three locations, shown in Fig. 4-14, this time for 60 seconds each at 2 ms intervals. The air flow rates varied from 90-140 LPM to result in variations in equivalence ratio from 0.85 (fuel-lean) to 1.33 (fuel-rich).

Fig. 4-15(a) shows the measured temperature at the three heights at the six different equivalence ratios. Each data point represents one minute of analyzed data, taken at 2 ms intervals. The temperature at the surface of the combustor peaks at the stoichiometric conditions (ϕ=1). This matches with combustion theory that says that peak temperature occurs when there is the exact amount of air needed to combust all

69

of the fuel. The temperature at the surface of the roller appears to peak slightly before stoichiometric, suggesting that profile of the jet changes with equivalence ratio or may be affected by the presence of additional combustion.

Since the maximum temperature occurs at stoichiometric conditions, we fixed the equivalence ratio at $\phi=1$ and varied the power flux to understand its effect on the fluid flow in between the catalytic combustor and the chilled roller. For film processing, power flux will often set the speed of the processing so it is
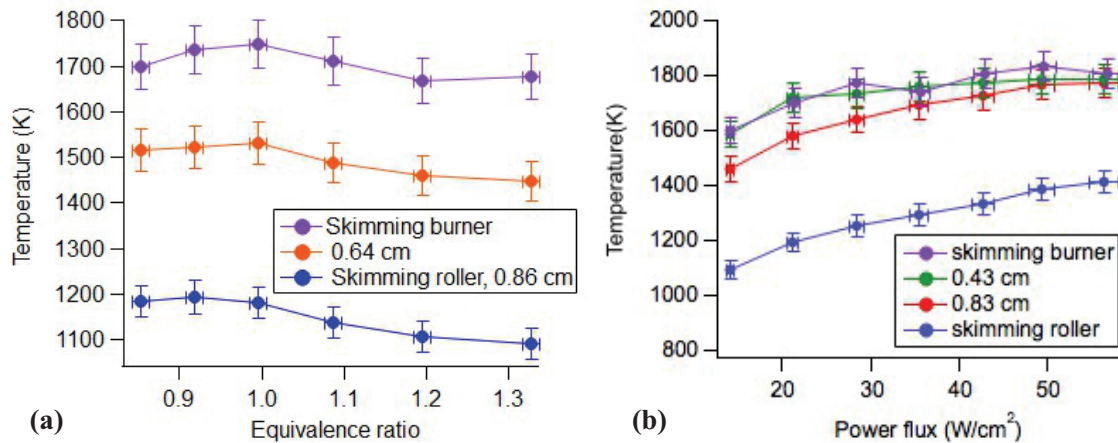
Fig. 4-15. (a) Temperature as a function of equivalence ratio at three heights in the heated jet above the catalytic combustor reacting methane and air at 32 W/cm^2 with a roller at 0.86 cm rotating at 140 m/min. (b) Measured temperature as a function of power flux at four different heights in the jet above the combustor operating on methane and air at $\phi=1$ with chilled roller at 1.27 cm. Vertical uncertainty bars are 3% uncertainty determined from the sensor validation and the horizontal uncertainty bars are uncertainty in flow rates.

important to understand the implications on heat transfer and combustion chemistry. The setup is identical to the varying equivalence ratio experiment, except the gap is set to a distance of 1.27 cm that allows four beam paths instead of three. The four beam paths are at the burner surface, the middle measurements at 0.43 and 0.83 cm (each about a third of the gap) and a final beam skimming the surface of chilled roller. The roller speed was maintained at about 140 m/min to provide continuity and to keep measurement relevant to industrial processes. Since equivalence ratio was fixed, both air and fuel rates were increased simultaneously.

Fig. 4-15(b) presents the temperature measurements as a function of seven different power fluxes. Each data point represents one minute of data, analyzed at 2 ms intervals. For all four measurement locations,

the temperature increases with power, though it appears to level off particularly at the height nearest to the combustor surface. This leveling off suggests that the catalyst is no longer increasing in temperature and may indicate continued reactions above the surface. This matches with visual inspection which shows a blue glow of the gases above the catalyst that increases as the power nears 63 W/m^2 and suggests continued combustion above the catalytic bed.

4.7   Conclusion

We characterized the temporal and spatial variation of a buoyant jet created by an industrially-relevant catalytic combustor. Measurements were performed using wavelength modulation spectroscopy (WMS) to quantify the temperature and H_2O mole fraction in the jet operating at the fuel lean condition of $\phi = 0.85$ and flow rates to match a power flux of 24 W/cm^2. Temperature was found to vary over a range of 50 K and H_2O mole fraction varies 0.015 over a minute of collected data measured immediately above the surface of the catalytic combustor. Vertical profiles of temperature and H_2O mole fraction above the center of the burner suggested additional combustion for the first 20-30 mm above the combustor, followed by entrainment and mixing of cool ambient air. Two-dimensional characterization of the near-field region of the buoyant jet suggested non-uniformities across the burner. The average temperature of 1580 K measured at the burner surface is substantially lower than temperatures measured in premixed flames at similar conditions (the adiabatic flame temperature is 2240 K), matching the expectation that the catalyst significantly reduces the temperatures required for the combustion reactions.

The temperature variation in the heated buoyant jet above the catalytic burner in conditions and configurations relevant to the application of the combustor to processing food and materials. The introduction of a chilled roller, as one might use for roll-to-roll processing, served to decrease temperature at the surface and improve the temporal uniformity of the flow. Varying the equivalence ratio or the air to fuel ratio affected the temperature profiles but did match expected trends. Variation of the amount of fuel, thus power flux, indicated that additional combustion may be occurring at the surface when the inlet flow rates are too high.

This work also presents a new approach for correcting species mole fraction in absorption-spectroscopy measurements of buoyant jets. By using CFD simulations of the jet above the combustor, we calculated an effective pathlength for gases of interest that reflected the narrowing and billowing of the heated gases in the buoyant jet. We applied this effective pathlength to improve the interpretation of the species mole fraction measurements in the core flow.

To fully optimize this system, further investigation into the presence of continued gas-phase combustion is needed. The completeness of combustion and reaction mechanisms could be explored by measurement of other combustion species, such as one or more free radicals. The effect of fuel flux or air-to-fuel ratio could also be explored to understand the limitations of the catalyst bed.

4.8   Acknowledgements

The majority of the text for this chapter has been prepared as journal article to submit to the *International Journal of Heat and Mass Transfer* **as:**

T. R. Hayden, N. T. Wimer, C. LaPointe, S. P. Nigam, J. D. Christopher, P. E. Hamlington, and G. B. Rieker, "Characterization of a buoyant jet from a catalytic combustor using wavelength modulation spectroscopy," International Journal of Heat and Mass Transfer **submitted**, (2018).

5 Large amplitude wavelength modulation spectroscopy for sensitive measurements of broad absorbers

5.1 Introduction

Despite the rapid development of renewable energy resources, more than 80% of U.S. energy is still supplied by combustion [114]. Minimizing emissions while maximizing economy and performance of combustion devices requires diagnostic tools that are fast, sensitive, and robust against the harsh environment of the combustor. Advanced gas turbine combustors are operating at pressures >50 atm, commercial coal gasifiers at >80 atm, and liquid-fueled rocket combustors at >100 atm. Laser absorption diagnostics are ideal for measurements in combustion applications because they are non-intrusive, quantitative, and require only simple optical access to the combustor [45]; however, existing laser absorption techniques have not yet reached higher than 30-50 atm at room temperature. This paper presents a diagnostic technique capable of measurement at extremely high densities (>2.5 times higher than previously published wavelength modulation spectroscopy measurements [115]). The technique combines the rapid, broad wavelength tuning of a Micro-Electro-Mechanical Systems (MEMS) Vertical Cavity Surface Emitting Laser (VCSEL) with the high sensitivity of Wavelength Modulation Spectroscopy (WMS).

The difficulty of absorption-based measurements in high-pressure systems is demonstrated in Fig. 5-1. Fig. 5-1(a) shows that for small molecules at atmospheric pressure, the absorbance spectrum is composed of distinct, narrow features corresponding to individual rotational-vibrational transitions of the absorbing gas. As gas pressure increases, so does density, leading to increased collisional effects, which broaden and blend absorption features together.

For WMS, the commonly used second harmonic signal (WMS-2f) is maximized when the modulation amplitude is 2.2 times the half width at half maximum (HWHM) of the absorption feature [116]. For traditional distributed feedback (DFB) diode lasers, the limit on the fast-tuning range of the laser source (<1nm) limits the maximum achievable modulation amplitude, causing the WMS-2f signal to decrease as density increases and absorption features broaden pas achievable tuning range of the diode. Thorlabs Inc.,

together with Praevium Research Inc., build medical imaging tools based on MEMS-VCSELs where broad and fast tuning is required. In our application, we employ a Praevium Research MEMS-VCSEL much like the one described in [117,118], operating at 1550 nm and with a tuning range of 160 nm at modulation frequencies of hundreds of kHz. This allows us to maintain the maximum modulation amplitude as pressure increases above 50 atm at room temperature (45 amagat density), as shown in Fig. 5-1. Fig. 5-1(b) further illustrates this advantage of the wide-scanning laser. As pressure and collision broadening increase, the DFB laser is unable to maintain the optimal modulation amplitude and the peak WMS-2f signal decreases significantly for pressures above 5 atm (4.6 amagat at room temperature). The MEMS-VCSEL laser continues to have a strong signal because it is able to scan the optimal modulation amplitude as features broaden together. Gas density ultimately determines the level of collisional broadening, so we describe measurement conditions in terms of density to regularize between the many different combinations of pressure and temperature in past work.

Several groups have demonstrated the utility of direct laser absorption spectroscopy in high gas density environments up to 18 amagat (20 atm at 296 K) [27,119–123]. WMS measurements have also been demonstrated at elevated density. In 2002, Fernholz et al measured O_2 at pressures up to 12 atm (11 amagat at room temperature) [124]. Most recently, Gao et al utilized WMS to measure high pressure CO_2 at densities up to 5.5 amagat (pressures of 1-10 atm at temperatures 500-1000K) [125]. Sur et al, Sun et al, Farooq et al, and Rieker et al performed WMS at densities up to 18 amagat (pressures of 20 atm at 296 K) [10,115,126–128], and Goldenstein et al measured water vapor at up to 13 amagat (50 atm at 2500 K) by performing scanned $2f$/$1f$ WMS using lasers around 2.5 μm [129]. Despite the success of these measurements, none have pushed to densities above 18.5 amagat (equivalent to 25 atm at room temperature and 103 atm at 1500 K). Other laser sensing techniques have been demonstrated at high densities, such as the work of Lempert et al measuring O_2 at densities up to 31 amagat using stimulated Raman scattering and coherent anti-Stokes Raman spectroscopy (CARS) [130], and more recent CARS work in

combustion [131,132]. CARS and other forms of Raman spectroscopy have been used in a laboratory setup

on gases, liquids and solids past 100 amg. [133].
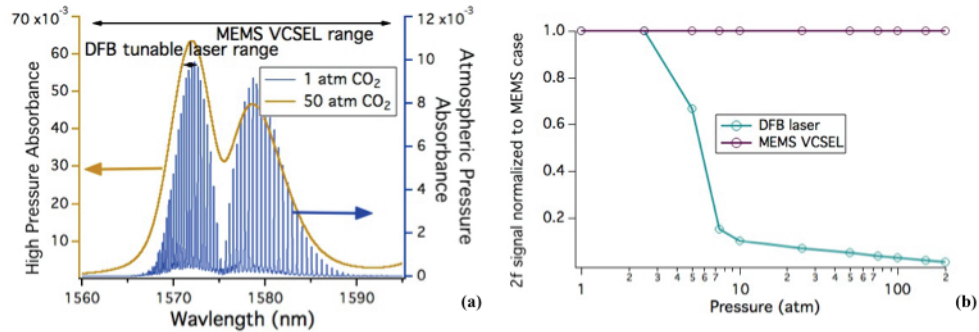
Fig. 5-1. (a) Room temperature absorbance spectrum of carbon dioxide (CO_2) at 1 atm and 50 atm, with the corresponding fast-scanning ranges of a traditional DFB diode laser and a MEMS-VCSEL laser (5% CO_2 in air, 100 cm path length). (b) Simulated 2f peak signal for CO_2 using a DFB and the MEMS-VCSEL laser centered around 1570 nm, normalized to the MEMS case, at a series of pressures. As pressure rises above a few atmospheres the DFB laser can no longer reach the optimal modulation amplitude for the broadening absorption conditions.

In this paper, we will describe and demonstrate the extension of WMS to the measurement of

extremely high-density gases using a MEMS-VCSEL laser. Although there have been previous absorption

spectroscopy experiments using a similar MEMS-VCSEL source, such as that of Stein *et al* using a 1310

nm source to perform high speed TDLAS measurements on HF and H_2O [134], this is the first

demonstration of WMS using such a source. We develop the simulations of the harmonic signals that are

required to extract information from the measured data. We discuss the unique attributes of the technique,

such as accounting for the nonlinear tuning of the MEMS-VCSEL laser over the large tuning range and a

method to characterize the rapid, broad tuning of the laser wavelength. We demonstrate the large amplitude

WMS technique on high-pressure carbon dioxide in air at densities up to 46 amagat (50 atm at room

temperature). In principle, the technique and laser are capable of far greater densities. Finally, we compare

the data to simulation. The large amplitude WMS reported here can in principle be applied to any absorber

exhibiting a wavelength-dependent absorption spectrum (which will induce a second harmonic signal if the

laser is modulated across a significant spectral feature). Therefore, the technique may be useful for any

species demonstrating broad absorption features, such as large molecular species and liquids. The

technique will benefit from further evolution of the MEMS-VCSEL technology to new wavelength ranges [135].

5.2 Impact of laser tuning characteristics on WMS with a MEMS

Traditionally, WMS harmonic signals are simulated using Fourier expansion of the spectral absorbance [24,136,137]. However, the Fourier expansion becomes intractable when the laser intensity and wavelength modulation are highly nonlinear. Unlike typical injection current tuning, the MEMS-VCSEL changes the laser cavity length using electrostatic actuation. Electrostatic tuning does not directly change the intensity of the laser. Instead, the wavelength-dependent features of the laser mirrors, gain medium, and experimental system components (transmit/receive optics, optical cell windows, etc.) cause intensity modulation as the wavelength is tuned. Over the wide tuning range of the MEMS-VCSEL (~160nm), these features are not monotonic and therefore create higher order frequencies in the intensity. The MEMS-VCSEL's nonlinear intensity profile during wavelength scanning negates the linearity assumptions often applied to DFB laser-based WMS, where a Fourier expansion is employed. Instead, we use a new approach similar to Refs [16,17,138] where we directly model the expected transmitted intensity of the laser through the sample region using the actual measured incident intensity and Beer's Law with time varying components, Eq. (5-1).

$$I_t(t) = I_0(t)exp\left(-\alpha\big(\lambda(t)\big)\right) \tag{5-1}$$

where I_0 is the incident intensity, α is absorbance, and $\lambda(t)$ is the wavelength as a function of time. We then process the simulated transmitted intensity with a digital lock-in amplifier that isolates the harmonic signal of interest.

This technique requires three inputs: (1) $I_0(t)$, the incident laser intensity (before absorption), (2) $\lambda(t)$, wavelength as a function of time, and (3) $\alpha(\lambda)$, absorbance as a function of wavelength. Each input will be explained in detail in the following subsections.

5.2.1 Incident intensity characterization, I_0

To simulate the transmitted intensity, $I_t(t)$, via Beer's law we need to first measure the intensity incident on the gas sample, which is denoted I_0. The MEMS-VCSEL laser used for this experiment is capable of

scanning ~160 nm centered around 1570 nm at frequencies up to 400 kHz. A drive voltage is passed to the laser, which electrostatically pulls down the MEMS mirror that forms the optical cavity above the VCSEL. The laser exhibits nonlinear relationships between the drive signal and both laser intensity and wavelength. Fig. 5-2 shows the laser intensity variation when a fast sinusoidal modulation signal is passed to the laser. Fig. 5-2(b) illustrates the non-sinusoidal intensity signal that results from the application of this fast sinusoidal modulation (Fig. 5-2(a)). Fig. 5-2(d) shows the laser intensity when a lower frequency linear voltage sweep (Fig. 5-2(c)) is also applied to slowly tune the center wavelength about 25 nm across the absorption features (as required to obtain a wavelength-resolved WMS spectrum). It is evident that the amplitude of the laser intensity modulation is center-wavelength-dependent. Therefore, the laser intensity cannot be simulated by a simple sinusoid, as is done in traditional WMS modeling. Instead, we measure the laser output intensity directly and incorporate the measured output intensity variation into the simulation.
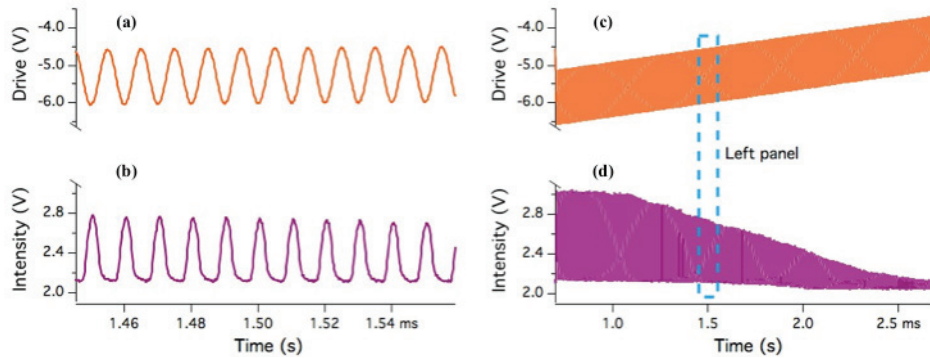
Fig. 5-2. (a) Sinusoidal voltage input signal to the laser used to modulate the laser wavelength (100 kHz modulation frequency); (b) Resulting intensity variation as a function of time, measured concurrently with the voltage input; (c) Voltage input signal as center wavelength is tuned with additional 500 Hz voltage sweep; (d) Resulting intensity variation for one full voltage sweep with fast modulation applied.

In order to track laser output, we need to measure both the temporal variation of the laser intensity and its distortion due to non-linear system effects. These characterizations require two separate measurements. To account for temporal variation, we make a concurrent, reference intensity measurement of the light coming from the laser. This is achieved by passing the laser light through a fiber splitter and

sending half of the light to a photodetector, allowing for a concurrent intensity measurement of laser output, denoted as I_{ref}. This characterization setup is shown in the experimental set up in Sec. 5.3.

To account for distortion due to elements of the optical setup (cell windows, etc.), we characterize the system response by passing a laser through the measurement cell when there is only non-absorbing gas present. This measurement accounts for etalons and optical effects particular to the experimental setup, such as variations in light transmission due to pressure-induced stress on the windows. This measurement is denoted I_{na} to denote non-absorbing background.

We combine these measurements in Eq. (5-2) by taking the ratio of the reference intensity during the sample measurement ($I_{ref, sample}$) to the reference measurement taken concurrently with the non-absorbing measurement through the cell ($I_{ref,na}$), which is then multiplied by the transmitted intensity through the non-absorbing gas in the cell (I_{na}).

$$I_0 = \left(\frac{I_{ref,sample}}{I_{ref,na}}\right) I_{na} \qquad (5\text{-}2)$$

The resulting I_0 represents the incident intensity that we would expect to measure for the system of interest, corrected for both the non-uniformities in the optical cell and temporal drifts of the laser itself.

5.2.2 Wavelength characterization, λ(t)

It is understood that electrostatic MEMS mirrors reduce the cavity length of the laser as the square of the applied voltage [139] We expect, as with intensity variation, the wavelength of the MEMS laser will not vary linearly with the drive modulation, so the standard WMS model assumption of a constant sinusoidal wavelength modulation is not valid.

The combination of the extremely large wavelength sweep range and fast sweep frequency of the laser makes large amplitude WMS possible, but also makes wavelength characterization difficult. Typically the wavelength variation of a laser can be characterized using a combination of an optical spectrum analyzer (OSA), a wavemeter, and/or an etalon with a well-known free spectral range [140]. For typical DFB lasers, the fast and slow modulations can be considered independent and can thus be turned off to perform a two-part characterization. First, an absolute characterization of the center wavelength with the modulation

turned off is performed with an OSA or wavemeter (which have slow acquisition rates). Then, the modulation is turned on and an etalon is used to provide a relative measurement of the wavelength modulation amplitude and slow scanning of the center wavelength (if used). Because the modulation amplitude varies significantly as the center wavelength of the MEMS-VCSEL is scanned, this characterization procedure does not work well for the MEMS-VCSEL.

Instead, we use a reference cell containing Carbon Monoxide together with a high-speed data acquisition system to provide absolute wavelength characterization at high speed. A NIST SRM 2515 Carbon Monoxide Absorption Reference Cell consists of a small chamber of $^{12}C^{16}O$ kept at a well-known temperature and pressure, such that the line-center wavelength of each CO absorption line is well known. The CO absorption cell thus provides an absolute wavelength reference as the laser sweeps over the known CO absorption lines, even during a fast scan. An example of the characterization using this method is shown in Fig. 5-3, where Fig. 5-3(a) shows the transmitted intensity of the laser through the reference cell during a single cycle of the fast modulation and the Fig. 5-3(b) shows the conversion to wavelength as a function of time based on the CO peak locations. The conversion from intensity measurement to wavelength is done by applying a peak finding algorithm to the transmitted intensity spectrum and matching the corresponding peaks to the known absolute center wavelengths of the $^{12}C^{16}O$ absorption features. We repeat the process to characterize fast modulation cycles at multiple locations throughout the slow voltage sweep.
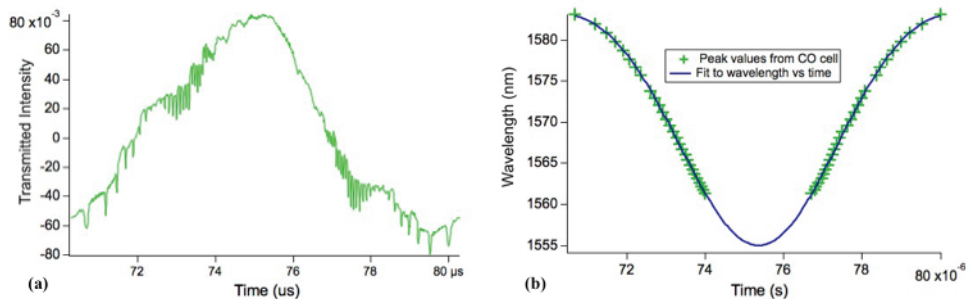
Fig. 5-3. (a) Transmitted intensity through the SRM 2515 CO cell as a function of time when the fast sine wave voltage modulation is applied to the laser. Variations in the baseline laser intensity through the CO cell are due in part to the nonlinear laser intensity modulation of the source and etalon effects in the un-optimized reference cell; (b) Wavelength as a function of time determined from the data in the left panel: location of CO absorption peaks (points) and curve fit (line).

Each characterization results in a center wavelength, and first and second harmonic modulation amplitude at a different point in the slow voltage sweep. The nature of the electrostatic modulation results in wavelength modulation that varies quadratically throughout the slow scan, so the measured wavelength variation across the slow scan is fit with Eq. (5-3).

$$\lambda(t) = (\lambda_0 + \lambda_1 t + \lambda_2 t^2) + (a_0 + a_1 t + a_2 t^2)\sin(2\pi f t + \phi_1)$$
$$+ (b_0 + b_1 t + b_2 t^2)\sin(4\pi f t + \phi_1)$$

(5-3)

where λ_i are the terms of the second order variation of the center wavelength, a_i are the terms of the first harmonic amplitude variation, b_i are the terms of the second harmonic amplitude, f is the frequency of the fast modulation, and ϕ_1 and ϕ_2 are the phase offsets between intensity and wavelength variation for the two harmonics, respectively. In future applications we will utilize a synthesized voltage waveform to account for the nonlinear voltage and wavelength relationship, as opposed to the simple sinusoid and saw-tooth driving voltage used in this experiment [117].
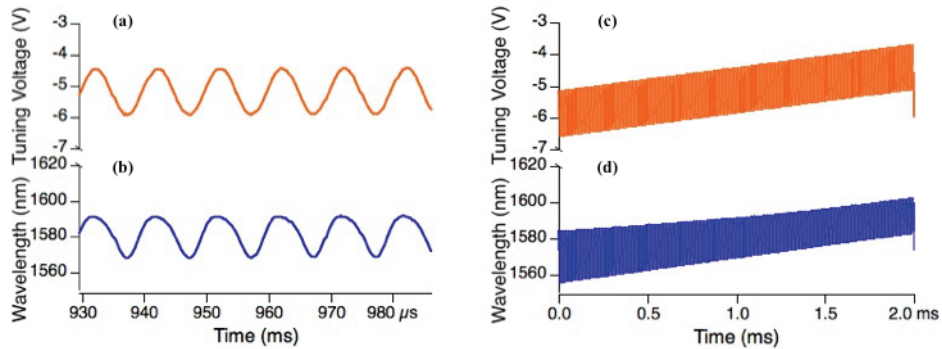
Fig. 5-4. (a) Sinusoidal voltage input signal to the laser used to modulate the laser wavelength (100 kHz modulation frequency); (b) Resulting wavelength variation as a function of time; (c) Voltage input signal as center wavelength is tuned with additional 500 Hz voltage sweep; (d) Resulting wavelength variation for one full voltage sweep with fast modulation applied.

During the characterization, up to twenty $^{12}C^{16}O$ absorption peaks are swept twice per ~10 microsecond modulation cycle. A fast data acquisition system (NI PXIe-7975R with 5761 digitizer sampling at 250 MHz) is required to resolve the narrow low-pressure CO absorption lines in the reference cell. The input to the fast DAQ is low impedance and the laser tuning input is high impedance. The low impedance DAQ alters the laser tuning voltage if the drive voltage is simultaneously connected to the laser

80

and the fast DAQ. Therefore, to avoid alteration of the drive signal during characterization, we did not measure the laser input voltage simultaneously during wavelength characterization. Because neither the concurrent intensity nor the laser tuning voltage are measured concurrently with the wavelength characterization, the phase shift between the laser intensity and laser wavelength modulation, ϕ_1 and ϕ_2, are not directly measured for the experiments in this paper. Therefore, we had to infer these phase shifts during the comparison of the model to the experiments. Future implementations will simultaneously measure laser intensity on the fast DAQ during wavelength characterization to measure these phase shifts.

5.2.3   Absorbance model, α(λ)

We utilized the spectral database HITRAN 2012 together with Voigt absorption profiles to simulate the spectral absorbance, $\alpha(\lambda)$, as shown in Fig. 5-1(a) This method is known to be inaccurate for simulating high pressure absorbance due to the breakdown of the assumptions inherent to the Lorentzian collisional broadening model used in the Voigt profile, in addition to line mixing, and other effects [10]. However, improved data on CO_2 broadening at high densities does not yet exist to provide an improved model. Fortunately, it has been shown that the impact of these non-ideal effects are lessened for WMS (vs. direct absorption spectroscopy) [10]. Still, we expect error in the simulated WMS signal induced by inaccuracy of the absorbance model at high-density conditions.

To assess the impact of the error in the absorbance model, the comparisons in Sec. 5.3 show an additional WMS simulation that includes a wavelength-dependent scaling to account for the breakdown of the Voigt profile at high CO_2 densities. Several empirical corrections have been developed to account for the shift of absorbance from the wings of an absorption feature toward the center due to non-Lorentzian effects at high densities. We utilized the wavelength-dependent empirical correction developed by Perrin and Hartman, which is multiplied by the simulated absorbance for each individual spectral line [141]. The model defined by Perrin and Hartman accounts for the reduction of absorption in the far wings of features, but does not conserve the integrated absorbance by enhancing absorption near line center (as expected, and shown in similar corrections developed for water vapor [142]). We therefore enhanced the scaling near the center region of the piece-wise function correction to conserve the integrated absorbance for each

81

absorption line. We emphasize that this correction was applied to determine the influence of the breakdown of the Voigt profile on the WMS simulation, and is not an alternative to future development of proper high-density absorption models. Accounting for linemixing and other effects is also necessary to further improve the fidelity of the absorption models [128].

5.3 Demonstration

To test the MEMS-VCSEL large amplitude WMS technique, we perform measurements on samples of high-density room temperature CO_2 (equivalent density to 255 atm at 1500 K). Note that the technique is capable of probing even higher densities or broader spectra, as these experiments only use a modulation amplitude of ~30nm, while the laser is able to modulate up to 160nm. We selected carbon dioxide because it is a major product of combustion and has absorption features in the wavelength range of the MEMS–VCSEL laser that are relatively free from water vapor absorption interference. For the large amplitude WMS technique to be useful as a gas concentration sensor, we must be able to interpret the measured signals
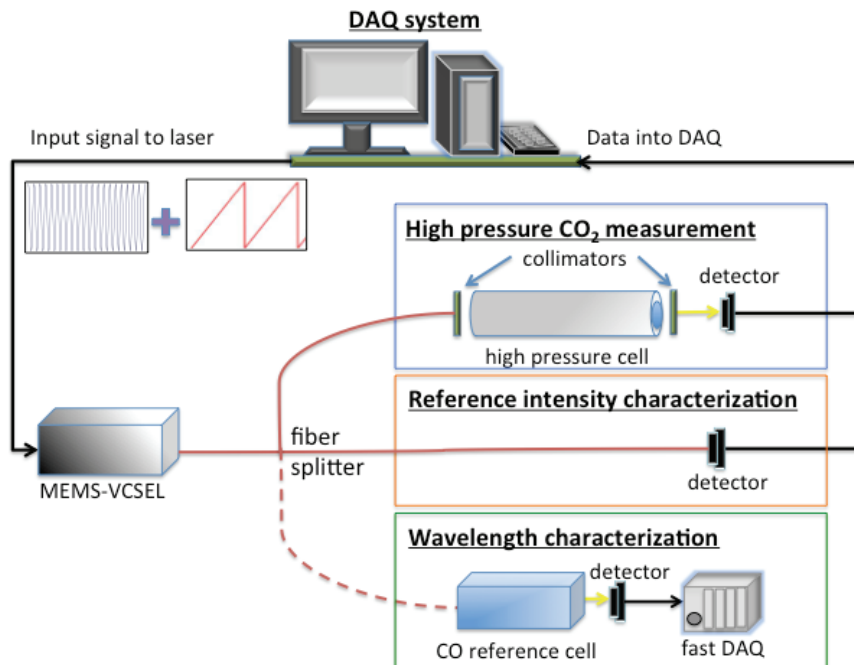
Fig. 5-5. Experimental setup for large amplitude WMS of high pressure CO_2 using a MEMS-VCSEL. The laser intensity is characterized simultaneously with the high pressure cell measurements, and the wavelength is characterized before or after the experiment. The system listed as the DAQ system is a desktop computer with a NI PCI 6110 while the fast DAQ is the NI PXIe-7975R.

82

with a simulation. Therefore, the goal of the experiment was to demonstrate that the measured large-amplitude WMS data at high density match simulation and scale linearly with concentration.

A schematic of the experimental setup is shown in Fig. 5-5, including the wavelength and intensity characterization setups. The wavelength characterization does not need to be performed synchronously with the sample measurement. A National Instruments PCI 6110 data acquisition board outputs the drive voltage to the laser and records the transmitted intensity through the CO_2 cell and directly to the intensity characterization detector. The laser drive signal, combines a 500 Hz saw-tooth sweep of the center wavelength and a 100kHz fast sinusoidal modulation. The drive signal is also recorded to the DAQ system as a reference to synchronize simulated I_0 signals with the measured data. The DAQ system samples at 5 MHz, which is more than sufficient to capture the second harmonic detector signal at 200 kHz. A software lock-in amplifier isolates the WMS second harmonic from the transmitted intensity signal. To be consistent, the same software lock-in amplifier is used to separately post-process both the measured data and the simulated transmitted intensity that forms the basis of the WMS model.

The highly nonlinear intensity modulation of the laser signal induces a strong residual amplitude modulation (RAM) background signal – i.e. there is a large (but stable) background WMS second harmonic signal even when an absorbing gas is not present. This is typical (though at a smaller magnitude) even in diode laser-based WMS, and the signal is normally subtracted from both the simulation and data [24]. Here, we measure the RAM background from the laser intensity characterization signal (I_0), and subtract from both the data and simulation. It is also possible to manipulate the laser output to minimize the measured background harmonic signals [117]. To perform the background subtraction, we pass the simulated transmitted intensity, the measured transmitted intensity, and the I_0 signal through the digital lock-in. Because the 2f signal is directly proportional to laser intensity, differences in baseline intensity values among the signals will cause the absolute value of the 2f magnitudes to be different. Therefore, the average magnitude of each intensity signal (simulated or measured) is scaled to match before they are passed through the lock-in. The magnitude of the background-subtracted signals is then calculated from Eq. (5-4):

$$2f = \sqrt{\left(2f_{x,signal} - 2f_{x,background}\right)^2 + \left(2f_{y,signal} - 2f_{y,background}\right)^2} \qquad (5\text{-}4)$$

Where the x and y components of the signal are the two orthogonal outputs from the lock-in [24].
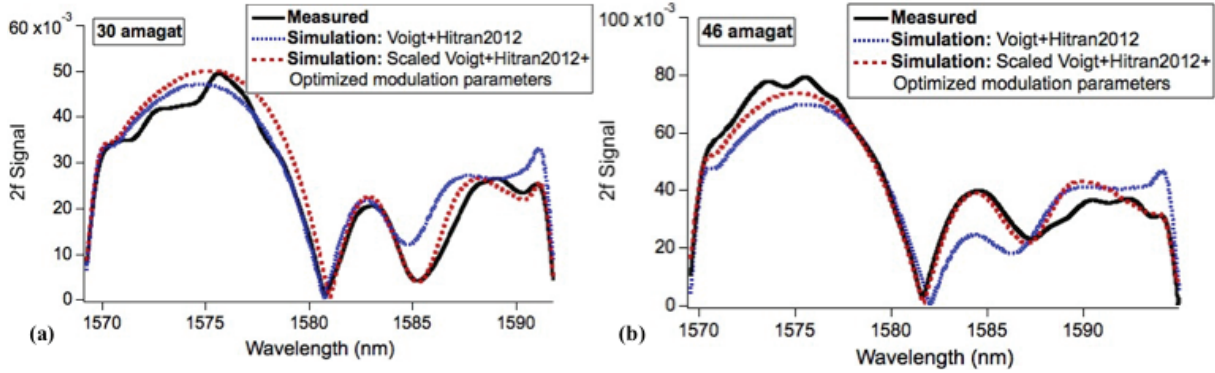
Fig. 5-6. (a) Simulated and measured second harmonic signal for 14.7% CO_2 mixed with air at 30 amagat (32.7 atm at 295K). (b) Simulated and measured second harmonic signal for 12% CO_2 mixed with air at a density of 46 amagat (50.5 atm at 300K). The red dash trace was obtained by scaling the simulated Voigt profile with a modified χ-function correction to account for non-Lorentzian lineshape effects that occur at high density, and by optimizing the wavelength modulation parameters within their characterization uncertainty.

In Fig. 5-6 we plot the measured and simulated results at 32.7 atm and 50.5 atm. Each plot contains two simulations: one that utilizes the measured wavelength modulation parameters and standard Voigt profile absorbance model, and another that utilizes modulation parameters that are optimized within the uncertainty of the measured modulation parameters and an absorbance profile using the scaled χ function correction. The original simulation using only measured parameters and a standard Voigt profile-based model, shows general agreement with the measurement, but suffers from the known inaccuracy at high densities of the absorption model and uncertainty in the modulation parameters stemming from the difficult wavelength characterization. The second simulation explores the influence of these potential sources of uncertainty by adding the scaled χ-function correction to the absorption model, and optimizing the wavelength modulation parameters by varying the λ_i, a_i, and b_i parameters within one standard deviation of their fit values. The revised simulation, shown in dashed red, tracks more closely with the measured 2*f* data, suggesting that these sources of uncertainty are important. Multiple reflections in the cell windows or other noise in the optical cell may account for the remaining discrepancy, particularly the ripple in the measured

84

signal. Overall, the match between the simulation and measurement demonstrate that with refinement, the technique can be used to extract thermodynamic properties from the data without calibration.
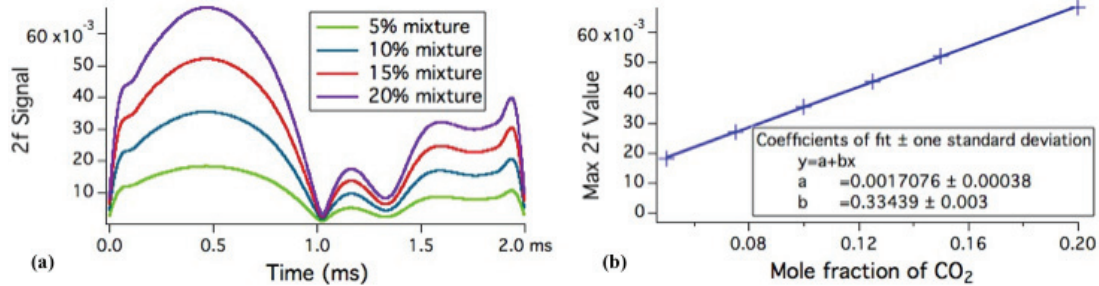
Fig. 5-7. (a) Simulated second harmonic signal for four different CO_2 mole fractions in air at room temperature, 101 cm path length and 32.7 atm. (b) The maximum 2f value from the graph on the left as a function of mole fraction.

If the measured $2f$ signal is linearly proportional to concentration, the measured signal can be used to extract concentration even without an accurate model, if a single point calibration at a known condition is possible (as was used for early demonstrations of the WMS technique [143]). Fig. 5-7 shows simulations for several different concentrations. The left panel shows that the WMS-2f signal increases with the concentration of the mixture. The right panel demonstrates that the WMS-2f peak signal exhibits the expected linear relationship with species mole fraction.

5.4   Conclusion

This paper presents the extension of the sensitive wavelength modulation spectroscopy technique to large modulation depths by using a MEMS-VCSEL laser. We demonstrated the potential of the technique by performing measurements at 2.5x higher density than previous measurements (46.3 amagat, 50.5 atm at room temperature). Through extensive characterization of the laser tuning properties and implementation of a new WMS model, we demonstrate good agreement between the model and the measured data. Although discrepancies remain, the agreement suggests that this sensor has the potential to measure the thermodynamic properties such as concentration and temperature of broadly absorbing species.

5.5   Acknowledgements

The majority of the text for this chapter is published in *Optics Express* as:

T. R. S. Hayden and G. B. Rieker, "Large amplitude wavelength modulation spectroscopy for sensitive measurements of broad absorbers," Opt. Express, OE 24, 27910–27921 (2016).

6 Dissertation Summary and Future Directions

6.1 Dissertation Summary

In this dissertation, wavelength modulation spectroscopy is extended in its capabilities and utilized in new environments. A new OH sensor using WMS is developed with the aid of a new spectral parameter database near 1491 nm extracted from the first dual frequency comb spectroscopy measurements above a premixed flame. This work also provides the first experimental demonstration of the connection between the presence of OH radical in a premixed flame and the oxidation of polypropylene film in flame processing. Additionally, it adds to the current understanding of the thermodynamic properties of a heated, buoyant jet above a catalytic combustor that could be used for industrial applications. Finally, it presents the highest density WMS to-date that demonstrates the possibility of widely-scanning WMS to measure broad absorbers.

6.2 Future Research Directions

6.2.1 Combination of WMS and dual comb spectroscopy

As exemplified in the work presented in Ch. 2, both WMS and dual comb spectroscopy have their strengths that could be leveraged together for increased sensor versatility. WMS has been shown to be a fast, robust, and quantitative method for measuring temperature and species mole fraction in both this dissertation and past work [24,138,144]. However, WMS has traditionally been performed using tunable diode lasers, which having a very reliable tuning range of 1-2 nm that needs to be characterized prior to analysis. This is ideal for probing narrow, isolated absorption transitions, such as those of H_2O at low temperatures. We demonstrate in this work the extension of the technique to large scanning ranges [29]; though, there are still challenges to overcome, such as linearizing the output of the laser.

On the other hand, dual comb spectroscopy is a broadband measurement technique with a well-known wavelength axis. The broadband capabilities make dual comb spectroscopy ideal for probing systems where the absorption transitions are not well-characterized, such as systems with elevated temperatures or high densities. The well-known wavelength axis is ideal for minimizing uncertainties in spectral parameter extraction that would be difficult using a diode laser. Current dual comb spectroscopy

approaches are limited in time resolution in combustion systems to approximately one second due to insufficient short-term signal-to-noise ratio. Beam steering caused by fluctuations in the density may also reduce the signal-to-noise more than 1f-normalized WMS. Finally, the current cost and sensitivity of the equipment to environment fluctuations makes dual comb spectroscopy currently intractable in certain industrial applications.

The complimentary nature of the strengths and weaknesses of these two techniques suggest that application of the two together would provide a versatile sensor package. Before they could be utilized together, the two sensors would need to be compared in a controlled manner for sensor validation. This validation could be broken down into three experiments: room temperature species mole fraction detection, elevated temperatures at a fixed species mole fraction and probing a time-varying system. In the first experiment, the species mole fraction and temperature would be fixed and maintained at fixed values. This controlled experiment would compare the precision and signal-to-noise of the two sensors, as well as develop Allan deviation plots to inform averaging times. The second experiment would seek to compare the precision and accuracy of the two techniques in measuring known, elevated temperatures in a fixed-temperature furnace. Finally, the third experiment would illustrate the time resolved nature of both sensors to provide a point of comparison for future work.

Fig. 6-1. 2D simulation of temperature in a heated buoyant jet

Performing a series of studies of the precision and accuracy of each of these techniques would then enable the two techniques to be combined to probe unknown systems. For example, the frequency combs could serve as a wavelength reference for the wavelength characterization of the diode lasers, as needed for the fitting WMS analysis presented in Sec. 1.2. Improving the accuracy of the wavelength characterization would improve the accuracy of the WMS sensor in capturing the thermodynamic properties of an unknown system. It would also be advantageous to co-propagate light from the two sensors through a gas sample of interest, thus leveraging the advantages of both techniques. This co-propagation could be achieved by cross-

polarizing the two light sources to avoid interference between the light, which has been tested already in the premixed ribbon burner system. Hence, combining these two valuable laser diagnostics together could provide a valuable tool for both combustion system characterizations.

6.2.2 Characterizing the temperature of interest

The pathlength correction approach presented in Ch. 4 of this dissertation highlights one of the challenges of utilizing absorption spectroscopy techniques in industrial combustion systems, they are not spatially uniform. Due to the competing effects of momentum flux and buoyancy, the width of a flame or buoyant jet may vary significantly, as shown in Fig. 6-1. The pathlength correction approach provides a method to account for this variation in species mole fraction measurements.

For many applications, the two-line thermometry approach used in this dissertation to measure temperature using WMS eliminates the effects of varying pathlength. However, it becomes difficult to interpret measured temperatures when the width of the probed flow is small compared to the distance between the optics. The background signal due to ambient air can be measured previous to combustion, but may not fully capture the background during combustion as the ambient air will heat up and diffuse with combustion products. Additionally, non-uniform, Gaussian-type temperature profiles also perturb the measured line-of-sight temperatures away from the actual average temperature due to nonlinear weighting by the individual absorption features that are used.

Techniques such as the onion-peeling method or Abel transform have been utilized to overcome this problem in axially symmetric flows [145]. However, there is no known approach for extracting temperatures in a flame or jet that is rectangular or a more complicated geometry. There have been scaling laws developed to describe the properties of reacting and non-reacting buoyant jets [146]. Additionally, computational fluid dynamics (CFD) simulations of the experimental set up could provide insight needed to better interpret these absorption-weighted temperature measurements. Future work would look to couple one of these numerical methods with the experimental measurements performed using WMS to improve temperature sensing by WMS in a reacting flow.

89

6.2.3 Studies of the effect of the distance between the chilled roller and the premixed flame exit on flame structure and polymer film processing

The work presented in Chapter 3 illustrates the effect the chilled roller has on the premixed flame and the distance between the burner and roller may affect polymer film processing. Previous work suggested that the optimal distance for film placement is 1-2 mm beyond the visible flame tips for maximum surface oxidation [79]. However, it is clear from the work presented in Chapter 3 that both OH mole in the flame and the surface oxidation are maximized at smaller gap sizes. Therefore, further investigation into the effects of the burner to roller gap on OH presence and surface oxidation is needed.

One way this could be studied further is by investigating through CFD the effects of this gap size. Before this can be pursued, further understanding of the chilled roller boundary condition is needed. It is clear that there is significant heat transfer from the flame to the chilled roller as measured temperatures drop rapidly near the surface (shown in Fig. 3-3). Thermocouples could be used to probe the inlet and exit H_2O temperatures in the chilled roller. The change of temperature could then be used to calculate the heat transfer to the fluid from the flame. Repeating this for different burner to roller gaps could elucidate the heat transfer changes with gap. Additionally, probing the temperature variation near the roller surface using WMS could provide insight into the heat transfer occurring at different gap sizes. The understanding of the boundary condition could be incorporated into a CFD simulation of the experiment that could be used to study the effect of the gap size.

In addition to numerical studies, other experimental methods could be utilized to study the changes in the flame structure with changing gap size. Stroud *et al* previously used Schlieren imaging to study the density gradients in the flame flow fields in between the burner and roller [104]. This approach could be used again to study how the flow may be changing at different gap sizes. Previous work with planar laser induced fluorescence (PLIF) measured OH in premixed flames, indicating that it could be an ideal candidate for characterizing OH presence in at the roller surface as the burner to roller gap changes [147]. Ideally, these measurements would be carried out by using the OH sensor presented in Ch. 2 and a smaller beam size to probe the OH variation at the surface. As shown in Ch. 3, it is particularly important to understand

the OH presence on the roller surface as it will have a large effect on surface oxidation of flame treated film. Hence, a better understanding of the burner to roller gap effects on the flame properties will aid in the optimization of flame processing of polymer films.

91

7 References

1. C. S. Alexander, M. C. Branch, M. Strobel, M. Ulsh, N. Sullivan, and T. Vian, "Application of ribbon burners to the flame treatment of polypropylene films," Progress in Energy and Combustion Science **34**, 696–713 (2008).

2. R. M. Nussbaum, "Oxidative activation of wood surfaces by flame treatment," Wood Sci.Technol. **27**, 183–193 (1993).

3. B. S. Gupta and M.-P. G. Laborie, "Surface Activation and Adhesion Properties of Wood-Fiber Reinforced Thermoplastic Composites," The Journal of Adhesion **83**, 939–955 (2007).

4. P. H. Winfield, A. F. Harris, and A. R. Hutchinson, "The use of flame ionisation technology to improve the wettability and adhesion properties of wood," International Journal of Adhesion and Adhesives **21**, 107–114 (2001).

5. S. A. Cottilard, *Catalytic Combustion* (Nova Science Publishers, Inc., 2011).

6. R. E. Hayes and S. T. Kolaczkowski, *Introduction to Catalytic Combustion* (CRC Press, 1998).

7. C. F. Edwards, S. L. Miller, M. N. Svreck, and S. Ramakrishnan, *Development of Low-Exergy-Loss, High-Efficiency Chemical Engines*, GCEP Technical Report (Stanford University, 2006).

8. M. N. Svrcek and C. F. Edwards, "Emissions from an extreme-compression, free-piston engine with diesel-style combustion," International Journal of Engine Research **13**, 238–252 (2012).

9. S. Ramakrishnan and C. F. Edwards, "Maximum-efficiency architectures for steady-flow combustion engines, II: Work-regenerative gas turbine engines," Energy **72**, 58–68 (2014).

10. G. B. Rieker, J. B. Jeffries, and R. K. Hanson, "Measurements of high-pressure CO2 absorption near 2.0 μm and implications on tunable diode laser sensor design," Applied Physics B **94**, 51–63 (2009).

11. A. Farooq, J. B. Jeffries, and R. K. Hanson, "Measurements of CO2 concentration and temperature at high pressures using 1f-normalized wavelength modulation spectroscopy with second harmonic detection near 2.7 um," Appl. Opt. **48**, 6740–6753 (2009).

12. P. J. Schroeder, M. J. Cich, J. Yang, W. C. Swann, I. Coddington, N. R. Newbury, B. J. Drouin, and G. B. Rieker, "Broadband, high-resolution investigation of advanced absorption line shapes at high temperature," Phys. Rev. A **96**, 022514 (2017).

13. L. S. Rothman, I. E. Gordon, R. J. Barber, H. Dothe, R. R. Gamache, A. Goldman, V. I. Perevalov, S. A. Tashkun, and J. Tennyson, "HITEMP, the high-temperature molecular spectroscopic database," Journal of Quantitative Spectroscopy and Radiative Transfer **111**, 2139–2150 (2010).

14. I. E. Gordon, L. S. Rothman, C. Hill, R. V. Kochanov, Y. Tan, P. F. Bernath, M. Birk, V. Boudon, A. Campargue, K. V. Chance, B. J. Drouin, J.-M. Flaud, R. R. Gamache, J. T. Hodges, D. Jacquemart, V. I. Perevalov, A. Perrin, K. P. Shine, M.-A. H. Smith, J. Tennyson, G. C. Toon, H. Tran, V. G. Tyuterev, A. Barbe, A. G. Császár, V. M. Devi, T. Furtenbacher, J. J. Harrison, J.-M. Hartmann, A. Jolly, T. J. Johnson, T. Karman, I. Kleiner, A. A. Kyuberis, J. Loos, O. M. Lyulin, S. T. Massie, S. N. Mikhailenko, N. Moazzen-Ahmadi, H. S. P. Müller, O. V. Naumenko, A. V. Nikitin, O. L. Polyansky, M. Rey, M. Rotger, S. W. Sharpe, K. Sung, E. Starikova, S. A. Tashkun, J. V. Auwera, G. Wagner, J. Wilzewski, P. Wcisło, S. Yu, and E. J. Zak, "The HITRAN2016 molecular spectroscopic database," Journal of Quantitative Spectroscopy and Radiative Transfer **203**, 3–69 (2017).

15. P. J. Schroeder, M. J. Cich, J. Yang, F. R. Giorgetta, W. C. Swann, I. Coddington, N. R. Newbury, B. J. Drouin, and G. B. Rieker, "Speed-dependent Voigt lineshape parameter database from dual

frequency comb measurements up to 1305 K. Part I: Pure H2O absorption, 6801–7188 cm−1," Journal of Quantitative Spectroscopy and Radiative Transfer **210**, 240–250 (2018).

16. C. S. Goldenstein, C. L. Strand, I. A. Schultz, K. Sun, J. B. Jeffries, and R. K. Hanson, "Fitting of calibration-free scanned-wavelength-modulation spectroscopy spectra for determination of gas properties and absorption lineshapes," Applied Optics **53**, 356 (2014).

17. K. Sun, X. Chao, R. Sur, C. S. Goldenstein, J. B. Jeffries, and R. K. Hanson, "Analysis of calibration-free wavelength-scanned wavelength modulation spectroscopy for practical gas sensing using tunable diode lasers," Meas. Sci. Technol. **24**, 125203 (2013).

18. R. K. Hanson, R. M. Spearrin, and C. S. Goldenstein, *Spectroscopy and Optical Diagnostics for Gases* (Springer, 2015).

19. R. K. Hanson and P. K. Falcone, "Temperature measurement technique for high-temperature gases using a tunable diode laser," Appl. Opt., AO **17**, 2477–2480 (1978).

20. C. S. Goldenstein and R. K. Hanson, "Diode-laser measurements of linestrength and temperature-dependent lineshape parameters for H2O transitions near 1.4 µm using Voigt, Rautian, Galatry, and speed-dependent Voigt profiles," Journal of Quantitative Spectroscopy and Radiative Transfer **152**, 127–139 (2015).

21. P. Kluczynski and O. Axner, "Theoretical Description Based on Fourier Analysis of Wavelength-Modulation Spectrometry in Terms of Analytical and Background Signals," Appl. Opt. **38**, 5803–5815 (1999).

22. John Scofield, "Frequency-domain description of a lock-in amplifier," American Journal of Physics **62**, 129–132 (1994).

23. J. Reid and D. Labrie, "Second-harmonic detection with tunable diode lasers — Comparison of experiment and theory," Appl. Phys. B **26**, 203–210 (1981).

24. G. B. Rieker, J. B. Jeffries, and R. K. Hanson, "Calibration-free wavelength-modulation spectroscopy for measurements of gas temperature and concentration in harsh environments," Appl. Opt. **48**, 5546–5560 (2009).

25. M. A. Bolshov, Y. A. Kuritsyn, and Y. V. Romanovskii, "Tunable diode laser spectroscopy as a technique for combustion diagnostics," Spectrochimica Acta Part B: Atomic Spectroscopy **106**, 45–66 (2015).

26. T. Cai, T. Tan, G. Wang, W. Chen, and X. Gao, "Gas temperature measurements using wavelength modulation spectroscopy at 1.39 µm," Optica Applicata **39**, 13–29 (2009).

27. V. Ebert, T. Fernholz, C. Giesemann, H. Pitz, H. Teichert, J. Wolfrum, and H. Jaritz, "Simultaneous diode-laser-based in situ detection of multiple species and temperature in a gas-fired power plant," Proceedings of the Combustion Institute **28**, 423–430 (2000).

28. R. K. Hanson and D. F. Davidson, "Recent advances in laser absorption and shock tube methods for studies of combustion chemistry," Progress in Energy and Combustion Science **44**, 103–114 (2014).

29. T. R. S. Hayden and G. B. Rieker, "Large amplitude wavelength modulation spectroscopy for sensitive measurements of broad absorbers," Opt. Express, OE **24**, 27910–27921 (2016).

30. Q. Huang, F. Wang, H. Zhang, J. Yan, M. Ni, and K. Cen, "In-situ CO measurement of gas and oil combustion flame using near infrared tunable diode laser with direct and modulated absorption signals," Optics Communications **306**, 99–105 (2013).

31. Z. Qu, R. Ghorbani, D. Valiev, and F. M. Schmidt, "Calibration-free scanned wavelength modulation spectroscopy – application to H_2O and temperature sensing in flames," Optics Express **23**, 16492 (2015).

32. S. Wagner, B. T. Fisher, J. W. Fleming, and V. Ebert, "TDLAS-based in situ measurement of absolute acetylene concentrations in laminar 2D diffusion flames," Proceedings of the Combustion Institute **32**, 839–846 (2009).

33. S. J. Pachuta and M. Strobel, "Time-of-flight SIMS analysis of polypropylene films modified by flame treatments using isotopically labeled methane fuel," Journal of Adhesion Science and Technology **21**, 795–818 (2007).

34. M. Strobel, M. C. Branch, M. Ulsh, R. S. Kapaun, S. Kirk, and C. S. Lyons, "Flame surface modification of polypropylene film," Journal of Adhesion Science and Technology **10**, 515–539 (1996).

35. Z. Guoli, Z. Aimin, W. Jiating, L. Zhongwei, and X. Yong, "Measurement of OH Radicals in Dielectric Barrier Discharge Plasmas by Cavity Ring-Down Spectroscopy," Plasma Sci. Technol. **12**, 166 (2010).

36. N. Srivastava, C. Wang, and T. S. Dibble, "A study of OH radicals in an atmospheric AC discharge plasma using near infrared diode laser cavity ringdown spectroscopy combined with optical emission spectroscopy," Eur. Phys. J. D **54**, 77–86 (2009).

37. R. Grün and H.-J. Günther, "Plasma nitriding in industry—problems, new solutions and limits," Materials Science and Engineering: A **140**, 435–441 (1991).

38. P. Bruggeman and D. C. Schram, "On OH production in water containing atmospheric pressure plasmas," Plasma Sources Sci. Technol. **19**, 045025 (2010).

39. J. W. Daily, "Laser induced fluorescence spectroscopy in flames," Progress in energy and combustion science **23**, 133–199 (1997).

40. M. J. Dyer and D. R. Crosley, "Two-dimensional imaging of OH laser-induced fluorescence in a flame," Opt. Lett., OL **7**, 382–384 (1982).

41. J. M. Seitzman, R. K. Hanson, P. A. DeBarber, and C. F. Hess, "Application of quantitative two-line OH planar laser-induced fluorescence for temporally resolved planar thermometry in reacting flows," Appl. Opt., AO **33**, 4000–4012 (1994).

42. B. B. Dally, A. N. Karpetis, and R. S. Barlow, "Structure of turbulent non-premixed jet flames in a diluted hot coflow," Proceedings of the Combustion Institute **29**, 1147–1154 (2002).

43. X. Mercier, E. Therssen, J. F. Pauwels, and P. Desgroux, "Cavity ring-down measurements of OH radical in atmospheric premixed and diffusion flames.," Chemical Physics Letters **299**, 75–83 (1999).

44. J. P. Maillard, J. Chauville, and A. W. Mantz, "High-resolution emission spectrum of OH in an oxyacetylene flame from 3.7 to 0.9 μm," Journal of Molecular Spectroscopy **63**, 120–141 (1976).

45. R. K. Hanson, "Applications of quantitative laser sensors to kinetics, propulsion and practical energy systems," Proceedings of the Combustion Institute **33**, 1–40 (2011).

46. U. Azimov, N. Kawahara, and E. Tomita, "UV–visible light absorption by hydroxyl and formaldehyde and knocking combustion in a DME-HCCI engine," Fuel **98**, 164–175 (2012).

47. X. Cui, C. Lengignon, W. Tao, W. Zhao, G. Wysocki, E. Fertein, C. Coeur, A. Cassez, L. Croize, W. Chen, Y. Wang, W. Zhang, X. Gao, W. Liu, Y. Zhang, and F. Dong, "Photonic sensing of the

atmosphere by absorption spectroscopy," Journal of Quantitative Spectroscopy and Radiative Transfer **113**, 1300–1316 (2012).

48. G. J. Ray, T. N. Anderson, J. A. Caton, R. P. Lucht, and T. Walther, "OH sensor based on ultraviolet, continuous-wave absorption spectroscopy utilizing a frequency-quadrupled, fiber-amplified external-cavity diode laser," Opt. Lett., OL **26**, 1870–1872 (2001).

49. S. Wang and R. K. Hanson, "High-sensitivity 308.6-nm laser absorption diagnostic optimized for OH measurement in shock tube combustion studies," Appl. Phys. B **124**, 37 (2018).

50. R. Peeters, G. Berden, and G. Meijer, "Near-infrared cavity enhanced absorption spectroscopy of hot water and OH in an oven and in flames," Appl Phys B **73**, 65–70 (2001).

51. L. Rutkowski, A. Khodabakhsh, A. C. Johansson, D. M. Valiev, L. Lodi, Z. Qu, R. Ghorbani, O. L. Polyansky, Y. Jin, J. Tennyson, F. M. Schmidt, and A. Foltynowicz, "Measurement of H2O and OH in a flame by optical frequency comb spectroscopy," in *2016 Conference on Lasers and Electro-Optics (CLEO)* (2016), pp. 1–2.

52. T. Aizawa, "Diode-laser wavelength-modulation absorption spectroscopy for quantitative in situ measurements of temperature and OH radical concentration in combustion gases," Applied optics **40**, 4894–4903 (2001).

53. T. Aizawa, T. Kamimoto, and T. Tamaru, "Measurements of OH radical concentration in combustion environments by wavelength-modulation spectroscopy with a 155-μm distributed-feedback diode laser," Applied Optics **38**, 1733 (1999).

54. L. Rutkowski, A. Foltynowicz, F. M. Schmidt, A. C. Johansson, A. Khodabakhsh, A. A. Kyuberis, N. F. Zobov, O. L. Polyansky, S. N. Yurchenko, and J. Tennyson, "An experimental water line list at 1950 K in the 6250–6670 cm−1 region," Journal of Quantitative Spectroscopy and Radiative Transfer **205**, 213–219 (2018).

55. P. J. Schroeder, D. J. Pfotenhauer, J. Yang, F. R. Giorgetta, W. C. Swann, I. Coddington, N. R. Newbury, and G. B. Rieker, "High temperature comparison of the HITRAN2012 and HITEMP2010 water vapor absorption databases to frequency comb measurements," Journal of Quantitative Spectroscopy and Radiative Transfer (2017).

56. D. C. Benner, C. P. Rinsland, V. M. Devi, M. A. H. Smith, and D. Atkins, "A multispectrum nonlinear least squares fitting technique," Journal of Quantitative Spectroscopy and Radiative Transfer **53**, 705–721 (1995).

57. B. J. Drouin, D. C. Benner, L. R. Brown, M. J. Cich, T. J. Crawford, V. M. Devi, A. Guillaume, J. T. Hodges, E. J. Mlawer, D. J. Robichaud, F. Oyafuso, V. H. Payne, K. Sung, E. H. Wishnow, and S. Yu, "Multispectrum analysis of the oxygen A-band," Journal of Quantitative Spectroscopy and Radiative Transfer **186**, 118–138 (2017).

58. T. R. Hayden, D. J. Petrykowski, A. Sanchez, S. P. Nigam, J. D. Christopher, C. LaPointe, N. T. Wimer, A. Upadhye, M. Strobel, P. E. Hamlington, and G. B. Rieker, "Characterization of OH, H2O, and temperature profiles in industrial flame treatment systems interacting with polymer films," Proceedings of the Combustion Institute **submitted**, (2018).

59. G. B. Rieker, J. B. Jeffries, R. K. Hanson, T. Mathur, M. R. Gruber, and C. D. Carter, "Diode laser-based detection of combustor instabilities with application to a scramjet engine," Proceedings of the Combustion Institute **32**, 831–838 (2009).

60. R. Sur, K. Sun, J. B. Jeffries, and R. K. Hanson, "Multi-species laser absorption sensors for in situ monitoring of syngas composition," Applied Physics B **115**, 9–24 (2014).

61.	T. R. Hayden, N. T. Wimer, C. LaPointe, S. P. Nigam, J. D. Christopher, A. Upadhye, M. Strobel, P. E. Hamlington, and G. B. Rieker, "Characterization of a buoyant jet from a catalytic combustor using wavelength modulation spectroscopy," International Journal of Heat and Mass Transfer **submitted**, (2018).

62.	I. Coddington, N. Newbury, and W. Swann, "Dual-comb spectroscopy," Optica, OPTICA **3**, 414–426 (2016).

63.	P. J. Schroeder, R. J. Wright, S. Coburn, B. Sodergren, K. C. Cossel, S. Droste, G. W. Truong, E. Baumann, F. R. Giorgetta, I. Coddington, N. R. Newbury, and G. B. Rieker, "Dual frequency comb laser absorption spectroscopy in a 16 MW gas turbine exhaust," Proceedings of the Combustion Institute **36**, 4565–4573 (2017).

64.	S. Coburn, C. B. Alden, R. Wright, K. Cossel, E. Baumann, G.-W. Truong, F. Giorgetta, C. Sweeney, N. R. Newbury, K. Prasad, I. Coddington, and G. B. Rieker, "Regional trace-gas source attribution using a field-deployed dual frequency comb spectrometer," Optica, OPTICA **5**, 320–327 (2018).

65.	I. Coddington, W. C. Swann, and N. R. Newbury, "Coherent dual-comb spectroscopy at high signal-to-noise ratio," Phys. Rev. A **82**, 043817 (2010).

66.	G.-W. Truong, E. M. Waxman, K. C. Cossel, E. Baumann, A. Klose, F. R. Giorgetta, W. C. Swann, N. R. Newbury, and I. Coddington, "Accurate frequency referencing for fieldable dual-comb spectroscopy," Opt. Express, OE **24**, 30495–30504 (2016).

67.	P. J. Schroeder, R. J. Wright, S. Coburn, B. Sodergren, K. C. Cossel, S. Droste, G. W. Truong, E. Baumann, F. R. Giorgetta, I. Coddington, N. R. Newbury, and G. B. Rieker, "Dual frequency comb laser absorption spectroscopy in a 16 MW gas turbine exhaust," Proceedings of the Combustion Institute **36**, 4565–4573 (2017).

68.	M. C. Branch, N. Sullivan, M. Ulsh, and M. Strobel, "Surface modification of polypropylene films by exposure to laminar, premixed methane-air flames," Symposium (International) on Combustion **27**, 2807–2813 (1998).

69.	G. B. Rieker, F. R. Giorgetta, W. C. Swann, J. Kofler, A. M. Zolot, L. C. Sinclair, E. Baumann, C. Cromer, G. Petron, C. Sweeney, P. P. Tans, I. Coddington, and N. R. Newbury, "Frequency-comb-based remote sensing of greenhouse gases over kilometer air paths," Optica, OPTICA **1**, 290–298 (2014).

70.	P. J. Schroeder, D. J. Pfotenhauer, J. Yang, F. R. Giorgetta, W. C. Swann, I. Coddington, N. R. Newbury, and G. B. Rieker, "High temperature comparison of the HITRAN2012 and HITEMP2010 water vapor absorption databases to frequency comb measurements," Journal of Quantitative Spectroscopy and Radiative Transfer (n.d.).

71.	E. M. Waxman, K. C. Cossel, G.-W. Truong, F. R. Giorgetta, W. C. Swann, S. Coburn, R. J. Wright, G. B. Rieker, I. Coddington, and N. R. Newbury, "Intercomparison of Open-Path Trace Gas Measurements with Two Dual Frequency Comb Spectrometers," Atmos Meas Tech **10**, 3295–3311 (2017).

72.	T. R. S. Hayden, D. J. Petrykowski, A. Sanchez, S. P. Nigam, C. Lapointe, J. D. Christopher, N. T. Wimer, A. Upadhye, M. Strobel, P. E. Hamlington, and G. B. Rieker, "Characterization of OH, H2O, and temperature profiles in industrial flame treatment systems interacting with polymer films," Proceedings of the Combustion Institute (2018).

73.	N. Sullivan, M. C. Branch, M. Strobel, J. Park, M. Ulsh, and B. Leys, "The Effects of an Impingement Surface and Quenching on the Structure of Laminar Premixed Flames," Combustion Science and Technology **158**, 115–134 (2000).

74. J. H. Bechtel and R. E. Teets, "Hydroxyl and its concentration profile in methane–air flames," Applied Optics **18**, 4138–4144 (1979).

75. M. Strobel, M. Ulsh, C. Stroud, and M. C. Branch, "The causes of non-uniform flame treatment of polypropylene film surfaces," Journal of Adhesion Science and Technology **20**, 1493–1505 (2006).

76. S. Farris, S. Pozzoli, P. Biagioni, L. Duó, S. Mancinelli, and L. Piergiovanni, "The fundamentals of flame treatment for the surface activation of polyolefin polymers – A review," Polymer **51**, 3591–3605 (2010).

77. E. Sheng, I. Sutherland, D. M. Brewis, R. J. Heath, and R. H. Bradley, "Surface studies of polyethylene modified by flame treatment," Journal of Materials Chemistry **4**, 487–490 (1994).

78. M. Strobel and C. S. Lyons, "An Essay on Contact Angle Measurements," Plasma Processes Polym. **8**, 8–13 (2011).

79. M. Strobel, M. C. Branch, M. Ulsh, R. S. Kapaun, S. Kirk, and C. S. Lyons, "Flame surface modification of polypropylene film," Journal of Adhesion Science and Technology **10**, 515–539 (1996).

80. G. K. Agrawal, S. Chakraborty, and S. K. Som, "Heat transfer characteristics of premixed flame impinging upwards to plane surfaces inclined with the flame jet axis," International Journal of Heat and Mass Transfer **53**, 1899–1907 (2010).

81. C. E. Baukal Jr. and B. Gebhart, "A review of empirical flame impingement heat transfer correlations," International Journal of Heat and Fluid Flow **17**, 386–396 (1996).

82. L. L. Dong, C. W. Leung, and C. S. Cheung, "Heat transfer of a row of three butane/air flame jets impinging on a flat plate," International Journal of Heat and Mass Transfer **46**, 113–125 (2003).

83. S. G. Tuttle, B. W. Webb, and M. Q. McQuay, "Convective heat transfer from a partially premixed impinging flame jet. Part II: Time-resolved results," International Journal of Heat and Mass Transfer **48**, 1252–1266 (2005).

84. S. Chander and A. Ray, "Heat transfer characteristics of three interacting methane/air flame jets impinging on a flat surface," International Journal of Heat and Mass Transfer **50**, 640–653 (2007).

85. S. Chander and A. Ray, "Flame impingement heat transfer: A review," Energy Conversion and Management **46**, 2803–2837 (2005).

86. L. C. Kwok, "Heat Transfer Characteristics of Slot and Round Premixed Impinging Flame Jets," Experimental Heat Transfer **16**, 111–137 (2003).

87. L. L. Dong, C. W. Leung, and C. S. Cheung, "Heat transfer characteristics of premixed butane/air flame jet impinging on an inclined flat surface," Heat and Mass Transfer **39**, 19–26 (2002).

88. C. Stroud, M. C. Branch, T. Vian, N. Sullivan, M. Strobel, and M. Ulsh, "Characterization of the thermal and fluid flow behavior of industrial ribbon burners," Fuel **87**, 2201–2210 (2008).

89. T. R. Hayden, N. Malarich, D. J. Petrykowski, S. P. Nigam, C. LaPointe, J. D. Christopher, N. T. Wimer, P. E. Hamlington, and G. B. Rieker, "OH radical detection in combustion environments using wavelength modulation spectroscopy and dual frequency comb spectroscopy near 1491 nm," **in prep**, (2018).

90. I. Glassman, R. A. Yetter, and N. G. Glumac, "Chapter 4 - Flame phenomena in premixed combustible gases," in *Combustion (Fifth Edition)* (Academic Press, 2015), pp. 147–254.

91. R. Carroni, V. Schmidt, and T. Griffin, "Catalytic combustion for power generation," Catalysis Today **75**, 287–295 (2002).

92. S. Keav, S. K. Matam, D. Ferri, and A. Weidenkaff, "Structured Perovskite-Based Catalysts and Their Application as Three-Way Catalytic Converters—A Review," Catalysts **4**, 226–255 (2014).

93. S. Minicò, S. Scirè, C. Crisafulli, R. Maggiore, and S. Galvagno, "Catalytic combustion of volatile organic compounds on gold/iron oxide catalysts," Applied Catalysis B: Environmental **28**, 245–251 (2000).

94. K. Persson, L. D. Pfefferle, W. Schwartz, A. Ersson, and S. G. Järås, "Stability of palladium-based catalysts during catalytic combustion of methane: The influence of water," Applied Catalysis B: Environmental **74**, 242–250 (2007).

95. J. D. Taylor, M. D. Allendorf, A. H. McDaniel, and S. F. Rice, "In Situ Diagnostics and Modeling of Methane Catalytic Partial Oxidation on Pt in a Stagnation-Flow Reactor," Ind. Eng. Chem. Res. **42**, 6559–6566 (2003).

96. P. Euzen, J.-H. Le Gal, B. Rebours, and G. Martin, "Deactivation of palladium catalyst in catalytic combustion of methane," Catalysis Today **47**, 19–27 (1999).

97. P. S. Barbato, G. Landi, and G. Russo, "Catalytic combustion of CH4-H2-CO mixtures at pressure up to 10 bar," Fuel Processing Technology **107**, 147–154 (2013).

98. O. Deutschmann, L. I. Maier, U. Riedel, A. H. Stroemman, and R. W. Dibble, "Hydrogen assisted catalytic combustion of methane on platinum," Catalysis Today **59**, 141–150 (2000).

99. C. S. Mcenally, L. D. Pfefferle, A. M. Schaffer, M. B. Long, R. K. Mohammed, M. D. Smooke, and M. B. Colkei, "Characterization of a coflowing methane/air non-premixed flame with computer modeling, rayleigh-raman imaging, and on-line mass spectrometry," Proceedings of the Combustion Institute **28**, 2063–2070 (2000).

100. Y. Hardalupas, C. S. Panoutsos, and A. M. K. P. Taylor, "Spatial resolution of a chemiluminescence sensor for local heat-release rate and equivalence ratio measurements in a model gas turbine combustor," Exp Fluids **49**, 883–909 (2010).

101. K. T. Kim, J. G. Lee, H. J. Lee, B. D. Quay, and D. A. Santavicca, "Characterization of Forced Flame Response of Swirl-Stabilized Turbulent Lean-Premixed Flames in a Gas Turbine Combustor," Journal of Engineering for Gas Turbines and Power **132**, 041502 (2010).

102. U. Stopper, M. Aigner, W. Meier, R. Sadanandan, M. Stöhr, and I. S. Kim, "Flow Field and Combustion Characterization of Premixed Gas Turbine Flames by Planar Laser Techniques," J. Eng. Gas Turbines Power **131**, 021504-021504–8 (2008).

103. S. Ducruix, D. Durox, and S. Candel, "Theoretical and experimental determinations of the transfer function of a laminar premixed flame," Proceedings of the Combustion Institute **28**, 765–773 (2000).

104. C. Stroud, M. C. Branch, T. Vian, N. Sullivan, M. Strobel, and M. Ulsh, "Characterization of the thermal and fluid flow behavior of industrial ribbon burners," Fuel **87**, 2201–2210 (2008).

105. F. Lemoine, Y. Antoine, M. Wolff, and M. Lebouche, "Simultaneous temperature and 2D velocity measurements in a turbulent heated jet using combined laser-induced fluorescence and LDA," Experiments in Fluids **26**, 315–323 (1999).

106. P. N. Papanicolaou and E. J. List, "Investigations of round vertical turbulent buoyant jets," Journal of Fluid Mechanics **195**, 341–391 (1988).

107. R. Watanabe, T. Gono, T. Yamagata, and N. Fujisawa, "Three-dimensional flow structure in highly buoyant jet by scanning stereo PIV combined with POD analysis," International Journal of Heat and Fluid Flow **52**, 98–110 (2015).

108.   M. Lackner, "Tunable diode laser absorption spectroscopy (TDLAS) in the process industries-A review," Reviews in Chemical Engineering **23**, 65–147 (2011).

109.   C. Greenshields, "OpenFOAM | The OpenFOAM Foundation," https://openfoam.org/.

110.   H. G. Weller, G. Tabor, H. Jasak, and C. Fureby, "A tensorial approach to computational continuum mechanics using object-oriented techniques," Computers in physics **12**, 620–631 (1998).

111.   Y. Wang, P. Chatterjee, and J. L. de Ris, "Large eddy simulation of fire plumes," Proceedings of the Combustion Institute **33**, 2473–2480 (2011).

112.   W.-W. Kim and S. Menon, "A new dynamic one-equation subgrid-scale model for large eddy simulations," in (1995), p. 356.

113.   B. M. Cetegen, Y. Dong, and M. C. Soteriou, "Experiments on stability and oscillatory behavior of planar buoyant plumes," Physics of Fluids **10**, 1658–1665 (1998).

114.   *Monthly Energy Review January 2016* (U.S. Energy Information Administration, n.d.).

115.   K. Sun, X. Chao, R. Sur, J. B. Jeffries, and R. K. Hanson, "Wavelength modulation diode laser absorption spectroscopy for high-pressure gas sensing," Applied Physics B **110**, 497–508 (2013).

116.   R. Arndt, "Analytical Line Shapes for Lorentzian Signals Broadened by Modulation," Journal of Applied Physics **36**, 2522–2524 (1965).

117.   V. Jayaraman, J. Jiang, B. Potsaid, G. Cole, J. Fujimoto, and A. Cable, "Design and performance of broadly tunable, narrow line-width, high repetition rate 1310nm VCSELs for swept source optical coherence tomography," in C. Lei and K. D. Choquette, eds. (2012), p. 82760D.

118.   V. Jayaraman, G. D. Cole, M. Robertson, A. Uddin, and A. Cable, "High-sweep-rate 1310 nm MEMS-VCSEL with 150 nm continuous tuning range," Electronics Letters **48**, 867–869 (2012).

119.   S. T. Sanders, J. A. Baldwin, T. P. Jenkins, D. S. Baer, and R. K. Hanson, "Diode-laser sensor for monitoring multiple combustion parameters in pulse detonation engines," Proceedings of the Combustion Institute **28**, 587–594 (2000).

120.   V. Nagali and R. K. Hanson, "Design of a diode-laser sensor to monitor water vapor in high-pressure combustion gases," Appl. Opt. **36**, 9518–9527 (1997).

121.   A. W. Caswell, S. Roy, X. An, S. T. Sanders, F. R. Schauer, and J. R. Gord, "Measurements of multiple gas parameters in a pulsed-detonation combustor using time-division-multiplexed Fourier-domain mode-locked lasers," Applied Optics **52**, 2893 (2013).

122.   K. Kohse-Höinghaus, R. S. Barlow, M. Aldén, and J. Wolfrum, "Combustion at the focus: laser diagnostics and control," Proceedings of the Combustion Institute **30**, 89–123 (2005).

123.   A. W. Caswell, S. Roy, X. An, S. T. Sanders, F. R. Schauer, and J. R. Gord, "Measurements of multiple gas parameters in a pulsed-detonation combustor using time-division-multiplexed Fourier-domain mode-locked lasers," Applied Optics **52**, 2893 (2013).

124.   T. Fernholz, H. Teichert, and V. Ebert, "Digital, phase-sensitive detection for in situ diode-laser spectroscopy under rapidly changing transmission conditions," Appl Phys B **75**, 229–236 (2002).

125.   G. Gao, B. Chen, and T. Cai, "Simultaneous detection of CO and CO2 at elevated temperatures using tunable diode laser absorption spectroscopy near 1570 nm," Opt. Spectrosc. **114**, 340–346 (2013).

126.   G. B. Rieker, X. Liu, H. Li, J. B. Jeffries, and R. K. Hanson, "Measurements of near-IR water vapor absorption at high pressure and temperature," Applied Physics B **87**, 169–178 (2007).

127. R. Sur, K. Sun, J. B. Jeffries, J. G. Socha, and R. K. Hanson, "Scanned-wavelength-modulation-spectroscopy sensor for CO, CO2, CH4 and H2O in a high-pressure engineering-scale transport-reactor coal gasifier," Fuel **150**, 102–111 (2015).

128. A. Farooq, J. B. Jeffries, and R. K. Hanson, "High-pressure measurements of CO2 absorption near 2.7 μm: Line mixing and finite duration collision effects," Journal of Quantitative Spectroscopy and Radiative Transfer **111**, 949–960 (2010).

129. C. S. Goldenstein, R. M. Spearrin, J. B. Jeffries, and R. K. Hanson, "Wavelength-modulation spectroscopy near 2.5 μm for H2O and temperature in high-pressure and -temperature gases," Applied Physics B **116**, 705–716 (2014).

130. W. R. Lempert, J. P. Looney, B. Zhang, and R. B. Miles, "Stimulated Raman scattering and coherent anti-Stokes Raman spectroscopy in high-pressure oxygen," Journal of the Optical Society of America B **7**, 715 (1990).

131. J. D. Miller, C. E. Dedic, S. Roy, J. R. Gord, and T. R. Meyer, "Interference-free gas-phase thermometry at elevated pressure using hybrid femtosecond/picosecond rotational coherent anti-Stokes Raman scattering," Optics Express **20**, 5003 (2012).

132. C. E. Dedic, J. B. Michael, J. D. Miller, and T. R. Meyer, "Evaluation of Hybrid fs/ps coherent anti-Stokes Raman scattering temperature and pressure sensivity at combustor relevant conditions," in (American Institute of Aeronautics and Astronautics, 2016).

133. D. J. Gardiner and P. R. Graves, *Practical Raman Spectroscopy* (Springer Science & Business Media, 2012).

134. B. A. Stein, V. Jayaraman, J. Y. Jiang, A. Cable, and S. T. Sanders, "Doppler-limited H2O and HF absorption spectroscopy by sweeping the 1,321–1,354 nm range at 55 kHz repetition rate using a single-mode MEMS-tunable VCSEL," Appl. Phys. B **108**, 721–725 (2012).

135. M. Abe, S. Kusanagi, Y. Nishida, O. Tadanaga, H. Takenouchi, and H. Sasada, "Dual wavelength 32-μm source for isotope ratio measurements of $^{13}CH_4/^{12}CH_4$," Optics Express **23**, 21786 (2015).

136. D. S. Bomse, A. C. Stanton, and J. A. Silver, "Frequency modulation and wavelength modulation spectroscopies: comparison of experimental methods using a lead-salt diode laser," Appl. Opt. **31**, 718–731 (1992).

137. L. C. Philippe and R. K. Hanson, "Laser diode wavelength-modulation spectroscopy for simultaneous measurement of temperature, pressure, and velocity in shock-heated oxygen flows," Appl. Opt. **32**, 6090–6103 (1993).

138. X. Chao, J. B. Jeffries, and R. K. Hanson, "Wavelength-modulation-spectroscopy for real-time, in situ NO detection in combustion gases with a 5.2 μm quantum-cascade laser," Appl. Phys. B **106**, 987–997 (2011).

139. "Modeling MEMS and NEMS," https://www.crcpress.com/Modeling-MEMS-and-NEMS/Pelesko-Bernstein/p/book/9781584883067.

140. H. Li, G. B. Rieker, X. Liu, J. B. Jeffries, and R. K. Hanson, "Extension of wavelength-modulation spectroscopy to large modulation depth for diode laser absorption measurements in high-pressure gases," Applied optics **45**, 1052–1061 (2006).

141. M. Y. Perrin and J. M. Hartmann, "Temperature-dependent measurements and modeling of absorption by CO2-N2 mixtures in the far line-wings of the 4.3μm CO2 band," Journal of Quantitative Spectroscopy and Radiative Transfer **42**, 311–317 (1989).

142. S. A. Clough, F. X. Kneizys, and R. W. Davies, "Line shape and the water vapor continuum," Atmospheric Research **23**, 229–241 (1989).

143. J. T. C. Liu, J. B. Jeffries, and R. K. Hanson, "Large-modulation-depth 2f spectroscopy with diode lasers for rapid temperature and species measurements in gases with blended and broadened spectra," Applied Optics **43**, 6500 (2004).

144. A. Farooq, J. B. Jeffries, and R. K. Hanson, "Sensitive detection of temperature behind reflected shock waves using wavelength modulation spectroscopy of CO2 near 2.7 μm," Appl. Phys. B **96**, 161–173 (2009).

145. A. S. Makowiecki, T. R. Hayden, M. R. Nakles, N. H. Pilgram, N. A. MacDonald, W. A. Hargus, and G. B. Rieker, "Wavelength modulation spectroscopy for measurements of temperature and species concentration downstream from a supersonic nozzle," in *53rd AIAA/SAE/ASEE Joint Propulsion Conference* (American Institute of Aeronautics and Astronautics, n.d.).

146. K. M. Tacina and W. J. A. Dahm, "Effects of heat release on turbulent shear flows. Part 1. A general equivalence principle for non-buoyant flows and its application to turbulent jet flames," Journal of Fluid Mechanics **415**, 23–44 (2000).

147. J. H. Bechtel and R. E. Teets, "Hydroxyl and its concentration profile in methane–air flames," Applied Optics **18**, 4138–4144 (1979).

8 Appendix A: Spectral line parameters for 1489-1490.5 nm (6700-6715 cm^{-1})

Table 8-1. This is a listing of the extracted absorption spectral line parameters for H_2O and the ones used for OH from 6700-6715 cm^{-1} using multi-spectral fitting routine described in [56,57]. The seed linelist of 453 H2O and four OH transitions is developed by evaluating a linestrength filter of $3x10^{-25}$ at 2000 K on the ~83,000 available transitions given in HITEMP 2010 for this spectral region. We floated the linestrength of 92 and 12 linecenters of the strongest H_2O transitions in order get a stable fit of the model to the data. For each parameter, linecenter and linestrength, there is a column denoting if it floated for the given transition. If the parameter is floated in the multi-spectral fitting routine the resulting uncertainty is listed in the following column. Finally, we perturbed the guess linestrength by +/- 10% to determine the stability of the resulting fit values, for which the resulting uncertainty is denoted in the final column for each parameter.

H₂O

Line #	Line center (cm^{-1})	Floated parameter?	Multi-spectral fit uncertainty (cm^{-1})	Perturbation uncertainty (cm^{-1})	Line-strength (cm^{-1}/molecule)	Floated parameter?	Multi-spectral fit uncertainty (%)	Perturbation uncertainty (%)
1	6700.0891	No	0	0.000	5.129E-37	No	0%	0%
2	6700.0891	No	0	0.000	1.710E-37	No	0%	0%
3	6700.0921	No	0	0.000	1.463E-33	No	0%	0%
4	6700.099169	No	0	0.000	9.800E-31	Yes	17%	0%
5	6700.1622	No	0	0.000	1.643E-37	No	0%	0%
6	6700.1771	No	0	0.000	1.789E-35	No	0%	0%
7	6700.2139	No	0	0.000	6.663E-34	No	0%	0%
8	6700.2175	No	0	0.000	1.126E-37	No	0%	0%
9	6700.2421	No	0	0.000	2.001E-33	No	0%	0%
10	6700.2493	No	0	0.000	3.961E-36	No	0%	0%
11	6700.273803	No	0	0.000	3.971E-37	No	0%	0%
12	6700.3287	No	0	0.000	4.866E-32	No	0%	0%
13	6700.3318	No	0	0.000	1.565E-32	No	0%	0%
14	6700.370525	No	0	0.000	1.858E-28	No	0%	0%
15	6700.423441	No	0	0.000	1.454E-38	Yes	23%	5%
16	6700.4844	No	0	0.000	1.121E-37	No	0%	0%

17	6700.4926	No	0	0.000	2.265E-36	No	0%	0%
18	6700.5096	No	0	0.000	3.414E-36	No	0%	0%
19	6700.5096	No	0	0.000	1.024E-35	No	0%	0%
20	6700.532519	No	0	0.000	6.761E-36	No	0%	0%
21	6700.561966	No	0	0.000	7.702E-35	No	0%	0%
22	6700.60506	No	0	0.000	4.428E-24	Yes	9%	11%
23	6700.648112	No	0	0.000	2.265E-36	Yes	30%	20%
24	6700.650482	No	0	0.000	3.098E-37	No	0%	0%
25	6700.6788	No	0	0.000	3.718E-32	Yes	51%	61%
26	6700.6964	No	0	0.000	3.850E-33	No	0%	0%
27	6700.7113	No	0	0.000	2.887E-33	No	0%	0%
28	6700.7463	No	0	0.000	1.957E-35	No	0%	0%
29	6700.7717	No	0	0.000	8.201E-29	No	0%	0%
30	6700.7858	No	0	0.000	2.484E-37	No	0%	0%
31	6700.849879	No	0	0.000	9.565E-36	No	0%	0%
32	6700.870577	No	0	0.000	3.655E-34	No	0%	0%
33	6700.880029	No	0	0.000	6.796E-28	No	0%	0%
34	6700.898296	No	0	0.000	1.461E-33	No	0%	0%
35	6701.009037	No	0	0.000	1.842E-35	No	0%	0%
36	6701.022382	No	0	0.000	1.017E-28	Yes	2%	0%
37	6701.035213	No	0	0.000	4.012E-32	No	0%	0%
38	6701.0663	No	0	0.000	1.848E-39	No	0%	0%
39	6701.07443	No	0	0.000	8.321E-25	Yes	11%	0%
40	6701.126192	No	0	0.000	1.105E-36	No	0%	0%
41	6701.1336	No	0	0.000	1.016E-37	No	0%	0%
42	6701.133884	No	0	0.000	1.099E-35	No	0%	0%
43	6701.34087	No	0	0.000	6.253E-26	No	0%	0%
44	6701.392778	No	0	0.000	8.620E-36	No	0%	0%
45	6701.386347	Yes	0.0035847	-0.001	2.731E-30	Yes	7%	1%
46	6701.4538	No	0	0.000	1.199E-40	No	0%	0%

103

47	6701.4834	No	0	0.000	2.916E-35	No	0%	0%
48	6701.51142	No	0	0.000	1.244E-24	Yes	5%	2%
49	6701.5138	No	0	0.000	4.490E-34	No	0%	0%
50	6701.515725	No	0	0.000	2.753E-38	No	0%	0%
51	6701.5954	No	0	0.000	1.487E-35	No	0%	0%
52	6701.6143	No	0	0.000	1.009E-32	No	0%	0%
53	6701.6185	No	0	0.000	9.360E-38	No	0%	0%
54	6701.61903	No	0	0.000	6.858E-26	No	0%	0%
55	6701.6205	No	0	0.000	2.840E-39	No	0%	0%
56	6701.6377	No	0	0.000	4.949E-36	No	0%	0%
57	6701.6582	No	0	0.000	1.499E-36	No	0%	0%
58	6701.66154	No	0	0.000	7.845E-32	No	0%	0%
59	6701.6904	No	0	0.000	4.987E-32	No	0%	0%
60	6701.7297	No	0	0.000	7.290E-32	No	0%	0%
61	6701.769844	No	0	0.000	2.408E-32	No	0%	0%
62	6701.850563	No	0	0.000	1.656E-30	No	0%	0%
63	6701.9225	No	0	0.000	4.668E-36	No	0%	0%
64	6701.9336	No	0	0.000	4.565E-36	No	0%	0%
65	6702.00795	No	0	0.000	6.782E-26	Yes	3%	1%
66	6702.0517	No	0	0.000	5.196E-29	No	0%	0%
67	6702.0755	No	0	0.000	1.336E-31	No	0%	0%
68	6702.083782	No	0	0.000	7.163E-32	No	0%	0%
69	6702.104012	No	0	0.000	1.490E-29	No	0%	0%
70	6702.137262	No	0	0.000	7.569E-36	No	0%	0%
71	6702.1482	No	0	0.000	1.147E-35	No	0%	0%
72	6702.2134	No	0	0.000	6.019E-39	No	0%	0%
73	6702.276864	No	0	0.000	1.170E-27	No	0%	0%
74	6702.3148	No	0	0.000	7.959E-32	Yes	11%	4%
75	6702.322205	No	0	0.000	1.767E-33	No	0%	0%
76	6702.3371	No	0	0.000	1.260E-35	No	0%	0%

77	6702.38916	No	0	0.000	1.353E-23	Yes	10%	6%
78	6702.451601	No	0	0.000	7.719E-34	No	0%	0%
79	6702.486	No	0	0.000	6.829E-38	No	0%	0%
80	6702.4879	No	0	0.000	2.049E-37	No	0%	0%
81	6702.5021	No	0	0.000	5.850E-25	No	0%	0%
82	6702.559782	No	0	0.000	1.773E-39	No	0%	0%
83	6702.56414	No	0	0.000	1.347E-26	No	0%	0%
84	6702.606962	No	0	0.000	1.694E-35	No	0%	0%
85	6702.6506	No	0	0.000	2.827E-35	Yes	16%	9%
86	6702.697409	No	0	0.000	1.859E-33	Yes	53%	12%
87	6702.7473	No	0	0.000	2.467E-33	No	0%	0%
88	6702.7596	No	0	0.000	3.133E-33	Yes	3%	2%
89	6702.810978	No	0	0.000	1.205E-35	No	0%	0%
90	6702.8487	No	0	0.000	3.758E-30	Yes	20%	26%
91	6702.85211	No	0	0.000	4.639E-30	No	0%	0%
92	6702.96897	No	0	0.000	6.656E-24	No	0%	0%
93	6702.987768	No	0	0.000	5.246E-39	No	0%	0%
94	6703.022446	Yes	0.0028709	0.005	2.380E-30	Yes	6%	9%
95	6703.09682	No	0	0.000	2.207E-25	No	0%	0%
96	6703.108834	No	0	0.000	1.532E-36	No	0%	0%
97	6703.111113	No	0	0.000	1.390E-30	Yes	170%	68%
98	6703.1269	No	0	0.000	1.945E-33	No	0%	0%
99	6703.2475	No	0	0.000	4.342E-42	No	0%	0%
100	6703.25664	No	0	0.000	4.115E-25	No	0%	0%
101	6703.2653	No	0	0.000	8.492E-33	No	0%	0%
102	6703.316757	No	0	0.000	3.941E-38	No	0%	0%
103	6703.35469	No	0	0.000	4.456E-33	Yes	12%	9%
104	6703.363375	No	0	0.000	2.326E-30	No	0%	0%
105	6703.43708	No	0	0.000	2.140E-25	Yes	18%	9%
106	6703.4446	No	0	0.000	1.901E-35	No	0%	0%

107	6703.454982	No	0	0.000	2.047E-28	No	0%	0%
108	6703.46935	No	0	0.000	2.738E-24	Yes	11%	10%
109	6703.4888	No	0	0.000	3.826E-33	No	0%	0%
110	6703.512144	No	0	0.000	1.345E-32	No	0%	0%
111	6703.52512	No	0	0.000	1.109E-29	Yes	24%	51%
112	6703.6374	No	0	0.000	2.081E-31	No	0%	0%
113	6703.6374	No	0	0.000	6.242E-31	No	0%	0%
114	6703.6652	No	0	0.000	3.764E-34	No	0%	0%
115	6703.66952	No	0	0.000	1.463E-30	No	0%	0%
116	6703.6776	No	0	0.000	1.791E-34	No	0%	0%
117	6703.68168	No	0	0.000	4.115E-25	No	0%	0%
118	6703.7994	No	0	0.000	8.516E-39	No	0%	0%
119	6703.817206	No	0	0.000	1.176E-32	No	0%	0%
120	6703.848715	No	0	0.000	4.245E-27	Yes	3%	2%
121	6703.857944	No	0	0.000	5.471E-33	No	0%	0%
122	6703.880629	No	0	0.000	3.049E-30	No	0%	0%
123	6703.9336	No	0	0.000	3.415E-33	No	0%	0%
124	6703.951326	No	0	0.000	6.532E-36	No	0%	0%
125	6703.9601	No	0	0.000	6.615E-36	No	0%	0%
126	6703.9611	No	0	0.000	2.206E-36	No	0%	0%
127	6703.962953	No	0	0.000	5.786E-36	No	0%	0%
128	6703.96428	No	0	0.000	2.517E-27	No	0%	0%
129	6703.9719	No	0	0.000	1.959E-34	No	0%	0%
130	6703.994	No	0	0.000	7.020E-41	No	0%	0%
131	6704.0162	No	0	0.000	1.886E-40	Yes	106%	68%
132	6704.11778	No	0	0.000	5.258E-26	Yes	10%	29%
133	6704.149288	No	0	0.000	2.173E-30	Yes	89%	221%
134	6704.16986	No	0	0.000	7.220E-39	Yes	18%	55%
135	6704.178532	No	0	0.000	4.214E-28	No	0%	0%
136	6704.1808	No	0	0.000	9.989E-42	No	0%	0%

137	6704.2461	No	0	0.000	2.591E-33	No	0%	0%
138	6704.2527	No	0	0.000	9.211E-39	No	0%	0%
139	6704.2552	No	0	0.000	2.763E-38	No	0%	0%
140	6704.2699	No	0	0.000	5.820E-42	No	0%	0%
141	6704.2827	No	0	0.000	4.814E-37	No	0%	0%
142	6704.2886	No	0	0.000	1.005E-29	No	0%	0%
143	6704.2886	No	0	0.000	3.015E-29	No	0%	0%
144	6704.292669	No	0	0.000	1.028E-33	No	0%	0%
145	6704.3454	No	0	0.000	6.229E-36	No	0%	0%
146	6704.4017	No	0	0.000	7.300E-31	No	0%	0%
147	6704.4324	No	0	0.000	1.070E-38	No	0%	0%
148	6704.43348	No	0	0.000	6.041E-36	No	0%	0%
149	6704.5491	No	0	0.000	1.225E-33	No	0%	0%
150	6704.5512	No	0	0.000	6.490E-41	No	0%	0%
151	6704.561899	Yes	0.0048785	-0.001	8.396E-23	Yes	8%	0%
152	6704.56631	No	0	0.000	2.033E-36	No	0%	0%
153	6704.616344	No	0	0.000	2.435E-37	No	0%	0%
154	6704.688612	No	0	0.000	3.600E-35	No	0%	0%
155	6704.712238	No	0	0.000	2.252E-35	No	0%	0%
156	6704.7267	No	0	0.000	1.630E-34	No	0%	0%
157	6704.772567	No	0	0.000	2.227E-27	No	0%	0%
158	6704.81921	No	0	0.000	7.279E-32	No	0%	0%
159	6704.8237	No	0	0.000	6.550E-32	No	0%	0%
160	6704.8509	No	0	0.000	2.324E-23	Yes	12%	4%
161	6704.9843	No	0	0.000	1.180E-35	No	0%	0%
162	6705.03851	No	0	0.000	2.123E-22	Yes	5%	1%
163	6705.07894	No	0	0.000	5.831E-28	No	0%	0%
164	6705.08746	No	0	0.000	7.867E-25	No	0%	0%
165	6705.071366	Yes	0.0048424	0.001	5.757E-28	Yes	12%	1%
166	6705.08137	Yes	0.0048424	0.001	1.728E-27	Yes	12%	1%

167	6705.18903	No	0	0.000	1.374E-35	No	0%	0%
168	6705.296386	No	0	0.000	2.265E-31	No	0%	0%
169	6705.298114	No	0	0.000	4.647E-28	No	0%	0%
170	6705.302323	No	0	0.000	1.151E-32	No	0%	0%
171	6705.35728	No	0	0.000	4.606E-34	No	0%	0%
172	6705.364105	No	0	0.000	7.533E-32	No	0%	0%
173	6705.44596	No	0	0.000	2.360E-36	No	0%	0%
174	6705.47191	No	0	0.000	2.512E-32	No	0%	0%
175	6705.480956	No	0	0.000	2.508E-27	No	0%	0%
176	6705.50954	No	0	0.000	1.392E-34	No	0%	0%
177	6705.566164	No	0	0.000	3.060E-28	No	0%	0%
178	6705.61722	No	0	0.000	9.556E-38	No	0%	0%
179	6705.6343	No	0	0.000	1.582E-38	No	0%	0%
180	6705.693708	No	0	0.000	3.018E-33	No	0%	0%
181	6705.721873	No	0	0.000	2.425E-28	No	0%	0%
182	6705.730665	Yes	0.0039931	0.000	2.088E-32	Yes	17%	1%
183	6705.7335	Yes	0.0039931	0.000	6.961E-33	Yes	17%	1%
184	6705.771495	No	0	0.000	1.537E-36	No	0%	0%
185	6705.8198	No	0	0.000	4.919E-41	No	0%	0%
186	6705.85671	No	0	0.000	6.483E-30	No	0%	0%
187	6705.8584	No	0	0.000	3.545E-38	No	0%	0%
188	6705.8804	No	0	0.000	1.208E-31	No	0%	0%
189	6705.968687	No	0	0.000	2.762E-27	No	0%	0%
190	6705.992607	No	0	0.000	2.195E-33	No	0%	0%
191	6706.0235	No	0	0.000	1.457E-40	No	0%	0%
192	6706.0915	No	0	0.000	2.404E-36	No	0%	0%
193	6706.1701	No	0	0.000	8.894E-40	No	0%	0%
194	6706.362322	No	0	0.000	1.158E-32	No	0%	0%
195	6706.373109	No	0	0.000	1.201E-35	Yes	7%	0%
196	6706.4069	No	0	0.000	7.668E-35	No	0%	0%

197	6706.465191	No	0	0.000	1.500E-32	No	0%	0%
198	6706.4707	No	0	0.000	1.452E-41	No	0%	0%
199	6706.5891	No	0	0.000	5.346E-36	Yes	22%	2%
200	6706.6312	No	0	0.000	2.487E-35	Yes	51%	15%
201	6706.6772	No	0	0.000	3.027E-36	Yes	75%	34%
202	6706.702713	No	0	0.000	2.290E-30	Yes	662%	644%
203	6706.7226	No	0	0.000	1.377E-36	No	0%	0%
204	6706.831	No	0	0.000	2.799E-34	Yes	4%	1%
205	6706.903497	No	0	0.000	1.059E-33	No	0%	0%
206	6706.925747	No	0	0.000	4.658E-32	No	0%	0%
207	6706.9755	No	0	0.000	2.949E-35	Yes	83%	62%
208	6706.9756	No	0	0.000	8.846E-35	Yes	83%	62%
209	6706.988698	No	0	0.000	7.136E-36	No	0%	0%
210	6707.0296	No	0	0.000	2.603E-34	No	0%	0%
211	6707.044	No	0	0.000	1.139E-37	No	0%	0%
212	6707.044576	No	0	0.000	5.790E-37	No	0%	0%
213	6707.079377	No	0	0.000	2.413E-37	No	0%	0%
214	6707.0888	No	0	0.000	7.841E-34	No	0%	0%
215	6707.156163	Yes	0.0011564	0.000	1.348E-35	Yes	6%	1%
216	6707.117102	No	0	0.000	9.780E-38	No	0%	0%
217	6707.145325	No	0	0.000	7.966E-27	No	0%	0%
218	6707.1907	No	0	0.000	1.953E-42	No	0%	0%
219	6707.278436	Yes	0.0089995	-0.002	6.736E-32	Yes	14%	5%
220	6707.24825	No	0	0.000	4.518E-24	No	0%	0%
221	6707.270635	No	0	0.000	4.162E-34	No	0%	0%
222	6707.280251	No	0	0.000	3.630E-37	No	0%	0%
223	6707.307394	No	0	0.000	3.237E-37	No	0%	0%
224	6707.323	No	0	0.000	2.003E-38	No	0%	0%
225	6707.327347	No	0	0.000	2.490E-29	No	0%	0%
226	6707.33362	No	0	0.000	7.336E-32	Yes	2%	0%

227	6707.34026	No	0	0.000	2.200E-31	Yes	2%	0%
228	6707.3754	No	0	0.000	2.680E-35	No	0%	0%
229	6707.43124	No	0	0.000	2.546E-31	Yes	3%	1%
230	6707.4522	No	0	0.000	6.313E-36	No	0%	0%
231	6707.4955	No	0	0.000	5.553E-41	No	0%	0%
232	6707.540442	Yes	0.0029353	0.000	4.467E-32	Yes	13%	6%
233	6707.679371	No	0	0.000	5.941E-32	Yes	13%	7%
234	6707.707493	No	0	0.000	1.657E-27	No	0%	0%
235	6707.73718	No	0	0.000	2.227E-25	No	0%	0%
236	6707.764937	No	0	0.000	1.437E-37	Yes	17%	2%
237	6707.78699	No	0	0.000	3.927E-34	No	0%	0%
238	6707.7979	No	0	0.000	7.538E-33	No	0%	0%
239	6707.854061	No	0	0.000	3.218E-36	No	0%	0%
240	6707.91444	Yes	0.0025404	-0.001	5.480E-30	Yes	4%	2%
241	6707.9514	No	0	0.000	1.138E-34	No	0%	0%
242	6707.9657	No	0	0.000	1.740E-41	No	0%	0%
243	6707.987754	No	0	0.000	2.326E-31	No	0%	0%
244	6708.000048	No	0	0.000	6.979E-31	No	0%	0%
245	6708.0051	No	0	0.000	4.768E-36	No	0%	0%
246	6708.07473	No	0	0.000	2.626E-30	Yes	11%	4%
247	6708.1141	No	0	0.000	2.008E-36	No	0%	0%
248	6708.1306	No	0	0.000	2.123E-33	Yes	11%	9%
249	6708.1314	No	0	0.000	7.075E-34	Yes	11%	9%
250	6708.1799	No	0	0.000	1.108E-35	No	0%	0%
251	6708.1892	No	0	0.000	7.049E-37	Yes	15%	8%
252	6708.1892	No	0	0.000	2.115E-36	Yes	15%	8%
253	6708.194434	No	0	0.000	2.411E-37	No	0%	0%
254	6708.2246	No	0	0.000	1.016E-38	No	0%	0%
255	6708.23312	No	0	0.000	3.993E-35	No	0%	0%
256	6708.26106	No	0	0.000	3.341E-34	No	0%	0%

110

257	6708.305914	No	0	0.000	2.677E-30	Yes	7%	2%
258	6708.3217	No	0	0.000	2.978E-40	No	0%	0%
259	6708.332	No	0	0.000	4.429E-32	No	0%	0%
260	6708.351531	No	0	0.000	2.118E-30	No	0%	0%
261	6708.359237	No	0	0.000	1.377E-29	No	0%	0%
262	6708.3878	No	0	0.000	5.316E-34	No	0%	0%
263	6708.415991	No	0	0.000	1.657E-34	Yes	26%	14%
264	6708.42509	No	0	0.000	1.174E-24	No	0%	0%
265	6708.45554	No	0	0.000	2.468E-34	Yes	43%	10%
266	6708.4714	No	0	0.000	2.553E-36	No	0%	0%
267	6708.513464	No	0	0.000	2.900E-33	No	0%	0%
268	6708.52686	No	0	0.000	1.090E-35	Yes	39%	8%
269	6708.555077	No	0	0.000	1.004E-28	No	0%	0%
270	6708.564222	No	0	0.000	1.779E-29	No	0%	0%
271	6708.602407	No	0	0.000	1.404E-29	Yes	1%	0%
272	6708.656893	No	0	0.000	9.720E-31	Yes	86%	50%
273	6708.6705	No	0	0.000	2.609E-31	No	0%	0%
274	6708.676083	No	0	0.000	6.341E-36	No	0%	0%
275	6708.7317	No	0	0.000	9.341E-34	No	0%	0%
276	6708.7459	No	0	0.000	2.144E-36	No	0%	0%
277	6708.7754	No	0	0.000	4.645E-29	No	0%	0%
278	6708.8665	No	0	0.000	7.842E-41	No	0%	0%
279	6708.925082	No	0	0.000	5.388E-33	Yes	8%	2%
280	6708.9507	No	0	0.000	7.583E-42	No	0%	0%
281	6708.951572	No	0	0.000	1.754E-35	No	0%	0%
282	6709.051557	No	0	0.000	9.606E-31	Yes	6%	1%
283	6709.144855	No	0	0.000	1.916E-31	No	0%	0%
284	6709.198066	No	0	0.000	5.015E-30	Yes	3%	0%
285	6709.271307	No	0	0.000	1.364E-29	No	0%	0%
286	6709.299043	No	0	0.000	6.465E-33	No	0%	0%

111

287	6709.307754	No	0	0.000	2.303E-27	Yes	5%	1%
288	6709.463468	No	0	0.000	2.880E-32	Yes	5%	0%
289	6709.528928	No	0	0.000	1.177E-29	Yes	6%	1%
290	6709.56511	No	0	0.000	1.203E-32	No	0%	0%
291	6709.6146	No	0	0.000	1.335E-36	Yes	9%	1%
292	6709.6146	No	0	0.000	4.006E-36	Yes	9%	1%
293	6709.673223	Yes	0.0024925	0.000	8.187E-38	Yes	12%	1%
294	6709.709	No	0	0.000	1.351E-42	No	0%	0%
295	6709.73292	No	0	0.000	4.131E-30	No	0%	0%
296	6709.7633	No	0	0.000	4.890E-35	No	0%	0%
297	6709.7668	No	0	0.000	3.860E-30	No	0%	0%
298	6709.790265	No	0	0.000	3.037E-30	Yes	1%	0%
299	6709.8018	No	0	0.000	5.024E-33	No	0%	0%
300	6709.829022	No	0	0.000	9.140E-30	Yes	1%	0%
301	6709.832682	No	0	0.000	3.215E-33	No	0%	0%
302	6709.86039	No	0	0.000	1.031E-28	No	0%	0%
303	6709.8858	No	0	0.000	5.857E-31	No	0%	0%
304	6709.8944	No	0	0.000	1.952E-31	No	0%	0%
305	6709.8963	No	0	0.000	2.691E-35	No	0%	0%
306	6709.9577	No	0	0.000	5.468E-35	No	0%	0%
307	6709.9652	No	0	0.000	1.635E-34	No	0%	0%
308	6709.977889	No	0	0.000	2.582E-27	No	0%	0%
309	6709.98306	No	0	0.000	5.735E-33	No	0%	0%
310	6710.026605	No	0	0.000	4.975E-30	Yes	4%	0%
311	6710.028375	No	0	0.000	1.658E-30	Yes	4%	0%
312	6710.029148	No	0	0.000	1.055E-33	No	0%	0%
313	6710.091525	No	0	0.000	1.286E-32	No	0%	0%
314	6710.0921	No	0	0.000	8.549E-35	No	0%	0%
315	6710.10199	No	0	0.000	2.427E-39	No	0%	0%
316	6710.1416	No	0	0.000	1.650E-36	No	0%	0%

317	6710.143702	No	0	0.000	4.394E-30	Yes	4%	0%
318	6710.16808	No	0	0.000	1.109E-25	No	0%	0%
319	6710.29184	No	0	0.000	2.453E-24	Yes	6%	0%
320	6710.33795	No	0	0.000	5.687E-39	No	0%	0%
321	6710.3572	No	0	0.000	2.191E-27	Yes	6%	0%
322	6710.37807	No	0	0.000	9.480E-26	No	0%	0%
323	6710.4131	No	0	0.000	1.971E-34	No	0%	0%
324	6710.435065	No	0	0.000	5.176E-34	No	0%	0%
325	6710.4448	No	0	0.000	8.012E-35	No	0%	0%
326	6710.471	No	0	0.000	1.166E-35	No	0%	0%
327	6710.4959	No	0	0.000	1.290E-34	No	0%	0%
328	6710.52653	No	0	0.000	6.656E-26	No	0%	0%
329	6710.5791	No	0	0.000	2.087E-37	No	0%	0%
330	6710.601009	No	0	0.000	2.587E-33	No	0%	0%
331	6710.619253	No	0	0.000	7.736E-33	No	0%	0%
332	6710.699593	No	0	0.000	2.246E-30	Yes	8%	0%
333	6710.77056	No	0	0.000	6.902E-30	No	0%	0%
334	6710.8088	No	0	0.000	7.533E-36	No	0%	0%
335	6710.8091	No	0	0.000	2.260E-35	No	0%	0%
336	6710.84361	No	0	0.000	2.546E-28	No	0%	0%
337	6710.880658	No	0	0.000	8.485E-33	No	0%	0%
338	6710.9052	No	0	0.000	1.190E-40	No	0%	0%
339	6711.1526	No	0	0.000	2.187E-35	No	0%	0%
340	6711.156463	No	0	0.000	5.037E-28	No	0%	0%
341	6711.20319	No	0	0.000	5.925E-28	Yes	5%	0%
342	6711.30345	No	0	0.000	5.365E-25	No	0%	0%
343	6711.30559	No	0	0.000	3.000E-32	No	0%	0%
344	6711.30611	No	0	0.000	4.463E-31	No	0%	0%
345	6711.332	No	0	0.000	1.737E-36	No	0%	0%
346	6711.332016	No	0	0.000	1.006E-24	No	0%	0%

113

347	6711.333851	No	0	0.000	3.352E-25	No	0%	0%
348	6711.3496	No	0	0.000	1.779E-38	No	0%	0%
349	6711.38954	No	0	0.000	1.453E-30	Yes	39%	4%
350	6711.411315	No	0	0.000	1.653E-34	Yes	102%	4%
351	6711.4338	No	0	0.000	9.682E-26	No	0%	0%
352	6711.4897	No	0	0.000	4.544E-33	No	0%	0%
353	6711.4999	No	0	0.000	7.734E-42	No	0%	0%
354	6711.518757	No	0	0.000	5.284E-35	No	0%	0%
355	6711.5328	No	0	0.000	1.562E-36	No	0%	0%
356	6711.5665	No	0	0.000	6.949E-35	No	0%	0%
357	6711.569181	No	0	0.000	4.745E-29	No	0%	0%
358	6711.5954	No	0	0.000	2.298E-35	No	0%	0%
359	6711.597	No	0	0.000	6.895E-35	No	0%	0%
360	6711.638	No	0	0.000	7.357E-35	No	0%	0%
361	6711.713497	Yes	0.0033037	0.001	4.297E-29	Yes	12%	6%
362	6711.689243	No	0	0.000	9.488E-33	No	0%	0%
363	6711.74982	No	0	0.000	6.687E-25	Yes	36%	14%
364	6711.7725	No	0	0.000	9.279E-24	No	0%	0%
365	6711.785894	No	0	0.000	3.654E-29	Yes	17%	6%
366	6711.90434	No	0	0.000	1.111E-28	No	0%	0%
367	6711.9222	No	0	0.000	6.445E-31	No	0%	0%
368	6711.92306	No	0	0.000	2.412E-30	No	0%	0%
369	6711.9847	No	0	0.000	3.560E-35	No	0%	0%
370	6712.1753	No	0	0.000	2.931E-33	No	0%	0%
371	6712.179036	No	0	0.000	1.242E-38	No	0%	0%
372	6712.211902	No	0	0.000	3.957E-29	Yes	12%	30%
373	6712.239798	No	0	0.000	3.826E-34	No	0%	0%
374	6712.25807	No	0	0.000	2.542E-25	No	0%	0%
375	6712.259543	No	0	0.000	2.146E-32	Yes	40%	106%
376	6712.267	No	0	0.000	4.877E-42	No	0%	0%

114

377	6712.339044	No	0	0.000	8.206E-34	No	0%	0%
378	6712.3939	No	0	0.000	7.574E-34	No	0%	0%
379	6712.4519	No	0	0.000	4.322E-38	No	0%	0%
380	6712.550033	No	0	0.000	3.212E-29	Yes	9%	4%
381	6712.637835	No	0	0.000	1.046E-32	No	0%	0%
382	6712.6686	No	0	0.000	1.950E-41	No	0%	0%
383	6712.677	No	0	0.000	4.995E-34	No	0%	0%
384	6712.6775	No	0	0.000	1.665E-34	No	0%	0%
385	6712.7089	No	0	0.000	2.584E-35	No	0%	0%
386	6712.7091	No	0	0.000	8.615E-36	No	0%	0%
387	6712.713135	No	0	0.000	1.271E-34	No	0%	0%
388	6712.726483	No	0	0.000	4.544E-34	No	0%	0%
389	6712.75013	No	0	0.000	9.905E-23	Yes	3%	1%
390	6712.77	No	0	0.000	4.550E-37	No	0%	0%
391	6712.7906	No	0	0.000	4.891E-32	No	0%	0%
392	6712.8128	No	0	0.000	2.000E-33	No	0%	0%
393	6712.8405	No	0	0.000	1.180E-27	No	0%	0%
394	6712.8454	No	0	0.000	5.993E-33	No	0%	0%
395	6712.90425	No	0	0.000	1.232E-22	Yes	3%	1%
396	6712.921382	No	0	0.000	6.429E-31	No	0%	0%
397	6712.93545	No	0	0.000	3.974E-25	No	0%	0%
398	6712.94077	No	0	0.000	2.378E-35	No	0%	0%
399	6712.9652	No	0	0.000	2.928E-38	No	0%	0%
400	6712.998158	No	0	0.000	2.357E-31	Yes	70%	3%
401	6712.998534	No	0	0.000	7.856E-32	Yes	70%	3%
402	6713.05881	No	0	0.000	2.579E-32	No	0%	0%
403	6713.065699	No	0	0.000	1.311E-33	Yes	157%	4%
404	6713.085051	No	0	0.000	1.103E-33	No	0%	0%
405	6713.099329	No	0	0.000	1.883E-28	No	0%	0%
406	6713.194766	No	0	0.000	9.338E-35	No	0%	0%

407	6713.218957	No	0	0.000	6.609E-38	No	0%	0%
408	6713.261077	No	0	0.000	1.246E-39	No	0%	0%
409	6713.286747	No	0	0.000	4.012E-30	No	0%	0%
410	6713.299336	No	0	0.000	3.394E-35	No	0%	0%
411	6713.331033	No	0	0.000	1.690E-32	No	0%	0%
412	6713.3437	No	0	0.000	3.173E-40	No	0%	0%
413	6713.349707	No	0	0.000	3.726E-30	No	0%	0%
414	6713.356453	No	0	0.000	3.902E-39	No	0%	0%
415	6713.4095	No	0	0.000	7.825E-36	No	0%	0%
416	6713.55447	No	0	0.000	2.752E-25	Yes	5%	0%
417	6713.709681	No	0	0.000	1.097E-30	No	0%	0%
418	6713.755923	No	0	0.000	7.022E-37	No	0%	0%
419	6713.7821	No	0	0.000	3.348E-38	No	0%	0%
420	6713.784191	No	0	0.000	3.106E-38	No	0%	0%
421	6713.812508	No	0	0.000	1.851E-35	No	0%	0%
422	6713.8296	No	0	0.000	2.531E-34	No	0%	0%
423	6713.8339	No	0	0.000	1.248E-38	No	0%	0%
424	6713.843756	No	0	0.000	1.279E-31	Yes	7%	1%
425	6713.913043	Yes	0.0005068	0.000	2.706E-31	Yes	2%	0%
426	6713.913043	Yes	0.0005068	0.000	9.020E-32	Yes	2%	0%
427	6713.92482	No	0	0.000	4.838E-30	No	0%	0%
428	6713.943164	No	0	0.000	1.452E-29	No	0%	0%
429	6713.9583	No	0	0.000	1.384E-28	No	0%	0%
430	6713.9598	No	0	0.000	4.613E-29	No	0%	0%
431	6713.961633	No	0	0.000	1.287E-29	No	0%	0%
432	6713.965017	No	0	0.000	7.931E-36	Yes	19%	4%
433	6713.98	No	0	0.000	1.697E-33	No	0%	0%
434	6714.023413	No	0	0.000	1.001E-29	No	0%	0%
435	6714.064245	No	0	0.000	2.237E-31	Yes	3%	0%
436	6714.073732	No	0	0.000	3.200E-39	No	0%	0%

116

437	6714.19946	No	0	0.000	9.663E-36	Yes	8%	0%
438	6714.20162	No	0	0.000	2.239E-25	No	0%	0%
439	6714.2036	No	0	0.000	4.716E-41	No	0%	0%
440	6714.2301	No	0	0.000	2.131E-31	No	0%	0%
441	6714.2518	No	0	0.000	6.322E-36	No	0%	0%
442	6714.272	No	0	0.000	6.986E-29	No	0%	0%
443	6714.286002	No	0	0.000	5.409E-33	No	0%	0%
444	6714.2951	No	0	0.000	1.603E-37	No	0%	0%
445	6714.38387	No	0	0.000	1.579E-24	Yes	1%	0%
446	6714.46	No	0	0.000	1.719E-28	No	0%	0%
447	6714.5356	No	0	0.000	5.181E-28	No	0%	0%
448	6714.5483	No	0	0.000	2.291E-35	No	0%	0%
449	6714.689018	No	0	0.000	1.004E-28	Yes	7%	0%
450	6714.7546	No	0	0.000	5.129E-38	No	0%	0%
451	6714.7744	No	0	0.000	7.172E-42	No	0%	0%
452	6714.9355	No	0	0.000	3.812E-32	No	0%	0%
453	6714.936162	No	0	0.000	2.616E-30	Yes	54%	2%

OH

Line #	Line center (cm^{-1})	Floated parameter?	Multi-spectral fit uncertainty (cm^{-1})	Perturbation uncertainty (cm^{-1})	Line-strength $(cm^{-1}/molecule)$	Floated parameter?	Multi-spectral fit uncertainty (%)	Perturbation uncertainty (%)
454	6707.00785	No	0	0.000	1.304E-21	No	0%	0%
455	6707.68202	No	0	0.000	1.315E-21	No	0%	0%
456	6712.63526	No	0	0.000	1.350E-28	No	0%	0%
457	6705.12788	No	0	0.000	5.785E-31	No	0%	0%

117